Università degli Studi di Padova

Dipartimento di Ingegneria Industriale

Corso di Laurea Magistrale in
Ingegneria Meccanica

Minimum Lap Time of Race Cars: Modelling and Simulation

Laureando:
Matteo Veneri

Relatore:
Ch.mo Prof. Matteo Massaro

Matricola:
1105175

Correlatore:
Dott. Nicola Dal Bianco

Anno accademico 2015/2016

Alla mia famiglia.

Sommario

Il lavoro di ricerca ha l'obiettivo di investigare problemi di tempo minimo relativi a vetture da corsa. Innanzitutto sarà sviluppata un'attenta attività di modellizzazione, con differenti livelli di complessità per quanto riguarda i modelli di veicolo e i tracciati percorsi. Il problema verrà quindi trascritto, mediante il software GPOPS-II, nella formulazione tipica di un problema NLP. La soluzione è dunque ottenuta grazie all'utilizzo di un codice di ottimizzazione, ovvero IPOPT, che permette di risolvere problemi con un numero molto elevato di variabili. Successivamente sarà considerata la validazione del modello numerico con riferimento ai test su strada, oltre ad un'analisi dei risultati e delle peculiarità derivanti da diverse strategie di modellizzazione. Infine verrà sviluppata un'analisi parametrica relativa ai principali parametri che influenzano la prestazione della vettura.

Abstract

The work investigates minimum lap time problems of race cars. A careful modelling activity is carried out first, with different levels of complexity both in the vehicle and road models. The problem is then transcribed in a form suitable for the solution as an NLP problem, using the software GPOPS-II. The solution is then achieved by means of an optimizer used for large scale problems, namely IPOPT. A validation of the numerical model against road tests is provided, together with a focus on the results and peculiarities resulting from the different modelling approaches. Finally, a parametric analysis on the main parameters affecting vehicle performance is carried out.

Contents

Introduction

Nowadays we are witnesses of an increasing importance of the "technological" aspects related to the vehicles; this evident trend conveys only a mere consumeristic meaning of the word "technology" and, in front of that, the study of vehicle mechanics and dynamics seems to be an outmoded discipline, in which nothing more should be investigated. Nevertheless, the many systems implemented in the modern vehicles are absolutely not independent from a mechanics-based modelling point of view; because of that, vehicle engineering offers a huge amount of research topics tightly connected to the proper technological improvements, which are going to define the future development of cars and motorcycles.
The modern progress in safety, performance and comfort of cars and motorcycles is significantly related with the possibility of describing these mechanical systems and their dynamic behaviour, with accurate models that implement the capability of predicting and suggesting real improvements in the everyday life. Self-driving vehicles, optimization of components and smart control and compensation of human mistakes are the very topics at the core of the vehicle dynamics research; moreover, at this point of investigation, for these topics can be taken into consideration many significant areas of improvement, imposing new targets in the technological evolution of the vehicle.
One of these is the development of optimal control problems, in which the University of Padua has been having an important contribution, in particular concerning the motorcycle simulations of minimum time problems [11]. The main advantage of these nonlinear methods is that they allow to simulate the ideal behaviour of the vehicle: the optimal control solution, in fact, represents the best performance achievable by the vehicle considered, as if an ideal driver was capable of exploiting all the possibilities offered by the vehicle dynamics; the vehicle is modelled using the equations of motion and the constraint equations that characterize its components.
There are mainly two different approaches to the optimal control problems: direct and indirect methods; the direct methods transcribe the problem into a proper Non Linear Programming (NLP) and discrete-domain minimum problem [1], while the indirect methods apply the *Pontryagin Minimum Principle* (PMP) and compute the stationary points of the target function [4]. During the last years a lot of research has been performed applying these two methods separately to vehicle dynamics problems.
A popular implementation of a direct method is GPOPS (General Purpose Optimal Control Software) which has been developed by Patterson at al. and takes advantage of a user-friendly interface, based on the MATLAB code [5]. Limebeer

et al. [12] have studied a vast amount of topics regarding the direct methods, such as the optimal simulation of Formula One hybrid powertrains; they used a simple model of powertrain, assuming a different power displacement in every different condition imposed by the pilot, and a basic car model, obtained considering the vehicle as a moving rigid body with concentrated mass and forces applied to the ideal points of contacts of the wheels.
On the other hand, one of the most efficient implementations of the indirect method is XOPTIMA, developed by Da Lio et al. [11] and Bertolazzi et al. [4]. Also this method has produced very significant results in vehicle dynamics research, both with regards to cars and motorcycles; referring to motorbikes, Bobbo et al. [14] developed a model which takes into account the most important rigid body dynamics and a linear tyre model, with the forces limited into adherence ellipses, and two controls applied on the steering angle and on the longitudinal forces at the contact points. Moreover the indirect strategy has been adopted to develop parametric optimizations: for instance Tremlett et al. [15] have recently simulated the control of a race car considering the model of a self-locking differential in different maneuvers; the dynamics has been simulated for different values of the differential viscosity constant and the dependency of the lap time has been studied.
Lot et al. [13] and Perantoni et al. [9] have developed a model of a tridimensional track for optimal control simulations, with indirect and direct methods respectively: the track data is obtained from a point to point reconstruction of the road from satellite images while the optimization of the raw data is achieved by an optimal control problem that optimizes the road curvature to get rid of the typical data noise, due to the segmented acquisition.
In this work a full development of an optimal control problem applied to a four-wheeled vehicle will be provided to obtain a minimum time simulation, starting from the system multi-body modelling and proceeding to the setup of the problem, the solution and the post-processing analysis. In particular two models will be investigated (ch. 2): the *basic* model, in which the tyre forces are calculated with a *saturation* formula and their combination is related only to a constant constraint, and the so-called *slip-slip* model, that include a Pacejka implementation of the tyre formulas and a full slip combination, in which the longitudinal slip quantities are function of each other and vary with the normal load. Moreover a tridimensional dynamics will be considered, including the slope variation during the track. For each model a step by step formulation will be deduced, in order to obtain a *state space* formulation, that is fundamental for the description of the optimal control problem.
To simulate the vehicle it is fundamental to gain a complete representation of the road, or rather the full track and the *curvilinear coordinates* that connect the track to the vehicle trajectory. The track data is obtained from satellite images and an optimal control elaboration, to reduce the noise and the sampling mistakes. Three different circuits of the GT3 championship will be taken into consideration: the *Adria International Raceway*, in which the vehicle is usually tested, the *Autodromo Nazionale di Monza* and the *Autodromo Internazionale Enzo e Dino Ferrari* of Imola, where the variation of elevation allows to simulate the tridimensional model.

Starting from a data set of a GT3 vehicle, a setup for the problem will be defined considering the main vehicle parameters, the boundary conditions and the constraints that characterize and limit the vehicle dynamics. The optimal solution will be achieved adopting a direct method, that makes use of the transcription code GPOPS and the NLP solver IPOPT (ch. 1). As for the transcription phase, GPOPS provides a method based on the *Randau quadrature orthogonal collocation method*, while, for each iteration of the solver, the code implements a mesh refinement based on the *adaptive hp refinement method*. Furthermore the solver enforces a solution using a barrier function and controls the tolerance reached in each iteration, in order to respect the maximum error imposed by the user.
First of all a validation of the model will be considered (ch. 3), in order to compare the simulation results to the real behavior of the GT3 car; afterwards the focus will be drawn to the evaluation and analysis of the results on each track, for both the models developed, and to the comparison between different modelling strategies, that reflect different levels of complexity and different possibilities to capture the vehicle behaviors. Finally a parametric optimization will be developed (ch. 4), evaluating the best lap time achieved with different values of the parameters that characterize the car. The parameters of interest are related to the position of the centre of mass, the aerodynamics, the dimensions of the vehicle, the yaw inertia and the viscosity constant of the differential. This study will permit to find the effect of each parameter to the system and their importance and trend in term of reducing the lap time and optimizing the performance.
This work represents, for the University of Padua, the first all-rounded optimal control analysis with the adoption of direct methods; although most of the modelling and control techniques used are well consolidated in the optimal control research, a deep level of complication is reached with the *slip-slip* model, that implements a complete tyre forces formulation and an in-depth dynamics representation. Moreover an inedited comparison between the main models is provided and a parametric analysis for all the main vehicle characteristics is developed with this model for the first time.

Chapter 1

Optimal Control

1.1 Introduction

The optimal control problems are based on the research of a minimum of the cost functional $\mathcal{F}(\mathbf{u})$ in terms of the state function $\mathbf{x}(t)$ and control $\mathbf{u}(t)$:

$$\mathcal{F}(\mathbf{u}) = \boldsymbol{\phi}(\mathbf{x}(t_i), \mathbf{x}(t_f)) + \int_{t_i}^{t_f} \mathcal{L}(\mathbf{x}(t), \mathbf{u}(t))dt, \tag{1.1}$$

considering a dynamic system defined by the following state space equations:

$$\dot{\mathbf{x}}(t) = \mathbf{f}(\mathbf{x}(t), \mathbf{u}(t), t); \quad \mathbf{x}(t_i) = \mathbf{x}_i; \quad t \in (t_i, t_f). \tag{1.2}$$

The function $\boldsymbol{\phi}(\mathbf{x}(t_i), \mathbf{x}(t_f))$ is called the *Mayer* part of the cost function and determines the *initial/final payoff*, while $\mathcal{L}(\mathbf{x}(t), \mathbf{u}(t))$ represents the *Lagrange* term or *running payoff*; the entire formulation is usually associated to the *Bolza* problem.
There are two different methods to solve the optimal control problem implementing different strategies: the *direct* method and the *indirect* one; basically the first strategy is focused on the research of the minimum of $\mathcal{F}(\mathbf{u})$, using an approximate formulation of the problem obtained dividing the state space into a mesh of points, from which it is possible to find a solution of the differential equations; this method is based on the transcription of the optimal control problem into a *nonlinear programming problem*, converting the infinite-dimensional representation in a finite-dimensional approximation [1]. Differently, the *indirect* strategy is based on the research of a stationary point of the cost function (1.1), determining the root of the necessary condition, obtained imposing the first variation of the cost functional equal to zero.

1.2 Indirect Methods

The indirect methods are basically obtained considering the calculus of variations and the minimum principle; a deeper description can be found in [2] and [3].
Considering by definition the *Hamiltonian* $\mathcal{H}(\mathbf{x}, \boldsymbol{\lambda}, \mathbf{u}, t)$, it is possible to write the equation (1.1) conveniently in terms of the *Lagrangian multipliers* or *costates* $\boldsymbol{\lambda}(t)$:

$$\mathcal{H}(\mathbf{x}, \boldsymbol{\lambda}, \mathbf{u}, t) = \mathcal{L}(\mathbf{x}, \mathbf{u}, t) + \boldsymbol{\lambda} \cdot \mathbf{f}(\mathbf{x}, \mathbf{u}, t), \tag{1.3}$$

$$\mathcal{J}(\mathbf{x}, \boldsymbol{\lambda}, \mathbf{u}) = \boldsymbol{\phi}(\mathbf{x}(t_i), \mathbf{x}(t_f)) + \int_{t_i}^{t_f} \mathcal{H}(\mathbf{x}, \boldsymbol{\lambda}, \mathbf{u}, t) - \boldsymbol{\lambda}(t) \cdot \dot{\mathbf{x}}(t)\, dt. \tag{1.4}$$

Introducing the integration by parts of the last term of the integral in the (1.3) the equation becomes:

$$\mathcal{J}(\mathbf{x}, \boldsymbol{\lambda}, \mathbf{u}) = \boldsymbol{\phi}(\mathbf{x}(t_i, t_f)) - \boldsymbol{\lambda}(\mathbf{x}(t_f) - \mathbf{x}(t_i)) + \int_{t_i}^{t_f} \mathcal{H} dt + \int_{t_i}^{t_f} \dot{\boldsymbol{\lambda}}(t) \cdot \mathbf{x}\, dt. \tag{1.5}$$

The research of the stationary points of the cost functional can be translated in the necessary condition $\delta\mathcal{J} = 0$ as follows:

$$\delta\mathcal{J} = \boldsymbol{\phi}_x \delta\mathbf{x}(t_f) - \boldsymbol{\lambda}(\delta\mathbf{x}(t_f) - \delta\mathbf{x}(t_i)) + \int_{t_i}^{t_f} \mathcal{H}_x \delta\mathbf{x} + \mathcal{H}_u \delta\mathbf{u} + \dot{\boldsymbol{\lambda}}(t) \cdot \delta\mathbf{x}\, dt. \tag{1.6}$$

In order to satisfy this condition, the following set of equations must be verified:

$$\dot{\mathbf{x}}(t) = \mathbf{f}(\mathbf{x}(t), \mathbf{u}(t), t), \tag{1.7}$$

$$\mathcal{H}_x + \dot{\boldsymbol{\lambda}} = 0, \tag{1.8}$$

$$\mathcal{H}_u = 0, \tag{1.9}$$

with the following BCs:

$$\boldsymbol{\phi}_x - \boldsymbol{\lambda}(t_f) = 0, \tag{1.10}$$

$$\mathbf{x}(t_i) = \mathbf{x}_i. \tag{1.11}$$

The (1.8) are called *co-equations*, the (1.9) are called *optimality equations* and the (1.10) are the *transversality conditions*; note that $\delta\mathbf{x}(t_i) = 0$ to match the initial boundary condition.
If the stationary point found represents a minimum of the cost function, then it must be true the condition $\delta^2\mathcal{J} \geq 0$; this inequality can be reduced in the form of:

$$\int_{t_i}^{t_f} \delta\mathbf{u}^T \mathcal{H}_{uu}(\mathbf{x}, \boldsymbol{\lambda}, \mathbf{u}, t) \delta\mathbf{u}\, dt \geq 0; \tag{1.12}$$

Because of $\delta\mathbf{u}(t)$ is an arbitrary function, and considering the equations (1.12) and (1.9), it is possible to state that the solution is a stationary point for $\mathcal{H}(\mathbf{x}, \boldsymbol{\lambda}, \mathbf{u}, t)$ with $\mathbf{x}, \boldsymbol{\lambda}$ and t fixed: in particular the solution represents a local minimum. Therefore the solution $\mathbf{u}(t)$ can be written for a more general problem:

$$\mathbf{u}(t) = \text{argmin}\{\mathbf{v} \in \mathbb{R}^m \,|\, \mathcal{H}((\mathbf{x}, \boldsymbol{\lambda}, \mathbf{v}, t)\}; \tag{1.13}$$

in other terms the second variation of the *Hamiltonian* must be a semi-definite positive matrix. Applying the boundary conditions at both t_i and t_f permits to define this as a *two-point boundary value problem* (TPBVP).
The derivation of a necessary condition such as the (1.12) is actually complicated considering that the controls $\mathbf{u}(t)$ are typically bounded in defined limits of variation ($\mathbf{u}(t) \in \mathcal{U}$); because of that $\delta\mathbf{u}(t)$ is not arbitrary and it must be adopted a different strategy to obtain a necessary condition. A simple heuristic, based on the *Pontryagin Minimum Principle*, that can solve this problem is defined considering a barrier function $p(\mathbf{u}, \varepsilon)$:

$$p(\mathbf{u}, \varepsilon) = -\varepsilon\, log[\,\mathrm{dist}(\mathbf{u}, \mathbb{R}^m \backslash \mathcal{U})], \qquad \mathrm{dist}(\mathbf{u}, \mathcal{A}) = \inf\{|\mathbf{u} - \mathbf{v}|, \mathbf{v} \in \mathcal{A}\}; \quad (1.14)$$

it should be noticed that p is small positive if $\mathbf{u} \in \mathcal{U}$ and is ∞ for $\mathbf{u} \notin \mathcal{U}$. Adding the barrier function to the expression of the cost functional the result is:

$$\tilde{\mathcal{F}}(\mathbf{u}) = \boldsymbol{\phi}(\mathbf{x}(t_i), \mathbf{x}(t_f)) + \int_{t_i}^{t_f} \mathcal{L}(\mathbf{x}(t), \mathbf{u}(t) + p(\mathbf{u}(t), \varepsilon)\, dt. \quad (1.15)$$

Therefore, deriving the boundary value problem from an *unconstrained* $\mathbf{u}(t)$ and considering ε as an infinitesimal quantity, the controls result:

$$\mathbf{u}(t) = \mathrm{argmin}\{\mathbf{v} \in \mathcal{U} \,|\, \mathcal{H}((\mathbf{x}, \boldsymbol{\lambda}, \mathbf{v}, t)\}. \quad (1.16)$$

An efficient and reliable implementation of optimal control indirect techniques for solving the TPBVP con be found in [4].

1.3 Direct Methods

The direct implementations of the optimal control problems have their foundations on the *transcription method*; this strategy allows to convert a formulation that involves continuous functions, in order to describe the states $\mathbf{x}(t)$ and the controls $\mathbf{u}(t)$, into an NLP problem with a finite set of discrete variables and constraints. These concepts are deeply investigated in [1].
The solution of the problem is based on three main points:

1. convert the dynamic system into an NLP problem with a set of discrete variables;

2. solve the finite-dimensional problem using a parameter optimization method;

3. check the accuracy of the approximation and, if necessary, repeat transcription and optimization.

Referring to the same formulation used for the indirect methods, it is now possible to introduce a discrete approximation of the state equations (1.7):

$$\dot{\mathbf{x}} = \mathbf{f}(\mathbf{x}(t), \mathbf{u}(t)) \approx \frac{\mathbf{x}_{k+1} - \mathbf{x}_k}{h}; \quad (1.17)$$

in the NLP the controls and states are evaluated at $t_1, t_2, \ldots, t_M$ with $t_{k+1} = t_k + h$ and $h = t_f/M$. Therefore the (1.7) becomes a constraint equation for the new discrete problem:

$$c_k(\mathbf{x}, \mathbf{u}) = \mathbf{x}_{k+1} - \mathbf{x}_k - h\,\mathbf{f}(\mathbf{x}(t), \mathbf{u}(t)) = 0, \quad k = 1, \ldots, M-1. \tag{1.18}$$

Defining the *Lagrangian* as:

$$\begin{aligned} \mathcal{L}(\mathbf{x}, \mathbf{u}, \boldsymbol{\lambda}) &= \mathcal{F}(\mathbf{x}(t), \mathbf{u}(t)) - \boldsymbol{\lambda}^T\,\mathbf{c}(\mathbf{x}, \mathbf{u}) = \\ &= \mathcal{F}(\mathbf{x}_M) - \sum_{k=1}^{M-1} \boldsymbol{\lambda}_k^T\,(\mathbf{x}_{k+1} - \mathbf{x}_k - h\,\mathbf{f}(\mathbf{x}_k, \mathbf{u}_k)), \end{aligned} \tag{1.19}$$

then it is possible to determine the necessary conditions for this problem, considering the gradient of the Lagrangian with respect of $\mathbf{x}, \mathbf{u}, \boldsymbol{\lambda}$ equal to zero: $\nabla\mathcal{L}(\mathbf{x}, \mathbf{u}, \boldsymbol{\lambda}) = 0$; therefore the necessary equations become[1]

$$\frac{\partial\mathcal{L}}{\partial\boldsymbol{\lambda}_k} = \mathbf{x}_{k+1} - \mathbf{x}_k - h\,\mathbf{f}(\mathbf{x}_k, \mathbf{u}_k) = 0, \tag{1.20}$$

$$\frac{\partial\mathcal{L}}{\partial\mathbf{x}_k} = (\boldsymbol{\lambda}_k - \boldsymbol{\lambda}_{k-1}) + h\,\boldsymbol{\lambda}_k^T\,\frac{\partial\mathbf{f}}{\partial\mathbf{x}_k} = 0, \tag{1.21}$$

$$\frac{\partial\mathcal{L}}{\partial\mathbf{u}_k} = h\,\boldsymbol{\lambda}_k^T\,\frac{\partial\mathbf{f}}{\partial\mathbf{u}_k} = 0, \tag{1.22}$$

$$\frac{\partial\mathcal{L}}{\partial\mathbf{x}_M} = -\boldsymbol{\lambda}_M + \frac{\partial\mathcal{F}}{\partial\mathbf{x}_M} = 0. \tag{1.23}$$

It is important to underline that with $M \to \infty$ and consequently $h \to 0$ the necessary conditions for the NLP become equal to the conditions found for the optimal control problem in section 1.2; in particular the (1.20) become the state equations (1.7), the (1.21) become the *adjoint equations* (co-equations) (1.8), equations (1.22) become the control equations (1.9) and the (1.23) become the transversality conditions (1.10): in other words, the necessary conditions for the NLP, approach the optimal control conditions increasing the number of discrete intervals of the mesh.
In addition to the other constraints, the direct formulation allows a robust implementation of algebraic *path constraints* which can be written in the form

$$\mathbf{g}(\mathbf{x}(t), \mathbf{u}(t), t) = 0, \tag{1.24}$$

and consequently the Hamiltonian can be expressed in the form

$$\mathcal{H} = \boldsymbol{\lambda}^T\mathbf{f} + \boldsymbol{\mu}^T\mathbf{g}. \tag{1.25}$$

It is also important, with reference to a physical problem, to define *inequality path constraints* that must be verified at each $t \in [t_i, t_f]$:

[1] in this case it is supposed that the cost function depends only in the final state (e. g. minimize the final time).

$$\mathbf{g}(\mathbf{x}(t), \mathbf{u}(t), t) \geq 0. \tag{1.26}$$

The transcription method discussed basically employs an approximation of the state function derivates, that can be referred to the *Euler method* considering equation (1.18); this step of the problem is a peculiar point for the implementation of the direct method because different strategies of discretization can change the form of the solution significantly. There is a huge number of transcription or *collocation* methods that can be obtained modifying the approaches to the derivate's approximation: one of the most consolidated is the *Randau collocation method* employed in the software GPOPS-II.

1.3.1 GPOPS-II

GPOPS-II, that stands for *General Purpose Optimal Control Software*, represents a robust implementation of the direct methods for the solution of optimal control problems [5]; the software takes advantage of a MATLAB integration that allows the user to build the problem defining the fundamental parameters and functions that describe the system dynamics.
The software has its core in the first and final steps of the direct optimal control problem, or rather the *transcription method* and the *control of the accuracy* of the results with a possible *mesh refinement*; the "real" optimization, or rather the solution of the problem reached optimizing the variables, is actually performed by the *solver* such as IPOPT (sec. 1.3.2) or SNOPT.
In general an optimal control problem can be described with a finite number of phases P; for each phase p is also defined a series of equations which, only in part, have just been taken into consideration in the previous paragraphs. In addition to the dynamic constraints from (1.7) and the inequality constraints from (1.26), it is important to consider also the *event constraints* that relate the beginning and the end of each phase,

$$\mathbf{b}_{min} \leq \mathbf{b}(\mathbf{e}^{(p)}, \mathbf{s}) \leq \mathbf{b}_{max}, \tag{1.27}$$

the *static parameter constraints*

$$\mathbf{s}_{min} \leq \mathbf{s} \leq \mathbf{s}_{max}, \tag{1.28}$$

and the *integral constraints*

$$\mathbf{q}_{min}^{(p)} \leq \mathbf{q}^{(p)} \leq \mathbf{q}_{max}^{(p)}, \tag{1.29}$$

with

$$\mathbf{e}^{(p)} = [\mathbf{x}^{(p)}(t_i^{(p)}), t_i^{(p)}, \mathbf{x}^{(p)}(t_f^{(p)}), t_f^{(p)}, \mathbf{q}^{(p)}], \tag{1.30}$$

and

$$q_i^{(p)} = \int_{t_i^{(p)}}^{t_f^{(p)}} y_i^{(p)}(\mathbf{x}^{(p)}, \mathbf{u}^{(p)}, t^{(p)}, \mathbf{s})\, dt \quad i = 1, \ldots, n_q^{(p)};\ p = 1, \ldots, P. \tag{1.31}$$

Considering now for simplicity a single-phase problem, in order to employ the collocation method, it is fundamental to define each function in terms of a new independent variable $\tau \in [-1, 1]$, while t becomes:

$$t = \frac{t_f - t_i}{2}\,\tau + \frac{t_f - t_i}{2}; \tag{1.32}$$

in other terms the independent variable is now dimensionless, with a variation between -1 and 1.
The interval considered is furthermore divided into K sub-intervals $[T_{k-1}, T_k]$ with $k = 1, \dots K$ and T_k are the *mesh points* in which it will be calculated the solution. The proper discretization of the problem is implemented by GPOPS using the *Randau quadrature orthogonal collocation method* with the following approximation, valid in each interval k:

$$\mathbf{x}^{(k)} \approx \mathbf{X}^{(k)}(\tau) = \sum_{j=1}^{N_k+1} \mathbf{X}_j^{(k)}\, l_j^{(k)}, \tag{1.33}$$

$$l_j^{(k)}(\tau) = \prod_{l=1}^{N_k+1} \frac{\tau - \tau_l^{(k)}}{\tau_j^{(k)} - \tau_l^{(k)}}, \quad l \neq j, \tag{1.34}$$

$\tau, l_j^{(k)}(\tau), j = 1, \dots, N_k{+}1$ is a basis of *Lagrange polynomials*, while $\tau_1^{(k)}, \dots, \tau_{N_k}^{(k)}$ are the *Legendre-Gauss-Randau* (LGR) collocation points with $\tau^{(k)} \in [T_{k-1}, T_k)$.
Considering now a convenient formulation of the state constraints, employing the new independent variable:

$$\frac{d\mathbf{x}^{(k)}(\tau^{(k)})}{d\tau^{(k)}} = \frac{t_f - t_i}{2}\,\mathbf{f}(\mathbf{x}^{(k)}(\tau^{(k)}), \mathbf{u}^{(k)}(\tau^{(k)}), \tau^{(k)}, t_i, t_f), \tag{1.35}$$

and differentiating in the same way $\mathbf{X}^{(k)}(\tau)$ the result is:

$$\frac{d\mathbf{X}^{(k)}(\tau)}{d\tau} = \sum_{j=1}^{N_k+1} \mathbf{X}_j^{(k)} \frac{d\, l_j^{(k)}(\tau)}{d\tau}; \tag{1.36}$$

introducing the approximation in equation (1.35), or rather collocating the dynamics at the LGR points the result is

$$\sum_{j=1}^{N_k+1} D_{ij}^{(k)} \mathbf{X}_j^{(k)} - \frac{t_f - t_i}{2}\,\mathbf{f}(\mathbf{X}_i^{(k)}, \mathbf{U}_i^{(k)}, \tau^{(k)}, t_i, t_f) = \mathbf{0}, \tag{1.37}$$

where $\mathbf{U}_i^{(k)}$ represents the approximation of the controls and $D_{ij}^{(k)}$ is an element of the *LGR differentiation matrix*:

$$D_{ij}^{(k)} = \left[\frac{d\, l_j^{(k)}(\tau)}{d\tau}\right]_{\tau_i^{(k)}}. \tag{1.38}$$

Furthermore, also the other constraint relations are made discrete, coherently with the states and controls; the path constraints become

$$\mathbf{g}_{min} \leq \mathbf{g}(\mathbf{X}_i^{(k)}, \mathbf{U}_i^{(k)}, \tau^{(k)}, t_i, t_f) \leq \mathbf{g}_{max}, \tag{1.39}$$

while the integral constraints are traduced using the *LGR quadrature weights* $w_j^{(k)}, j = 1, \ldots, N_k$ as follows:

$$q_j \approx \sum_{k=1}^{K} \sum_{i=1}^{N_k} \frac{t_f - t_i}{2} w_i^{(k)} y_j(\mathbf{X}_i^{(k)}, \mathbf{U}_i^{(k)}, \tau^{(k)}, t_i, t_f); \tag{1.40}$$

the events constraints becomes

$$\mathbf{b}_{min} \leq \mathbf{b}(\mathbf{X}_1^{(1)}, t_i, \mathbf{X}_{N_{k+1}}^{(K)}, t_f, \mathbf{q}) \leq \mathbf{b}_{max}, \tag{1.41}$$

where $\mathbf{X}_1^{(1)}$ and $\mathbf{X}_{N_{k+1}}^{(K)}$ represents the state functions calculated at the beginning and at the end of the time interval of the simulation respectively. It is important to notice that the continuity in each sub-interval must be constrained considering the identity $\mathbf{X}_{N_{k+1}}^{(k)} = \mathbf{X}_1^{(k+1)}$: these further equations are actually eliminated from the problem because the software uses the same variable for both these values.
The transcription method described represents only the first step of the direct implementation; the problem is then built up generalizing the formulation for all the phases and summarizing the equations in form of vector and matrices that must interface with the solver. This re-formulation will be omitted because it goes beyond the purposes of this work.
Moreover GPOPS, after calling the solver and presenting the conveniently-written equations to obtain the optimal solution, provides the final step of the method: it consists in the check of the accuracy and the consequent refinement of the mesh in order to reach the desired level of reliability of the solution defined by the user-specified tolerance. This step is implemented trough an *adaptive hp refinement method* that allows a variation of the number of mesh intervals, the width of each interval and the degree of the Lagrange polynomial which approximate the functions, in order to give a proper integration of the equations. The estimate of the solution error, that must be compared with the tolerance defined for the problem, is calculated using a relative difference between the state estimate and the integral of the dynamics obtained after modifying the set of LGR points; summing up, in GPOPS are implemented two different strategies to achieve a refinement of the mesh: if the estimate of the polynomial degree is lower than the user-defined limit, the method increases the polynomial degree within a mesh interval or, in other words, generates a denser number of sub-intervals; differently, if the upper allowed limit for the polynomial degree is exceeded, the software provides an increment of mesh intervals.
Another important aspect to underline is represented by the scaling of the NLP problem, that allow a faster and more robust convergence to the optimal solution: the software employs an automatic scaling approach, that transforms a generic variable $x \in [a, b]$ to a new scaled variable $\tilde{x} \in [-1/2, 1/2]$ considering the following expressions:

$$\tilde{x} = v_x x + r_x, \tag{1.42}$$
$$v_x = \frac{1}{b-a}, \tag{1.43}$$
$$r_x = \frac{1}{2} - \frac{b}{b-a}. \tag{1.44}$$

1.3.2 IPOPT

IPOPT (*Interior Point Optimizer*) performs the real optimization process that follows the transcription computed by GPOPS; the fundamental principle that stays behind the solver is to allow convergence using exact merit functions to enforce progress toward solution [6]. An alternative to this approach is a *filter method* that accepts the trial points if they improve the objective function or reduce the constraint violation separately; IPOPT implements a further method that adapts the filter approach to barrier methods and performs the validity of trial steps, considering the norm of the optimality conditions.
With reference to a simplified problem formulated as follows:

$$\min \mathcal{F}(\mathbf{x}), \quad \mathbf{x} \in \mathbb{R}^n \tag{1.45}$$
$$\mathbf{g}(\mathbf{x}) = 0, \tag{1.46}$$
$$\mathbf{x} \geq 0, \tag{1.47}$$

the interior point method computes approximate solutions for a sequence of barrier problems defined as

$$\min \boldsymbol{\psi}_\mu(\mathbf{x}) \doteq \mathcal{F}(\mathbf{x}) - \mu \sum_{i=1}^{n} \ln(x_i), \tag{1.48}$$
$$\mathbf{g}(\mathbf{x}) = 0; \tag{1.49}$$

these equations are defined for a sequence of μ, called the *barrier parameter*, which is driver to zero; equivalently,

$$\nabla \mathcal{F}(\mathbf{x}) + \nabla \mathbf{g}(\mathbf{x})\boldsymbol{\lambda} - \mathbf{z} = 0, \tag{1.50}$$
$$\mathbf{g}(\mathbf{x}) = 0, \tag{1.51}$$
$$\mathrm{diag}(\mathbf{x})\,\mathrm{diag}(\mathbf{z})\mathbf{e} - \mu\mathbf{e} = 0, \tag{1.52}$$

where $\mathrm{diag}(\mathbf{x})$ and $\mathrm{diag}(\mathbf{z})$ give two diagonal matrixes in which the elements are elements of $\mathbf{x}$ and $\mathbf{z}$ respecitvely, while $\mathbf{e}$ is a vector of ones; $\boldsymbol{\lambda} \in \mathbb{R}^m$ and $\mathbf{z} \in \mathbb{R}^n$ are the Lagrangian multipliers for the equality constraints and the inequality constraints respectively. This set of equations, for $\mu \to 0$, represents the *optimality conditions* for the considered problem if the constraints are satisfied.

The method described implements an approximated solution of the barrier problem considering μ as a constant and decreasing this parameter for the solution of the next barrier. The *optimality error* for the problem can be defined as follows:

$$E_\mu(\mathbf{x}, \boldsymbol{\lambda}, \mathbf{z}) \doteq \max \left\{ \frac{\|\nabla \mathcal{F}(\mathbf{x}) + \nabla \mathbf{g}(\mathbf{x})\boldsymbol{\lambda} - \mathbf{z}\|_\infty}{s_d}, \|\mathbf{g}(\mathbf{x})\|_\infty, \frac{\|\operatorname{diag}(\mathbf{x}) \operatorname{diag}(\mathbf{z})\mathbf{e} - \mu\mathbf{e}\|_\infty}{s_c} \right\}, \tag{1.53}$$

where s_d and s_c are properly defined scaling parameters; evaluating this quantity at $\mu = 0$ makes possible to obtain the *optimality error for the original problem* and definitely a terminal condition for the whole algorithm: in other terms the iterations terminates if the approximate solution $(\mathbf{x}^*, \boldsymbol{\lambda}^*, \mathbf{z}^*)$ satisfies:

$$E_0(\mathbf{x}^*, \boldsymbol{\lambda}^*, \mathbf{z}^*) \leq \epsilon_{tol}, \tag{1.54}$$

with $\epsilon_{tol} > 0$ is the user-defined tolerance for the mesh error.
The solution of the barrier problem can be found, for the k iteration, adopting the Newton's method with the search directions $(\mathbf{d}_k^x, \mathbf{d}_k^\lambda, \mathbf{d}_k^z)$ generated from a linearization of the optimality conditions (1.50), (1.51), (1.52):

$$\begin{bmatrix} W_k & A_k & -I \\ A_k^T & 0 & 0 \\ Z_k & 0 & X_k \end{bmatrix} \begin{pmatrix} \mathbf{d}_k^x \\ \mathbf{d}_k^\lambda \\ \mathbf{d}_k^z \end{pmatrix} = - \begin{pmatrix} \nabla \mathcal{F}(\mathbf{x}_k) + A_k \boldsymbol{\lambda}_k - \mathbf{z}_k \\ \mathbf{g}(\mathbf{x}_k) \\ X_k Z_k \mathbf{e} - \mu_j \mathbf{e} \end{pmatrix}, \tag{1.55}$$

with $Z = \operatorname{diag}(\mathbf{z})$, $X = \operatorname{diag}(\mathbf{x})$, $A_k \doteq \nabla \mathbf{g}(\mathbf{x}_k)$, $W_k = \nabla^2_{xx} \mathcal{L}(\mathbf{x}_k, \boldsymbol{\lambda}_k, \mathbf{z}_k)$ Hessian of the Lagrangian function

$$\mathcal{L}(\mathbf{x}, \boldsymbol{\lambda}, \mathbf{z}) \doteq \mathcal{F}(\mathbf{x}) + \mathbf{g}(\mathbf{x})^T \boldsymbol{\lambda} - \mathbf{z}\,. \tag{1.56}$$

Considering now the step sizes α_k, $\alpha_k^z \in (0, 1]$, it is possible to evaluate the following iterations as

$$\mathbf{x}_{k+1} \doteq \mathbf{x}_k - \alpha_k \mathbf{d}_k^x, \tag{1.57}$$
$$\boldsymbol{\lambda}_{k+1} \doteq \boldsymbol{\lambda}_k - \alpha_k \mathbf{d}_k^\lambda, \tag{1.58}$$
$$\mathbf{z}_{k+1} \doteq \mathbf{z}_k - \alpha_k^z \mathbf{d}_k^z; \tag{1.59}$$

it is important to notice that the determination of the step sizes is fundamental for the progression of the iterative method and the choice of these parameters takes advantage of the *line-search filter method*. This formulation is based on the interpretation of the barrier method as an optimization problem with two separate targets to minimize: the function $\psi_{\mu_j}(\mathbf{x})$ and the entity of the constraint violation $\theta(\mathbf{x})$. A trial point should be considered as "acceptable" if it satisfies for the k iteration the following conditions, for a *backtracking line-search procedure* which allows to explore a decreasing sequence of trial steps sizes $\alpha_{k,l}$:

$$\theta(\mathbf{x}_k(\alpha_{k,l})) \leq (1 - \gamma_\theta)\theta(\mathbf{x}_k), \tag{1.60}$$
$$\psi_{\mu_j}(\mathbf{x}_k(\alpha_{k,l})) \leq \psi_{\mu_j}(\mathbf{x}_k) - \gamma_\psi \theta(\mathbf{x}_k), \tag{1.61}$$

```
iter    objective    inf_pr   inf_du lg(mu)  ||d||  lg(rg) alpha_du alpha_pr  ls
   0  1.6109693e+01 1.12e+01 5.28e-01   0.0 0.00e+00    -  0.00e+00 0.00e+00   0
   1  1.8029749e+01 9.90e-01 6.62e+01   0.1 2.05e+00    -  2.14e-01 1.00e+00f  1
   2  1.8719906e+01 1.25e-02 9.04e+00  -2.2 5.94e-02   2.0 8.04e-01 1.00e+00h  1
```

Figure 1.1: IPOPT console output quantities.

with γ_θ, $\gamma_\psi \in (0, 1)$. Moreover, for each iteration the algorithm sets a filter that defines the prohibited regions for the trial points; initially the formulation is:

$$\Psi_0 \doteq (\theta, \psi) \in \mathbb{R}^2 \, : \, \theta \geq \theta^{max}, \tag{1.62}$$

and is updated as

$$\Psi_{k+1} \doteq \Psi_k \cup \Big\{(\theta, \psi) \in \mathbb{R}^2 \, : \, \theta \geq (1 - \gamma_\theta)\theta(\mathbf{x}_k), \, \psi \leq \psi_{\mu_j}(\mathbf{x}_k) - \gamma_\psi \theta(\mathbf{x}_k)\Big\}. \tag{1.63}$$

IPOPT provides a console tabular output in order to compute an evaluation for the most important parameters connected to the convergence of the problem; in figure (1.1) can be seen an example of the printed quantities.

The meaning of the variables of interest can be summed up as follows:

- *iter*: iteration count;
- *objective*: unscaled objective value at current iteration;
- *inf_pr*: unscaled constraint violation at current iteration, or rather the infinity-norm (maximum) of the constraints;
- *inf_du*: scaled dual infeasibility at current point, or rather the infinity-norm of the internal dual infeasibility expressed at (1.50);
- *lg(mu)*: log_{10} of the barrier parameter μ;
- $\|d\|$: infinity-norm of the primal step;
- *lg(rg)*: depends on log_{10} of regularization of Hessian and Lagrangian;
- *alpha_du*: stepsize of dual variables α_k^z in (1.59);
- *alpha_pr*: stepsize of the primal variables α_k in (1.57);
- *ls*: number of backtracking line search steps.

1.3.3 ADiGator

The evaluation of the objective function gradient, the constraint Jacobian and the Hessian of the Lagrangian is fundamental in order to obtain a solution for the NLP problem; the standard strategy adopted to evaluate these derivatives is the numerical method called finite-differencing: this method employs an approximation determined dividing the difference of the function, evaluated at two neighbor points, by the difference of the same points. Considering a generic function $f(x)$ to evaluate in an interval of length ε:

$$\left.\frac{df}{dx}\right|_x = \frac{f_{x+\varepsilon/2} - f_{x-\varepsilon/2}}{\varepsilon} \tag{1.64}$$

The main advantage of this strategy consists in the fact that only evaluations of the function are required; nevertheless the finite-differencing strongly depends on the spacing between the chosen points: with a large spacing the approximation is coarse, while using small spacing may lead to an improper evaluation of the behavior of the function.
An alternative to this method is based on the target of formulating an efficient and accurate way to compute the needed derivatives automatically: this is known as *automatic differentiation* (AD) [7]. Taking into consideration a differentiable computer program, it may be broken into a sequence of elementary operations, each one connected to a correspondent derivative rule; applying systematically the chain rule to each of the elementary operation rules, it is possible to achieve a derivative with accuracy coincident with machine precision. A MATLAB based tool, implemented in GPOPS, that provides automatic differentiation is *ADiGator*: this package generates a MATLAB program which is capable of computing the possible non-zero derivatives of the original function program. The main advantages given by the tool for the direct optimal control problems are the following:

1. no time penalties are added with the derivative evaluation because the derivative code is only evaluated by MATLAB library;

2. the tool is capable to compute *vectorized* derivatives of the *vectorized* functions which result from the direct collocation method provided by GPOPS: it improves the efficiency;

3. second-order derivatives can be provided simply applying recursively the same procedure.

ADiGator make use of a source transformation via operator overloading in order to determine the derivatives of functions defined by MATLAB programs; in other words the tool works as follows: the inputs to the software consist in a function (that have to be differentiated), the information on the sizes of inputs and the derivative information on the inputs; the operator is overloaded because different operators have different implementations depending on their arguments: the program in fact will be able to recall the functions using different inputs available during the calculations. The algorithm first transforms the given MATLAB

source code into an intermediate code in which are included calls to *ADiGator* specific routines for transformation; this code is then evaluated multiple times using overloaded CADA objects, which include only information on the size of objects, symbolic identifiers and the possible non zero derivative locations. The evaluations and informations obtained are included in functions and derivative files: as result the method provides a transformation of the original user function into a MATLAB function that computes a numerical solution of the non-zero derivatives of the original function. All these consideration are extensively developed in [7].

1.3.4 MATLAB Implementation

The MATLAB code necessary to implement and solve the optimal control problem using GPOPS is subordinate to the creation of a series of quantities, which are fundamental in order to define the main variables and parameters involved:

1. the *endpoint function*;
2. the *continuous function*;
3. lower and upper limits of:
    - the time at start and terminus of a phase;
    - the state at start, during and at the terminus of a phase;
    - the controls during a phase;
    - the path constraint (in all the phases for definition);
    - the event constraints;
    - the static parameters.

If on the one hand the functions are defined separately to the main code and recalled in it to set up the problem, on the other hand the global boundary conditions of the quantities listed must be written in the main code itself. In the *endpoint function* is defined the cost to be minimized, the begin and the end of each phase, the integrals of each phase, and the static parameters related, while in the *continuous function* are provided the dynamics equation in each phase, the integrands and the path constraints in each phase.
For some problems with a high level of complexity it should be provided an initial guess for the solution, building a proper set of values for the time, the states, the controls, the integral and the parameters (if adopted).

1.3.5 Simple Example: The Brachistochrone Problem

In order to clarify the basic structure of the optimal analysis, it might be useful to formalize a simple problem in terms of a practical GPOPS implementation. The physical problem, known as the *brachistocrone problem*, consists in the research of the optimal shape of a wire, that is able to minimize the final time in which an ideal body can drop without friction in a given horizontal distance. In this

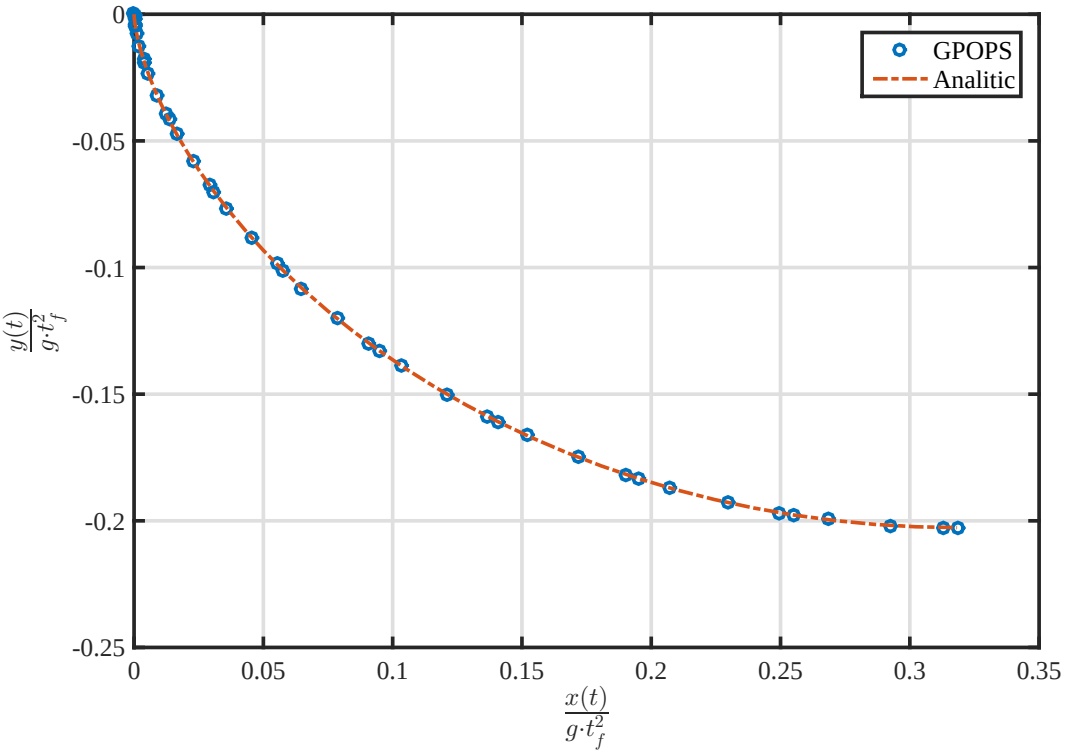

Figure 1.2: Comparison between the GPOPS solution and the analytical solution from [2].

paragraph will be implemented the dual problem of the one just described: the target is to maximize the utter horizontal distance in which the ideal body drops along the wire in a given time t_f; this analysis is taken from [2, p.47]. The problem admits an analytical solution calculated in a discrete number N of states, with $\alpha = \pi/2N$:

$$\frac{x(i)}{gt_f^2} = \frac{\cos(\alpha/2)}{4N^2 \sin(\alpha/2)} \left[\frac{i\, 2\sin(2\alpha i)}{2\sin(\alpha)} \right], \quad i = 1, \ldots, N \tag{1.65}$$

$$\frac{y(i)}{gt_f^2} = \frac{\cos(\alpha/2)}{8N^2 \sin(\alpha/2)\sin(\alpha)} [1 - \cos(2\alpha i)], \quad i = 1, \ldots, N. \tag{1.66}$$

In figure 1.2 should be seen the results of the analytical method and the solution found with GPOPS-II considering the optimal shape of the wire in terms of x and y coordinates, made dimensionless dividing by gt_f^2: the two methods generate the same path. Moreover, it should be highlighted that GPOPS increments the mesh points in proximity of the origin because, in this point, the convergence is made more difficult by the small values of the variables.

1.4 Comparison Between Methods

In spite of the fact that both the direct and indirect methods focus their attention on the research of a minimum for the objective function, these two methods are substantially different in terms of the strategies applied and referring to the quantities that need to be calculated. In general, on the one hand, the direct methods proceed in a discrete domain in order to find a minimum of the cost function; on the other hand the indirect methods are based on the research of a root of the necessary condition and, namely, of a stationery point of the target function. In practice, as shown in the previous paragraphs, indirect methods need the user to derive an explicit formulation of the adjoint equations (1.8), the control equations (1.9) and the transversality conditions (1.10): these steps of calculation are not necessary for a direct formulation; moreover, for this reason, the direct methods allow a complete distinction between the formulation of the physical model and the mathematical formulation of the optimal control problem, that are fundamentally correlated for the indirect approach.
The most significant difficulties connected to the analysis with an indirect method can be synthetically expressed in three points [1, p.129]:

1. the relevant derivatives must be calculated by the user such as $\mathcal{H}_x$ and $\mathcal{H}_u$;
2. path inequalities and junction condition are difficult to estimate: in particular these quantities are substituted by penalties in the cost function;
3. it must be computed a guess for the adjoint variables $\boldsymbol{\lambda}$.

To be more precise, path inequalities are also used in the direct methods while the penalties for the constraint violation are implemented only internally in the solver (e.g. IPOPT): the main difference is that in the indirect methods the user has to obtain an explicit formulation for these penalties, while with direct methods are integrated in the solution program.

Chapter 2

Vehicle Model

2.1 Introduction

The possibility to obtain realistic solutions for the optimal control problem, or rather results that can be assumed as a good approximation of the real behavior of the vehicle, depends on the level of complexity provided for the vehicle dynamic model: the more the model is able to capture the most significant dynamic parameters, the more the simulation is capable of reaching the ideal perfect performance for the real vehicle, in terms of minimum time maneuvers.
Therefore, it is clear that the possibility of finding and modelling the quantities which have a main role in the dynamic behavior, is the real challenge for obtaining a proper solution for the problem; as underlined by the theory of vehicle dynamics, the most important parameters that make the difference between a good level of approximation and a coarse representation of reality are related to the tyre modelling and the slip quantities: this observation represents the main difference between the models that will be presented in the following sections. Further improvements are connected to the introduction of the lateral dynamics and the effect of the road slope.
Despite of that, the simulations have to face with the difficulty introduced for the calculations using complex models with a big deal of state variables and controls. The speed of elaboration is, in most of the cases, an important limit that does not allow the usage of more accurate characterizations for the vehicle dynamics. In fact, the proper model of the system has to be the best compromise between enough fast calculation and a good representation of the vehicle, and it depends on the user necessities: fast simulations must be provided for an almost "real time" comparison with the running vehicle, while slower calculations can be used during the phase of design and test.
The main models that will be treated later are:

- *basic* model with constant *traction ellipses*: in this model the tyre forces are constrained to remain in the traction ellipses limits, in order to simulate the coupling between longitudinal and lateral forces;
- *slip-slip* model with longitudinal and lateral slip: forces are limited to the slip limit value; a more proper coupling is therefore provided;

As noticed before, the real difference between these models is connected to the tyre modelling, although other dynamic behaviors are taken into consideration, such as the lateral load transfer or the effect of the road slope.
All the simulations will be developed using the data of a real racing car of the GT3 Italian championship: the BMW M6 GT3. In terms of modelling, the vehicle is characterized by a rear wheel drive transmission, with front engine and rear gearbox positioning; the driving axle includes a self-locking differential and the car is also equipped by a rear adjustable wing. For confidentiality reasons, the technical data will not be reported in this dissertation.

2.2 Basic Car Model

The first basic model departs from a *single-track model* in which the tyre forces are constrained to stay into constant and user-defined adherence ellipses; in that way it is provided a simple combination of the forces, which are obtained with an elementary *saturating force model*: for high or low slips the force saturates to its maximum (or minimum) value. A *single-track model* is basically a vehicle approximation equipped only by one rear wheel and one steering front wheel; differently, in this basic model, all the four wheels are considered dividing equally the front and rear forces for the wheels of the front and rear axle respectively.

2.2.1 Kinematics

Consider now two reference frames: an XYZ absolute reference frame, with Z axis directed towards the ground (SAE convention), and a moving reference frame xyz, with origin in the centre of mass (CoM), x axis directed along the longitudinal axis of symmetry of the vehicle, and z axis directed towards the ground (SAE convention); the moving frame is instantly rotated around the z axis of an angle $\psi(t)$, called *yaw angle*, and is subjected to a translational movement with velocity $\mathbf{V}(\mathbf{t}) = [u(t), v(t), 0]$, which corresponds to the velocity of the vehicle. A representation of these kinematic parameters is realized in fig. 2.1.

Applying now the Poisson fundamental equation for kinematics (2.1), the expression of tyre velocities can be found, where $\boldsymbol{\omega}(t)$ is the angular velocity matrix for the moving frame while $\mathbf{r}$ is the vector directed from the CoM to the wheel centre of mass.

$$\mathbf{V}_{wheel} = \mathbf{V} + \boldsymbol{\omega} \wedge \mathbf{r}; \tag{2.1}$$

$$\begin{pmatrix} u_{fr} \\ v_{fr} \end{pmatrix} = \begin{pmatrix} u \\ v \end{pmatrix} + \begin{pmatrix} 0 & -\dot{\psi} \\ \dot{\psi} & 0 \end{pmatrix} \begin{pmatrix} a \\ \frac{T}{2} \end{pmatrix} = \begin{pmatrix} -\dot{\psi}\,\frac{T}{2} + u \\ \dot{\psi}\,a + v \end{pmatrix}; \tag{2.2}$$

then the *trim angle* β_w, or rather the angle between the wheel velocity and the x axis of the moving reference frame, can be expressed as follows:

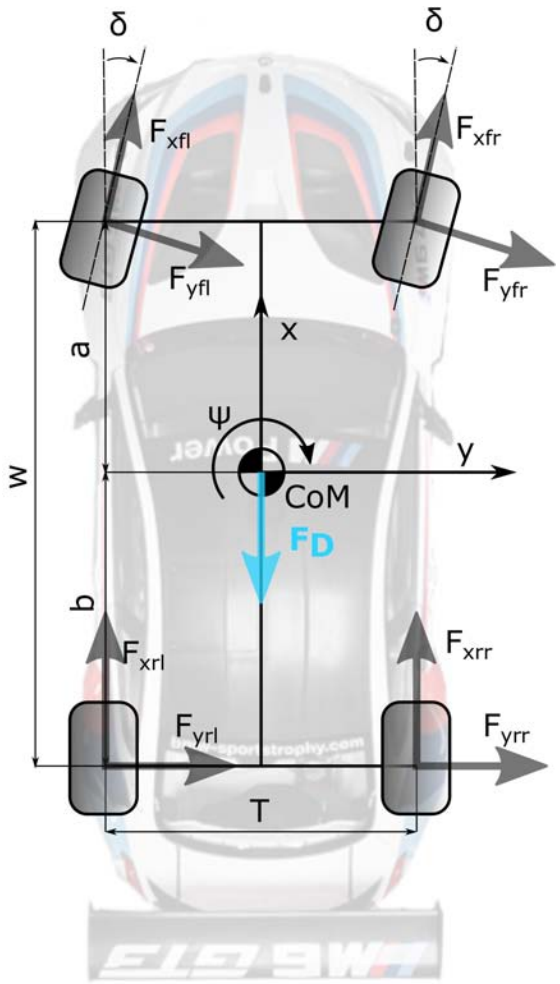

Figure 2.1: View of the vehicle in xy plane.

$$\beta_{fr} \approx \tan\beta_{fr} = \frac{\dot{\psi}\,a + v}{-\dot{\psi}\,\frac{T}{2} + u}. \tag{2.3}$$

The same calculations can be made for the other wheels:

$$\begin{pmatrix} u_{fl} \\ v_{fl} \end{pmatrix} = \begin{pmatrix} \dot{\psi}\,\frac{T}{2} + u \\ \dot{\psi}\,a + v \end{pmatrix} \qquad \rightarrow \qquad \beta_{fl} \approx \frac{\dot{\psi}\,a + v}{\dot{\psi}\,\frac{T}{2} + u}, \tag{2.4}$$

$$\begin{pmatrix} u_{rr} \\ v_{rr} \end{pmatrix} = \begin{pmatrix} -\dot{\psi}\,\frac{T}{2} + u \\ -\dot{\psi}\,b + v \end{pmatrix} \qquad \rightarrow \qquad \beta_{rr} \approx \frac{-\dot{\psi}\,b + v}{-\dot{\psi}\,\frac{T}{2} + u}, \tag{2.5}$$

$$\begin{pmatrix} u_{rl} \\ v_{rl} \end{pmatrix} = \begin{pmatrix} \dot{\psi}\,\frac{T}{2} + u \\ -\dot{\psi}\,b + v \end{pmatrix} \qquad \rightarrow \qquad \beta_{rl} \approx \frac{-\dot{\psi}\,b + v}{\dot{\psi}\,\frac{T}{2} + u}. \tag{2.6}$$

All these formulas derive from a linear approximation assuming small values for the trim angle; a further approximation can be obtained considering that realistically $u \gg \dot{\psi}\,T/2$:

$$\beta_{fl} \approx \beta_{fr} \approx \beta_f = \frac{\dot{\psi}\,a + v}{u}, \qquad \beta_{rl} \approx \beta_{rr} \approx \beta_r = \frac{-\dot{\psi}\,b + v}{u}; \tag{2.7}$$

Then it is evident that the trim angles are equal for the wheels of the same axle; moreover the *steering angles* δ for the front wheels can be approximated as equal ($\delta_{fl} \approx \delta_{fr} \approx \delta$): this is more realistic for high speeds.
Thanks to the *congruence* equations, it is possible to express a relation between the trim angles β and the *lateral slip angles* λ, from which it can be obtained the lateral tyre forces. These fundamental slip quantities are defined as the angles between the wheel velocity (due to translation and rotation around z) and the axis of symmetry of the wheel (fig. 2.2).

$$\lambda_f = \delta - \beta_f = \delta - \frac{\dot{\psi}\,a + v}{u}, \qquad \lambda_r = -\beta_r = -\frac{-\dot{\psi}\,b + v}{u}. \tag{2.8}$$

2.2.2 Dynamics

Each wheel is subjected to a force vector $[F_x, F_y, N]_w$ composed by longitudinal and lateral tyre forces, and the normal loads N; the point of application of these forces is the ideal contact point of the wheels, assuming that this point is coincident to the projection of the wheel centre to the ground. The longitudinal forces can be divided into two different contributes: a front longitudinal force F_{xf} for the front wheels and a rear longitudinal force F_{xr} for the rear wheels; F_{xf} can be only negative and exists during a braking condition, while F_{xr} represents the positive driving force during acceleration and the negative contribution during braking. Only when the driver presses the brake pedal, the front and rear forces are related by equation (2.9) in which is expressed the braking ratio β. F_x is the total longitudinal force applied, namely the sum of each force applied on the wheel contact points.

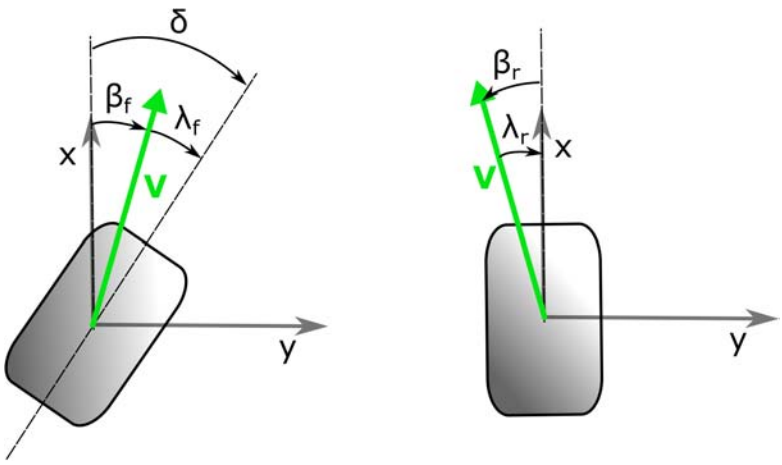

Figure 2.2: Relations between the steering angle, the slip angle and the trim angle for a front wheel (on the left) and a rear wheel (on the right).

$$\begin{cases} F_{xf} = 0 \\ F_{xr} > 0 \end{cases} \quad F_x > 0 \text{ (traction)}, \qquad \begin{cases} F_{xf} = \beta\, F_x \\ F_{xr} = (1-\beta)\, F_x \end{cases} \quad F_x < 0 \text{ (braking)}. \tag{2.9}$$

The lateral forces are obtained from a simple formulation of a saturated force; this particular form does not take into consideration the coupling between the longitudinal and lateral forces:

$$F_{yf} = \frac{K_f \lambda_f N_f}{\sqrt{1 + \dfrac{K_f^2 \lambda_f^2}{D_{yf}^2}}}, \qquad F_{yr} = \frac{K_r \lambda_r N_r}{\sqrt{1 + \dfrac{K_r^2 \lambda_r^2}{D_{yr}^2}}}; \tag{2.10}$$

where K represents the slope of the curve at $\lambda = 0$ and D_y is the maximum value for saturation, defined by the ratio F_y/N for $\lambda \to \infty$. As it can be deduced, D_y represents the friction coefficient related to the tyre lateral behavior. An explicative representation of the forces depending on the lateral slip angle is highlighted in figure 2.3.
It should be noticed also that in this model the front and rear forces on the contact points, are equally split to the wheels of the same axle, both for the longitudinal and for the lateral ones; in fact the force vectors for each wheel can be expressed as follows:

$$\mathbf{F}_{fl} = \mathbf{F}_{fr} = \left[\frac{1}{2}F_{xf},\, \frac{1}{2}F_{yf},\, \frac{1}{2}N_f\right], \qquad \mathbf{F}_{rl} = \mathbf{F}_{rr} = \left[\frac{1}{2}F_{xr},\, \frac{1}{2}F_{yr},\, \frac{1}{2}N_r\right]. \tag{2.11}$$

Moreover the model takes into consideration the *drag force* applied to the ground projection (G) of the CoM; this choice is related to the fact that the aerodynamics forces are typically measured positioning the vehicle on inertial supports with dynamometric sensors. As suggested by eq. (2.12), this force depends on the

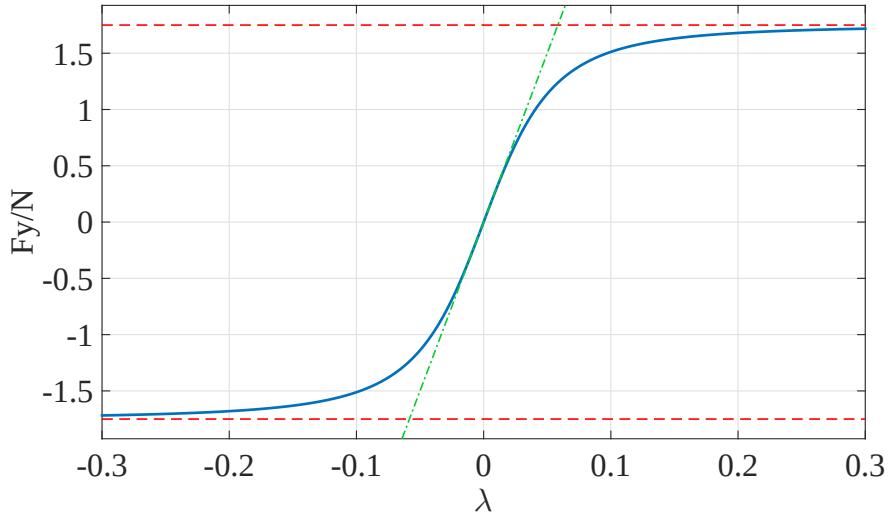

Figure 2.3: Representation of the forces calculated with the saturation formulas; the dashed lines represents the parameter D_y while the dot-dash line has equation $K\,\lambda$ and is coincident with the tangent at the origin of F_y/N.

drag area $C_D A$, obtained by the product of the *drag coefficient* C_D and the *frontal area* A, and on the air density ρ and the longitudinal speed u.

$$F_D = -\frac{1}{2}\, C_D A\, \rho\, u^2. \tag{2.12}$$

Thanks to this considerations, it is possible to formulate the Newton-Euler equations of the system, considering the xy plane; note that $F_y = F_{yf} + F_{yr}$ and $F_x = F_{xf} + F_{xr}$.

$$\left(-\dot{\psi}\, v + \dot{u}\right) m + \frac{1}{2}\, C_D A\, \rho\, u^2 - F_x + F_{yf}\, \delta = 0, \tag{2.13}$$

$$m(\dot{\psi}\, u + \dot{v}) - F_y - F_{xf}\, \delta = 0, \tag{2.14}$$

$$I_z\, \ddot{\psi} - a\, F_{yf} + b\, F_{yr} - a\, \delta\, F_{xf} = 0; \tag{2.15}$$

Equation (2.13) represents the force equilibrium in x direction, eq. (2.14) the force equilibrium in y direction and eq. (2.15) the momentum equilibrium around z axis; I_z is the inertia momentum of the vehicle with reference to z axis.
From this set of equations can obtained the *state space* expression of the dynamical system: this step is fundamental in order to define the *state variables* of the optimal control problem.

$$\dot{u} = \dot{\psi}\, v - \frac{1}{2}\, \frac{C_D A\, \rho\, u^2}{m} + \frac{F_x}{m} - \frac{F_{yf}\, \delta}{m}, \tag{2.16}$$

$$\dot{v} = -\dot{\psi}\, u + \frac{F_y + F_{xf}\, \delta}{m}, \tag{2.17}$$

$$\ddot{\psi} = \frac{a\, F_{yf} - b\, F_{yr} + a\, F_{xf}\, \delta}{I_z}. \tag{2.18}$$

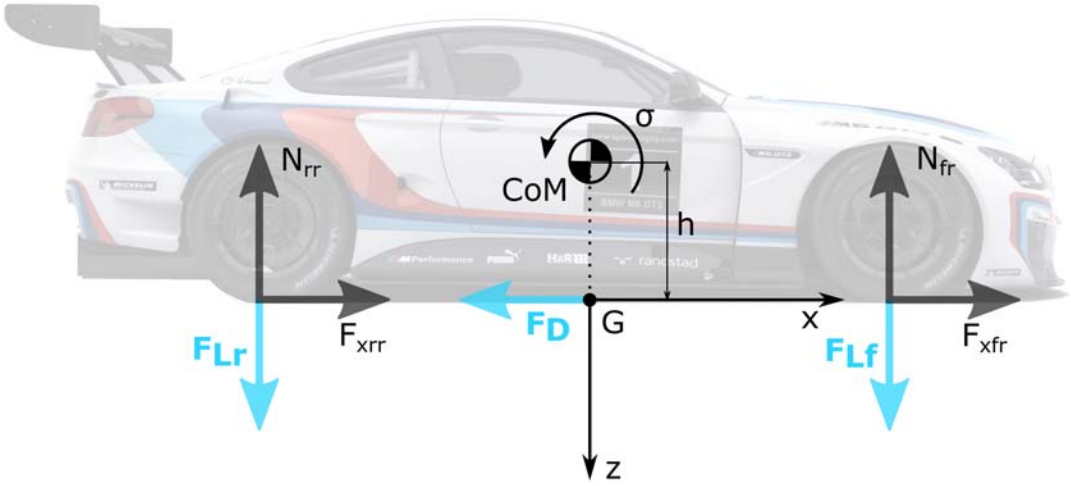

Figure 2.4: View of the vehicle in zx plane.

In this first model the total front and rear loads N_f and N_r are formulated considering only the longitudinal load transfer; they can be deduced from the following simple equations, directly obtained considering the Euler equations around y direction with the pivot at the front and rear contact point respectively;

$$N_f = -\frac{b\,m\,g - h\,(F_{xf} + F_{xr})}{w}, \quad N_r = -\frac{a\,m\,g + h\,(F_{xf} + F_{xr})}{w}. \tag{2.19}$$

As can be seen in figure (2.4), b is the distance between the rear axle and G, a is the distance between the front axle and G, $w = a + b$ is the wheelbase of the vehicle and h is the height of the CoM measured from the ground ($\overline{GCoM}$); it can be noticed that the normal loads are directed oppositely to the z axis and that, for this model, $N_{fl} = N_{fr} = N_f/2$ and $N_{rl} = N_{rr} = N_r/2$.

2.2.3 Further Complications

The basic traction ellipses model would result more realistic considering the lift downforce and lateral load transfer; as for the lift forces (see fig. 2.4), they can be calculated in analogy with the drag force; it should be underlined that the direction is opposite to the z axis:

$$F_{Lf} = -\frac{1}{2}\,C_{Lf} A\,\rho\,u^2, \qquad F_{Lr} = -\frac{1}{2}\,C_{Lr} A\,\rho\,u^2; \tag{2.20}$$

these forces are applied respectively to the front and rear projection of the axle centers on the ground and depend on the *lift areas*, or rather on the product between the *lift coefficient* and the *resistant area* for lift. The parameter $C_L A$ is calculated using the same dynamometric support of the drag coefficient; this choice determines the points of application.

The analysis of the lateral load transfer depends on the roll properties of the vehicle and, in particular, on the front and rear roll stiffness $K_{\phi f}$ and $K_{\phi r}$, calcu-

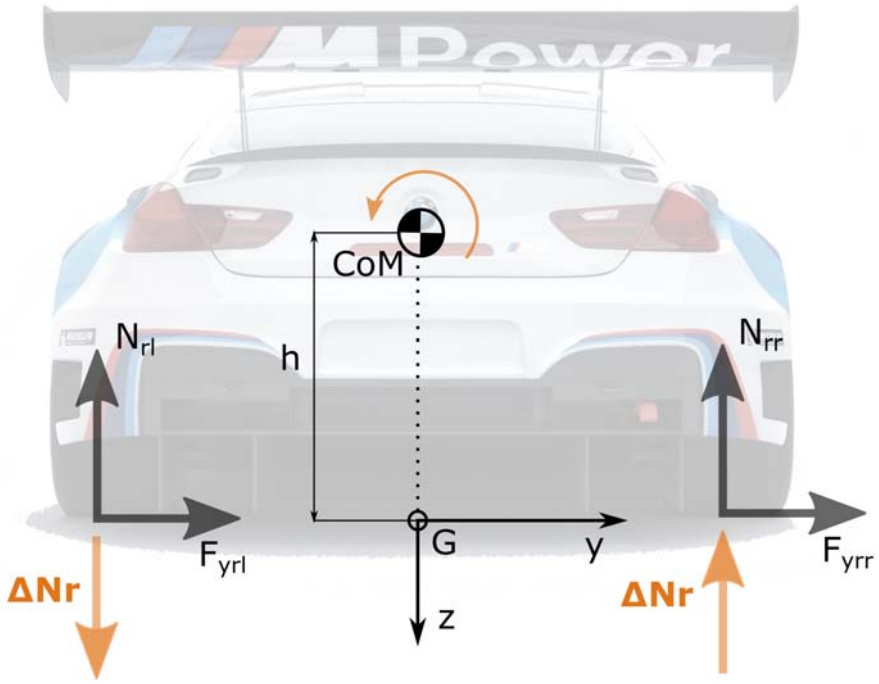

Figure 2.5: View of the vehicle in yz plane with lateral load transfer for the rear wheels.

lated considering a rotation of the vehicle around the roll centers. With reference to figure (2.5), it is possible to approximate the centers of rotation of the vehicle at the same height h of the CoM, and then formulate an equation that express the effect of the roll stiffness on the load transfer. Considering that the *roll stiffness ratio* ξ is defined as:

$$\xi = \frac{K_{\phi f}}{K_\phi}, \qquad \text{with} \quad K_\phi = K_{\phi f} + K_{\phi r}, \tag{2.21}$$

and expressing the lateral load transfer ΔN in function of ξ with the momentum equilibrium around the projection points of the approximated stiffness centers on the ground (coincident with G in the yz plane), can be found the following expressions for front and rear load transfer (fig. 2.5):

$$\begin{cases} \Delta N_f \, T = m \, a_y \, h \, \xi \\ \Delta N_r \, T = m \, a_y \, h \, (1 - \xi) \end{cases}, \qquad \text{with} \quad \begin{cases} \Delta N_f = \frac{1}{2}(N_{fl} - N_{fr}) \\ \Delta N_r = \frac{1}{2}(N_{rl} - N_{rr}) \end{cases}. \tag{2.22}$$

One of these roll equation, in combination with the Newton equation in z direction and the Euler equations around x and y axes, allows to obtain an expression for the loads applied on each wheel. From the system:

$$-hma_y + \frac{1}{2}T\left(N_{fl} - N_{fr} + N_{rl} - N_{rr}\right) = 0, \quad (2.23)$$

$$-\frac{1}{2}aC_{Lf}A\,\rho\,u^2 + \frac{1}{2}bC_{Lr}A\,\rho\,u^2 + hma_x + aN_{fl} + aN_{fr} - bN_{rl} - bN_{rr} = 0, \quad (2.24)$$

$$\frac{1}{2}C_{Lf}A\,\rho\,u^2 + \frac{1}{2}C_{Lr}A\,\rho\,u^2 + mg - N_{fl} - N_{fr} - N_{rl} - N_{rr} = 0, \quad (2.25)$$

$$\frac{1}{2}\left(N_{fl} - N_{fr}\right)T - hma_y\,\xi = 0, \quad (2.26)$$

it follows the wheel normal loads:

$$N_{fl} = -\frac{1}{2}\frac{hma_x}{w} + \frac{1}{2}\frac{bmg}{w} + \frac{1}{4}C_{Lf}A\,\rho\,u^2 + \frac{hma_y\,\xi}{T}, \quad (2.27)$$

$$N_{fr} = -\frac{1}{2}\frac{hma_x}{w} + \frac{1}{2}\frac{bmg}{w} + \frac{1}{4}C_{Lf}A\,\rho\,u^2 - \frac{hma_y\,\xi}{T}, \quad (2.28)$$

$$N_{rl} = \frac{1}{2}\frac{hma_x}{w} + \frac{1}{2}\frac{agm}{w} + \frac{1}{4}C_{Lr}A\,\rho\,u^2 + \frac{hma_y\,(1-\xi)}{T}, \quad (2.29)$$

$$N_{rr} = \frac{1}{2}\frac{hma_x}{w} + \frac{1}{2}\frac{agm}{w} + \frac{1}{4}C_{Lr}A\,\rho\,u^2 - \frac{hma_y\,(1-\xi)}{T}. \quad (2.30)$$

Because of the effect of lateral load transfer, the loads and consequently the lateral forces on the same axle are different: in order to follow the same representation of the previous model, expressed in eq. (2.11), by contrast are reported the following force vectors:

$$\mathbf{F}_{fl} = \left[\frac{1}{2}F_{xf},\, F_{yfl},\, N_{fl}\right], \qquad \mathbf{F}_{fr} = \left[\frac{1}{2}F_{xf},\, F_{yfr},\, N_{fr}\right]; \quad (2.31)$$

$$\mathbf{F}_{rl} = \left[\frac{1}{2}F_{xr},\, F_{yrl},\, N_{rl}\right], \qquad \mathbf{F}_{rr} = \left[\frac{1}{2}F_{xr},\, F_{yrr},\, N_{rr}\right]. \quad (2.32)$$

The acceleration of the CoM, that appear in the load transfer expressions, can be calculated from a derivation of the velocity $\mathbf{V} = [u(t), v(t), 0]$ using the Poisson formulas:

$$\mathbf{A}_{CoM} = [a_x, a_y, 0] = [\dot{u} - v\,\dot{\psi},\, \dot{v} + u\,\dot{\psi},\, 0]. \quad (2.33)$$

Relaxation equations can be provided for a_x and a_y in order to allow a representation of the suspension dynamics: in fact this approximation traduces the accelerations expressions into a low-pass filter, which generate a delay in the application of the tyre forces; starting from the Newton equations towards x and y axes, combined with the (2.33), it can be found the expression for the acceleration components, that are made equal to the filter expression (left hand side of eq. (2.34) and (2.36)) using the parameters τ_{ax} and τ_{ay}, which are connected to the filter cutting frequency.

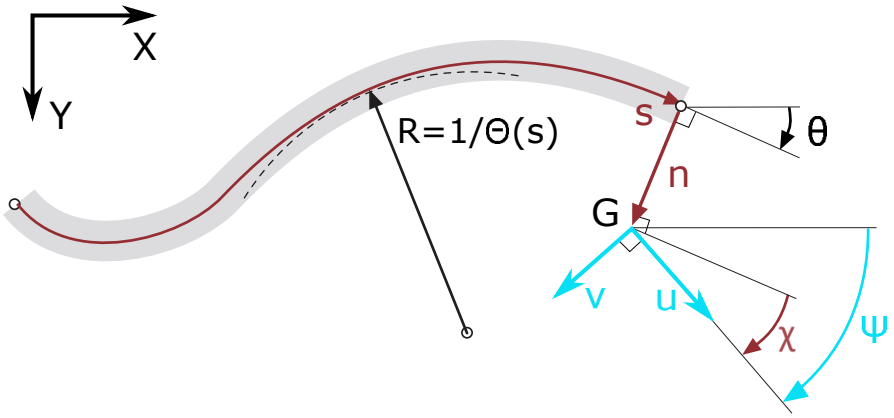

Figure 2.6: Curvilinear coordinates.

$$\tau_{ax}\,\dot{a}_x + a_x = -\frac{1}{2}\,\frac{C_D A\,\rho\,u^2}{m} - \frac{\delta F_{yfl} + \delta F_{yfr} - F_{xf} - F_{xr}}{m}, \tag{2.34}$$

$$\dot{a}_x = -\frac{1}{2}\,\frac{C_D A\,\rho\,u^2}{m\,\tau_{ax}} - \frac{\delta F_{yfl} + \delta F_{yfr} + m a_x - F_{xf} - F_{xr}}{m\,\tau_{ax}}, \tag{2.35}$$

$$\tau_{a_y}\dot{a}_y + a_y = \frac{\delta F_{xf} + F_{yfl} + F_{yfr} + F_{yrl} + F_{yrr}}{m}, \tag{2.36}$$

$$\dot{a}_y = \frac{\delta F_{xf} - m a_y + F_{yfl} + F_{yfr} + F_{yrl} + F_{yrr}}{m\,\tau_{ay}}. \tag{2.37}$$

It is important to underline that the *relaxation equations*, although are implemented to simulate a delay in the lateral and longitudinal load transfer, can boost the convergence of the optimal control problem, with a proper choice of the typical time constants τ_{ax} and τ_{ay}.
The inclusion of these behaviors, related to the lateral dynamics and the lift forces, does not change the formulation of the Newton-Euler equation for xy plane and the state space expression, because no forces are added to the plane of interest.

2.2.4 Curvilinear Coordinates

In order to model the behavior of the vehicle on the track, and then obtain its position on the road, it is fundamental to consider the *curvilinear coordinates*. For a xy planar problem, the equations of curvilinear coordinates can be easily deduced projecting the velocities of the moving frame xyz on the road frame; the road frame is defined by three curvilinear coordinates: the versor $s(t)$ is the *curvilinear abscissa* and is instantly tangent to the centre of the road, $n(t)$ is a versor perpendicular to $s(t)$ and $\chi(t)$ represents the rotation of this frame around the orthogonal to the ground plane and directed downwards (fig. 2.6). Equation (2.40) is obtained form the definition of the *road curvature* $\Theta(s)$, which is a function of the curvilinear abscissa.

$$\cos(\chi)\ u - \sin(\chi)\ v = -\left(\dot{\psi} - \dot{\chi}\right) n + \dot{s}, \tag{2.38}$$

$$\sin(\chi)\ u + \cos(\chi)\ v = \dot{n}, \tag{2.39}$$

$$\frac{\dot{\psi} - \dot{\chi}}{\Theta(s)} = \dot{s}. \tag{2.40}$$

The explicit formulation of these equations, or rather the *state space* representation, is useful in order to set up the optimal control problem.

$$\dot{s} = -\frac{\cos(\chi)\, u - \sin(\chi)\, v}{n\Theta(s) - 1}, \tag{2.41}$$

$$\dot{n} = \sin(\chi)\, u + \cos(\chi)\, v, \tag{2.42}$$

$$\dot{\chi} = \frac{\cos(\chi)\,\Theta(s)\, u - \sin(\chi)\,\Theta(s)\, v + n\Theta(s)\,\dot{\psi} - \dot{\psi}}{n\Theta(s) - 1}. \tag{2.43}$$

2.2.5 3D Road

A model that implements the effects of the variation of the road slope σ is then provided, starting from the basic model of car; this model represents a simplified version of a complete 3D model because no variation of z coordinate is considered, as if the vehicle underwent the effects of slope with only a *pitch* rotation around the y axis, maintaining the same elevation in the whole domain. Therefore no changes are expected for the Newton equation along the y axis (2.45) and for the Euler equation around z (2.46) axis, while the force equilibrium along x axis (2.44) has to include the effect of gravity $mg\sin\sigma$; consequently the xy plane dynamics is captured solving the following equations:

$$-\dot{\psi} m v + m\dot{u} + \frac{1}{2} C_D A \rho u^2 + mg\sin\sigma - F_{xf} - F_{xr} + (F_{yfl} + F_{yfr})\,\delta = 0, \tag{2.44}$$

$$\dot{\psi} m u + m\dot{v} - F_{yfl} - F_{yfr} - F_{yrl} - F_{yrr} - \delta F_{xf} = 0, \tag{2.45}$$

$$I_z\,\ddot{\psi} - aF_{yfl} - aF_{yfr} + bF_{yrl} + bF_{yrr} + \left(\frac{1}{2} T F_{yfl} - aF_{xf} - \frac{1}{2} T F_{yfr}\right)\delta = 0; \tag{2.46}$$

the accelerations, treated as a low-pass filter, become:

$$\dot{a}_x = -\frac{1}{2}\,\frac{C_D A \rho u^2 + 2\, mg\sin\sigma + 2\,\delta F_{yfl} + 2\,\delta F_{yfr} + 2\, m a_x - 2\, F_{xf} - 2\, F_{xr}}{m\tau_{ax}}, \tag{2.47}$$

$$\dot{a}_y = \frac{\delta F_{xf} - m a_y + F_{yfl} + F_{yfr} + F_{yrl} + F_{yrr}}{m\tau_{ay}}; \tag{2.48}$$

and the state space equations are:

$$\dot{u} = -\frac{1}{2}\,\frac{C_D\,A\,\rho\,u^2 - 2\,\dot{\psi} m v + 2\,mg\sin\sigma + 2\,\delta F_{yfr} + 2\,\delta F_{yfl} - 2\,F_{xr} - 2\,F_{xf}}{m}, \tag{2.49}$$

$$\dot{v} = -\frac{\dot{\psi} m u - \delta F_{xf} - F_{yrr} - F_{yrl} - F_{yfr} - F_{yfl}}{m}, \tag{2.50}$$

$$\ddot{\psi} = \frac{1}{2}\,\frac{\delta T F_{yfr} - \delta T F_{yfl} + 2\,\delta a F_{xf} + 2\,a F_{yfr} + 2\,a F_{yfl} - 2\,b F_{yrr} - 2\,b F_{yrl}}{I_z}. \tag{2.51}$$

The Euler equations around x (2.52) and y (2.53) axes and the Newton equation along z axis (2.54) present new terms due to the road slope; the full set of equations, from which it is possible to determine the normal loads, becomes:

$$\dot{\psi}\,\dot{\sigma}(I_z - I_y) - hm a_y + \frac{1}{2}\,T N_{fl} - \frac{1}{2}\,T N_{fr} + 1/2\,T N_{rl} - \frac{1}{2}\,T N_{rr} = 0, \tag{2.52}$$

$$I_y\,\ddot{\sigma} - \frac{1}{2}\,a C_{Lf} A\,\rho\,u^2 + \frac{1}{2}\,b C_{Lr} A\,\rho\,u^2 + mgh\sin\sigma + a_x\,hm + a N_{fl} + a N_{fr} - b N_{rl} - b N_{rr} = 0, \tag{2.53}$$

$$-\dot{\sigma} m u + \frac{1}{2}\,C_{Lf} A\,\rho\,u^2 + \frac{1}{2}\,C_{Lr} A\,\rho\,u^2 + mg\cos\sigma - N_{fl} - N_{fr} - N_{rl} - N_{rr} = 0 \tag{2.54}$$

$$\frac{1}{2}\,(N_{fl} - N_{fr})\,T - hm a_y\,\xi = 0; \tag{2.55}$$

the term $\dot{\psi}\,\dot{\sigma}(I_z - I_y)$ of eq. (2.52) represents the gyroscopic effect of the whole vehicle in x axis, due to a yaw and a pitch rotation of the chassis; $I_y\,\ddot{\sigma}$ (eq. 2.53) is the inertia momentum caused by the variation of the pitch angular velocity while, in eq. (2.54), the term $\dot{\sigma} m u$ represents the z component of the acceleration, because $z = 0\ \forall\ s(t) \in [0, +\infty)$. Solving the system in function of the loads of each wheel the result becomes:

$$N_{fl} = -\frac{1}{2}\frac{mgh\sin\sigma}{w} - \frac{1}{2}\frac{a_x\,hm}{w} + \frac{1}{2}\frac{mgb\cos\sigma}{w} - \frac{1}{2}\frac{\dot{\sigma}bum}{w} + \frac{1}{4}\,C_{Lf}A\,\rho\,u^2 - \frac{1}{2}\frac{I_y\,\ddot{\sigma}}{w} + \frac{hm a_y\,\xi}{T}, \tag{2.56}$$

$$N_{fr} = -\frac{1}{2}\frac{mgh\sin\sigma}{w} - \frac{1}{2}\frac{a_x\,hm}{w} + \frac{1}{2}\frac{mgb\cos\sigma}{w} - \frac{1}{2}\frac{\dot{\sigma}bum}{w} + \frac{1}{4}\,C_{Lf}A\,\rho\,u^2 - \frac{1}{2}\frac{Iy\,\ddot{\sigma}}{w} - \frac{hm a_y\,\xi}{T}, \tag{2.57}$$

$$N_{rl} = \frac{1}{2}\frac{mgh\sin\sigma}{w} + \frac{1}{2}\frac{a_x\,hm}{w} + \frac{1}{2}\frac{mga\cos\sigma}{w} - \frac{1}{2}\frac{\dot{\sigma}aum}{w} + \frac{1}{4}\,C_{Lr}A\,\rho\,u^2 + + \frac{1}{2}\frac{I_y\,\ddot{\sigma}}{w} - \frac{hm a_y\,(\xi-1)}{T} + \frac{\dot{\psi}I_y\,\dot{\sigma}w - \,\dot{\sigma}I_z\,\dot{\psi}w}{T}, \tag{2.58}$$

$$N_{rr} = \frac{1}{2}\frac{mgh\sin\sigma}{w} + \frac{1}{2}\frac{a_x\,hm}{w} + \frac{1}{2}\frac{mga\cos\sigma}{w} - \frac{1}{2}\frac{\dot{\sigma}aum}{w} + \frac{1}{4}\,C_{Lr}A\,\rho\,u^2 + + \frac{1}{2}\frac{I_y\,\ddot{\sigma}}{w} + \frac{hm a_y\,(\xi-1)}{T} + \frac{-\dot{\psi}I_y\,\dot{\sigma}w + \,\dot{\sigma}I_z\,\dot{\psi}w}{T}; \tag{2.59}$$

2.3 Road Reconstruction

Building the road data is fundamental to simulate the vehicle behavior for two reasons: on the one hand it defines the limits of the track in which the car must remain; on the other hand an accurate reconstruction allows the problem to have a faster convergence, while using coarse data implies longer simulations with higher possibilities of capturing non-realistic behaviors.
The "raw data" of the road is obtained thanks to the creation of two text files, which contain respectively the coordinates of the right and left borders in terms of latitude and longitude; this two-dimensional data is taken from Google™ satellite maps[1], and the road profiles are captured with a series of points by the user. A further text file for road elevation is then created from a database[2] in which is mapped the elevation as a function of latitude and longitude; in fact, setting the previously obtained coordinates as an input, the database generates the correspondent altitude data.
The files obtained are then used as an input for a MATLAB script in which are calculated the cartesian coordinates of the $X_cY_cZ_c$ earth-centered Cartesian system (ECEF) from the $\Phi\Lambda h$ coordinate system:

$$X_c = (N(\Phi) + h)\,\cos\Phi\cos\Lambda, \tag{2.60}$$

$$Y_c = (N(\Phi) + h)\,\cos\Phi\sin\Lambda, \tag{2.61}$$

$$Z_c = [N(\Phi)(1-e^2) + h]\,\sin\Phi; \tag{2.62}$$

[1]The maps are available at the following link `http://www.google.com/earth/index.html`.
[2]The database is available at the following link `http://www.gpsvisualizer.com/elevation`.

e represents the earth eccentricity, a the semi-major axis, Φ is the latitude, Λ the longitude, h the elevation and $N(\Phi)$ is the distance from the surface to the Z_c axis along the ellipsoid normal,

$$N(\Phi) = \frac{a}{\sqrt{1 - e^2 \sin^2 \Phi}}. \tag{2.63}$$

It is possible to group the boundary measurements in a set of the M right hand boundary points $\mathcal{B}_r$ and a set of the M left hand side points $\mathcal{B}_l$; these groups contain the measured set of vectors $\mathbf{b}_{r,i} = [X_c, Y_c, Z_c]_{r,i}$ and $\mathbf{b}_{l,i} = [X_c, Y_c, Z_c]_{l,i}$ respectively, for $i = 1, \ldots, M$; the group of track centre line points $\mathcal{C}$ can be deduced with the relation $\mathbf{c}_i = (\mathbf{b}_{l,i} + \mathbf{b}_{r,i})/2$. At this point the satellite data captured is ready for the last step of road reconstruction that consists in a *track smoothing optimal control problem* [9]. The *state vector*, contains the full set of state variables; one of the possible choices is:

$$\mathbf{x} = [x,\, y,\, z,\, \theta,\, \sigma,\, \beta,\, \dot{\theta},\, \dot{\sigma},\, \dot{\beta},\, n_l,\, n_r]^T; \tag{2.64}$$

note that the coordinates of the road centre vector $\mathbf{c} = [x, y, z]$ are now defined with reference to the start line of the track for simplicity. As for the control vector, a possible definition is consequently:

$$\mathbf{u} = [\ddot{\theta},\, \ddot{\sigma},\, \ddot{\beta},\, \dot{n}_l,\, \dot{n}_r]^T. \tag{2.65}$$

The road is defined by a series of strips, each one characterized by three eulerian angles: s is the curvilinear abscissa, θ represents the road *heading*, or rather the direction of traveling, σ represents the *slope* and β describes the *banking* or, in other words, the leaning of the road; n_l and n_r are the distances between the road left and right borders and the centre line (typically $n_l = n_r = n_w$). Each *ribbon* of the road can be parametrically defined using a vector $\mathbf{r}(s, n) = \mathbf{c}(s) + \mathbf{n}(s)$ where $\mathbf{c}(s)$ represent the coordinate of the centre of the ribbon and $\mathbf{n}(s)$ is the vector that links the centre to each point of the ribbon. Following these considerations, the state equations can be obtained from the following expressions:

$$\theta(s) = \int_{s_0}^{s} \dot{\theta}(s)\, ds, \tag{2.66}$$

$$\sigma(s) = \int_{s_0}^{s} \dot{\sigma}(s)\, ds, \tag{2.67}$$

$$\beta(s) = \int_{s_0}^{s} \dot{\beta}(s)\, ds, \tag{2.68}$$

$$\mathbf{r}(s, n) = \int_{s_0}^{s} \dot{\mathbf{c}}(s)\, ds + \mathbf{n}(s). \tag{2.69}$$

$$\tag{2.70}$$

The purpose of the problem is to minimize the Euclidean distances between the *ribbon model* of the road and the data set deduced from the measured points $\overline{\mathcal{B}}_l$, $\overline{\mathcal{B}}_r$, $\overline{\mathcal{C}}$: these curves are obtained interpolating the measured data point for left

border, right border and centre line respectively.
The integral cost function for the optimal control problem can be expressed using three terms:

$$l(s, \mathbf{x}, \mathbf{u}) = e(s, \mathbf{x}, \mathbf{u}) + r_c(s, \mathbf{u}) + r_w(s, \mathbf{u}); \tag{2.71}$$

the term $e(s, \mathbf{x}, \mathbf{u})$ represents the *tracking error*, or rather the error between the curves defined by the points $\mathcal{C}$ and $\overline{\mathcal{C}}$, $\mathcal{B}_l$ and $\overline{\mathcal{B}}_l$, $\mathcal{B}_r$ and $\overline{\mathcal{B}}_r$; each component of error is multiplied by a *weighting function* w that determines the importance of each term and consequently the accuracy of tracking:

$$e(s, \mathbf{x}, \mathbf{u}) = w_c \|\mathbf{c} - \overline{\mathbf{c}}\| + w_l \|\mathbf{b}_l - \overline{\mathbf{b}}_l\| + w_r \|\mathbf{b}_r - \overline{\mathbf{b}}_r\|. \tag{2.72}$$

The second term $r_c(s, \mathbf{u})$ is connected to the *curvature rate* and reduces the high frequency content of the road curvature; similarly to the previous expression each component is weighted by the w functions that determine the smoothness of the road:

$$r_c(s, \mathbf{u}) = w_\theta \ddot{\theta}^2(s) + w_\mu \ddot{\mu}^2(s) + w_\phi \ddot{\phi}^2(s). \tag{2.73}$$

The *width rate* term $r_w(s, \mathbf{u})$ allows a limitation in the high frequency noise of the track boundaries: higher values of w permit a smoother variation for the road width;

$$r_w(s, \mathbf{u}) = w_{n_l} \dot{n}_l^2(s) + w_{n_r} \dot{n}_r^2(s). \tag{2.74}$$

2.4 Slip-Slip Model

The main limits of the *basic* model described in section 2.2, can be highlighted considering that the longitudinal slip is neglected and only a simplified formulation with partial force combination is provided for the tires. The adherence ellipses in reality depend on the wheel loads applied, and their from is not properly elliptic (fig. 2.8).
By contrast, in the *slip-slip* model is taken into account a more complete formulation for the tyre dynamics, adopting more elaborated equations for the tyre forces, both in lateral and longitudinal direction, and providing a combination for the forces themselves. In this case the tyre forces are related to a simplified formulation of the Pacejka *Magic Formula* [8] and depend on lateral and longitudinal slip quantities, which must be obtained for each wheel.

2.4.1 Kinematics

Starting from the expressions of the *trim angles* β_w from eq. (2.3), (2.4), (2.5) and (2.6), it is possible to deduce the *lateral slip angles* λ for each wheel:

$$\lambda_{fl} = \delta - \frac{\dot{\psi}a + v}{\frac{1}{2}\dot{\psi}T + u}, \qquad \lambda_{fr} = \delta - \frac{\dot{\psi}a + v}{-\frac{1}{2}\dot{\psi}T + u}, \tag{2.75}$$

$$\lambda_{rl} = -\frac{-\dot{\psi}b + v}{\frac{1}{2}\dot{\psi}T + u}, \qquad \lambda_{rr} = -\frac{-\dot{\psi}b + v}{-\frac{1}{2}\dot{\psi}T + u}. \tag{2.76}$$

Also the *longitudinal slips* κ are fundamental for the determination of the tyre forces; these quantities express the non ideal slip properties of the wheels in longitudinal direction and are defined as follows:

$$\kappa_{fl} = \frac{\omega_{fl} R_w - u_{fl}}{u_{fl}}, \quad \kappa_{fr} = \frac{\omega_{fr} R_w - u_{fr}}{u_{fr}}, \tag{2.77}$$

$$\kappa_{rl} = \frac{\omega_{rl} R_w - u_{rl}}{u_{rl}}, \quad \kappa_{rr} = \frac{\omega_{rr} R_w - u_{rr}}{u_{rr}}. \tag{2.78}$$

During traction the tangential velocity of the wheel ωR_w is greater than the longitudinal velocity $u_w = \{u_{fl}, u_{fr}, u_{rl}, u_{rr}\}$ and then κ is positive; on the contrary, during braking, u_w is greater than the tangential velocity and κ has a negative value. Substituting now the expressions for u_w in the definitions of κ, the explicit expression are obtained, where R_w is the wheel radius and $\omega = \dot{\theta}$.

$$\kappa_{fl} = \frac{\dot{\theta}_{fl} R_w - \frac{1}{2}\dot{\psi}T - u}{\frac{1}{2}\dot{\psi}T + u}, \quad \kappa_{fr} = \frac{\dot{\theta}_{fr} R_w + \frac{1}{2}\dot{\psi}T - u}{-\frac{1}{2}\dot{\psi}T + u}, \tag{2.79}$$

$$\kappa_{rl} = \frac{\dot{\theta}_{rl} R_w - \frac{1}{2}\dot{\psi}T - u}{\frac{1}{2}\dot{\psi}T + u}, \quad \kappa_{rr} = \frac{\dot{\theta}_{rr} R_w + \frac{1}{2}\dot{\psi}T - u}{-\frac{1}{2}\dot{\psi}T + u}. \tag{2.80}$$

The formulation used for the slip quantities refers to the so called *theoretical slips*; a different definition of the slip parameters is also useful to describe the Pacejka *Magic Formula* [8] for F_x and F_y: the *practical slips* σ_x and σ_y; these quantities must be defined for each wheel, although only a general formulation is reported.

$$\sigma_x = \frac{\kappa}{\sqrt{1+\kappa^2}}, \tag{2.81}$$

$$\sigma_y = \frac{\tan(\lambda)}{\sqrt{1+\kappa^2}}, \tag{2.82}$$

$$\sigma_{tot} = \sqrt{\sigma_x^2 + \sigma_y^2}. \tag{2.83}$$

If the model includes the effect of the *camber angle* of the wheel γ, it is necessary calculate an *equivalent slip angle* λ^* [3].

[3] In [8] can be found that $\lambda^* = \lambda + C_\gamma \gamma / C_\lambda$, with $C_\lambda = K_y N$ and C_γ *camber stiffness* of the tyre. In the simulations considered in this work the camber is drawn to zero.

2.4.2 Dynamics

In this model it is fundamental to consider different forces for each wheel; in fact the tyre forces depend on the normal loads which, because of the lateral and longitudinal load transfer, are different for each wheel; it can be noticed that this observation leads to a different formulation respect the previous model: in this case the longitudinal forces F_x do not represent the input for the dynamic system any more and, by contrast, are function of the longitudinal slips.
Applying the complete Pacejka *Magic Formula* [8], the longitudinal and lateral forces become:

$$F_x = N \frac{\sigma_x}{\sigma_{tot}} D_x \sin\{C_x \arctan\left[B_x \sigma_{tot} - E_x \left(B_x \sigma_{tot} - \arctan(B_x \sigma_{tot})\right)\right]\}, \quad (2.84)$$

$$F_y = N \frac{\sigma_y}{\sigma_{tot}} D_y \sin\{C_y \arctan[B_y \sigma_{tot} - E_y \left(B_y \sigma_{tot} - \arctan(B_y \sigma_{tot})\right)]\}; \quad (2.85)$$

each force must be specified for each wheel using the appropriate $\sigma_x, \sigma_y, \sigma_{tot}, N$ and the coefficients B, C, D, E: all these quantities can assume different values for each wheel.
The parameters B, C, D, E are defined considering a reference value for normal loads N_0: a coefficient df_z is then employed to linearly scale the peak friction coefficient D for different values of normal loads:

$$df_z = \frac{N - N_0}{N_0}. \quad (2.86)$$

Considering the expressions of F_x/N and F_y/N, that represent the tyre forces (longitudinal or lateral) normalized by the load, it can be noticed that D defines the peak, C is the asymptotic value assumed for infinite slip, B depends on the slope at the origin and E represents form and position of the peak. Moreover can be demonstrated that the product $K = BCD$ is the slope of the normalized force at the origin. For the longitudinal forces:

$$K_x = B_x C_x D_x = pK_{x1} \exp(pK_{x3}\, df_z), \quad (2.87)$$

while the force coefficients are:

$$E_x = pE_{x1}, \quad (2.88)$$

$$D_x = (pD_{x1} + pD_{x2}\, df_z)\, \lambda_{\mu,x}, \quad (2.89)$$

$$C_x = pC_{x1}, \quad (2.90)$$

$$B_x = \frac{K_x}{C_x D_x N}. \quad (2.91)$$

Similarly for the lateral parameters:

$$K_y = pK_{y1} N_0 \sin\left(2 \arctan \frac{N}{pK_{y2} N_0}\right), \quad (2.92)$$

and for the force coefficients:

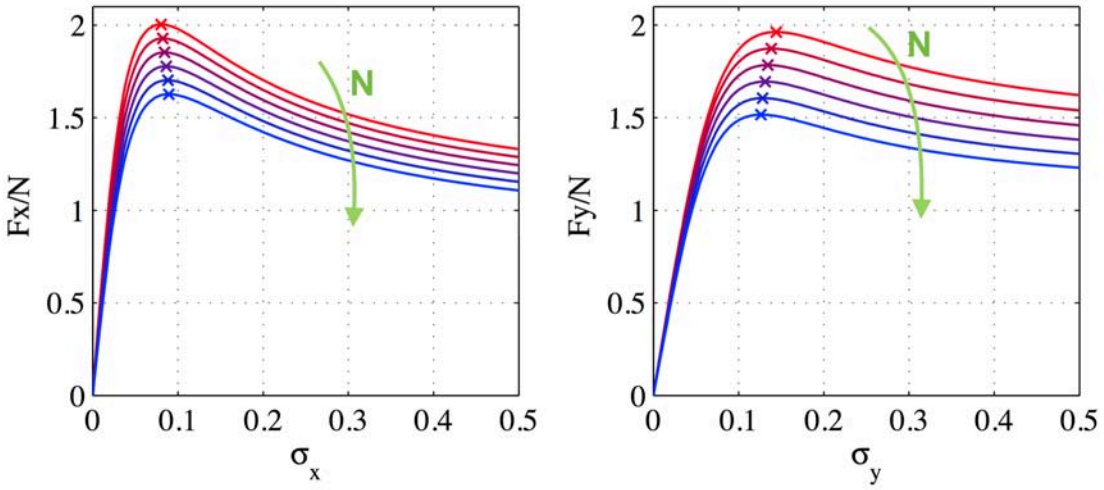

Figure 2.7: Normalized longitudinal (left) and lateral (right) tyre forces, for normal loads from 500 N (red, top) to 5500 N (blue, bottom) in steps of 1000 N.

$$E_y = pE_{y1}, \tag{2.93}$$
$$D_y = (pD_{y1} + pD_{y2}\, df_z)\, \lambda_{\mu,y}, \tag{2.94}$$
$$C_y = pC_{y1}, \tag{2.95}$$
$$B_y = \frac{K_y}{C_y\, D_y\, N}; \tag{2.96}$$

where $\lambda_{\mu,x}$ and $\lambda_{\mu,y}$ are the scaling factors that reduce the friction in different conditions of tires and road. The parameters pD, pC, pE, pK derive from empirical tests on the wheels. In fig. (2.7) is represented a typical form of the tyre functions defined.

It is important to underline that only simplified formulas for the tyre coefficient are used [15], taking into consideration the main terms, in order to allow an easier convergence for the optimal control problem; the full expressions of B, C, D, E can be found in [8].

In fig. 2.8 is reported the g-g diagram obtained with the tyre coefficients implemented in the *slip-slip* model; it can be observed the typical "curl": in fact decreasing the lateral adherence coefficient F_y/N, the longitudinal friction coefficient F_x/N increases until, under certain values of F_y/N, F_x/N is definitely reduced.

Taking advantage of the considerations on the necessity of defining different forces for each wheel, the following formulation becomes clear:

$$\mathbf{F}_{fl} = [F_{xfl},\, F_{yfl},\, N_{fl}]\,, \qquad \mathbf{F}_{fr} = [F_{xfr},\, F_{yfr},\, N_{fr}]\,; \tag{2.97}$$
$$\mathbf{F}_{rl} = [F_{xrl},\, F_{yrl},\, N_{rl}]\,, \qquad \mathbf{F}_{rr} = [F_{xrr},\, F_{yrr},\, N_{rr}]\,. \tag{2.98}$$

The Newton-Euler equations for the xy plane do not present significant variations, except the fact that the longitudinal forces are different in each wheel:

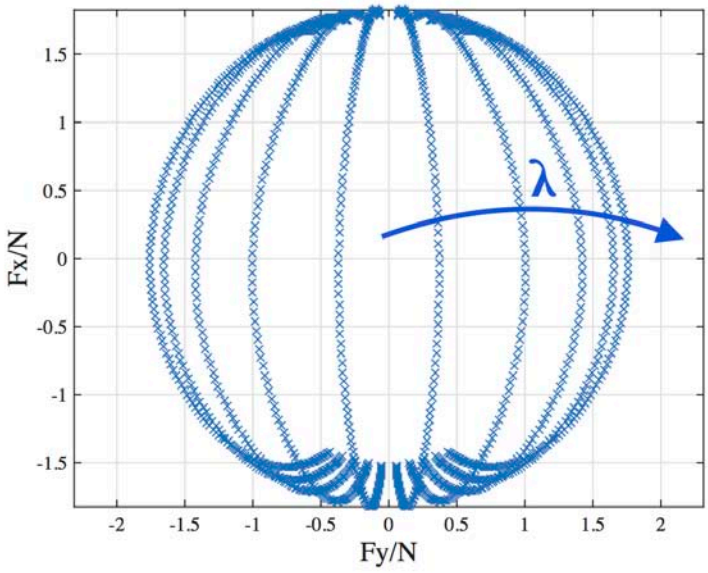

Figure 2.8: Adherence diagram obtained with the Pacejka parameters of the tyre model adopted for the simulations, for different values of λ.

$$\left(-\dot{\psi}\, v + \dot{u}\right) m + \frac{1}{2}\, C_D A\, \rho\, u^2 - (F_{xfl} + F_{xfr} + F_{xrl} + F_{xrr}) + (F_{yfl} + F_{yfr})\ \delta = 0, \tag{2.99}$$

$$m(\dot{\psi}\, u + \dot{v}) - (F_{yfl} + F_{yfr} + F_{yrl} + F_{yrr}) - (F_{xfl} + F_{xfr})\ \delta = 0, \tag{2.100}$$

$$I_z\, \ddot{\psi} + \frac{1}{2}\, \delta T\, (F_{yfl} - F_{yfr}) - \delta\, a\, (F_{xfl} + F_{xfr}) + \frac{1}{2}\, T\, (-F_{xfl} + F_{xfr} - F_{xrl} + F_{xrr}) - \\ - a\, (F_{yfl} + F_{yfr}) + b\, (F_{yrl} + F_{yrr}) = 0. \tag{2.101}$$

Consequently the *state space* equations become:

$$\dot{u} = \dot{\psi}\, v - \frac{1}{2}\, \frac{C_D A\, \rho\, u^2}{m} + \frac{(F_{xfl} + F_{xfr} + F_{xrl} + F_{xrr})}{m} - \frac{(F_{yfl} + F_{yfr})\ \delta}{m}, \tag{2.102}$$

$$\dot{v} = -\dot{\psi}\, u + \frac{(F_{yfl} + F_{yfr} + F_{yrl} + F_{yrr}) + (F_{xfl} + F_{xfr})\ \delta}{m}, \tag{2.103}$$

$$\ddot{\psi} = -\frac{1}{2}\frac{\delta\, T\, (F_{yfl} - F_{yfr}) - 2\, \delta\, a\, (F_{xfl} + F_{xfr}) + T\, (-F_{xfl} + F_{xfr} - F_{xrl} + F_{xrr})}{I_z} + \\ + \frac{a\, (F_{yfl} + F_{yfr}) + b\, (F_{yrl} + F_{yrr})}{I_z}. \tag{2.104}$$

Chapter 3

Minimum Time Simulation

3.1 Optimal Control Problem

An optimal control problem, as underlined in sec. 1.1, is defined by a set of *state space variables* $\mathbf{x}$ and a set of *control variables* $\mathbf{u}$: the choice of these variables determines the model equations that must be used and the efficiency of the simulation in terms of time for convergence and quality of the results.
Moreover the problem is defined by a *cost function* to minimize, composed by a term that depends on the initial and final value of the parameters, and an integral term, as previously reported with eq. (1.1). In this case the *target function* depends only on the second term, known as *Lagrange* integral function:

$$\mathcal{F}(\mathbf{u}) = \int_{t_i}^{t_f} \mathcal{L}(\mathbf{x}(t), \mathbf{u}(t))dt = \int_{s_i}^{s_f} \frac{1}{\dot{s}}\, ds; \tag{3.1}$$

in other words the objective of the optimal control problem is to minimize the lap time in a properly defined track.
In order to privilege the model behaviors free from high dynamics effects (i.e. vibrations) of the control quantities, it is possible to add at the integrand of the *objective function* a series of terms, or *penalties*, that represent the squared control variables, multiplied by a coefficient u_ε that weights the effect of the *penalty* terms.

$$\mathcal{F}(\mathbf{u}) = \int_{s_i}^{s_f} \frac{1}{\dot{s}} \left(1 + u_\varepsilon \sum\nolimits_i \mathbf{u}_i^2\right) ds; \tag{3.2}$$

$\mathbf{u}_i$ represents the generic control, for $i = 1, \ldots, N_u$, and N_u number of controls that have to be penalized.

In the *basic model* a possible set of state variables and controls is:

$$\mathbf{x} = [n,\, \chi,\, u,\, v,\, \Omega,\, a_x,\, a_y]^T, \tag{3.3}$$

$$\mathbf{u} = [F_x/mg,\, \delta/k_\delta]^T; \tag{3.4}$$

all the state variables $\mathbf{x}$ come from the integration of the state equations $\dot{\mathbf{x}}$, or rather eq. (2.42), (2.43), (2.102), (2.103), (2.104), (2.35) and (2.37). The control variables are the total longitudinal tyre force F_x, normalized by the weight force

of the vehicle, and the steering angle of the front wheels δ, divided by a constant $k_\delta = 15\pi/180$ rad; the normalization of the control parameters is fundamental to allow an easier convergence of the simulation.
It must be underlined that, in the minimum lap time problems, the integration is not employed in the domain of time; in fact the state space equations are written in term of the derivative of the curvilinear abscissa $s(t)$. The reason of this choice consists in the fact that the road parameters (e.g. curvature, width, slope) are known in function of $s(t)$; moreover all the resulting quantities of the simulation, such as the forces and the velocities, are easier to be interpreted considering their variation with the position of the car in the track (i.e. the curvilinear abscissa). To traduce the whole set of differential equations $\dot{\mathbf{x}}$ in term of derivative of $s(t)$ it is possible to observe that in general:

$$\frac{d\,\mathbf{x}}{ds} = \frac{d\,\mathbf{x}}{dt}\,\frac{dt}{ds} = \frac{\dot{\mathbf{x}}}{\dot{s}}\,; \tag{3.5}$$

the derivative of the curvilinear abscissa $\dot{s}$ is calculated in eq. (2.41).
A different strategy can be considered in order to limit the vibrations of the controls; this purpose is rached employing the derivatives of F_x and δ as controls and including the total longitudinal force and the steering angle as state variables. The two further state equations are:

$$\frac{d}{ds}\left(\frac{F_x}{mg}\right) = \frac{1}{\dot{s}}\left(k_{dF}\,\frac{\dot{F}_x}{mg}\right), \qquad \frac{d}{ds}\left(\frac{\delta}{k_\delta}\right) = \frac{1}{\dot{s}}\left(k_{d\delta}\,\frac{\dot{\delta}}{k_\delta}\right); \tag{3.6}$$

the constants k_{dF} and $k_{d\delta}$ are required for the usage of normalized controls, with values near unity, in order to permit less numeric difficulties for the solver.

$$\mathbf{x} = \left[n,\, \chi,\, u,\, v,\, \Omega,\, a_x,\, a_y,\, F_x/mg,\, \delta/k_\delta\right]^T, \tag{3.7}$$

$$\mathbf{u} = \left[\dot{F}_x/mg,\, \dot{\delta}/k_\delta\right]^T. \tag{3.8}$$

This choice is fundamental to reach a solution for the problem: in fact the first control method, proposed at (3.4), generates a significantly vibrating signal for controls, that makes the solution really tough to be achieved; controlling the systems with the derivatives generates a "filtering" action for the controls, that result free from high-frequency components. In figure 3.1 is remarked this concept considering that the control strategy without the derivatives of the variables of interest (on top) has not been capable of converging to a solution with the tolerance requested.

The adoption of the normal loads as controls, represents a significant advantage in terms of time, in particular when coupled with *ADiGator* for automatic differentiation.

$$\mathbf{x} = \left[n,\, \chi,\, u,\, v,\, \Omega,\, a_x,\, a_y,\, F_x/mg,\, \delta/k_\delta\right]^T, \tag{3.9}$$

$$\mathbf{u} = \left[\dot{F}_x/k_{dF},\, \dot{\delta}/k_{d\delta},\, N_{fl},\, N_{fr},\, N_{rl},\, N_{rr}\right]^T; \tag{3.10}$$

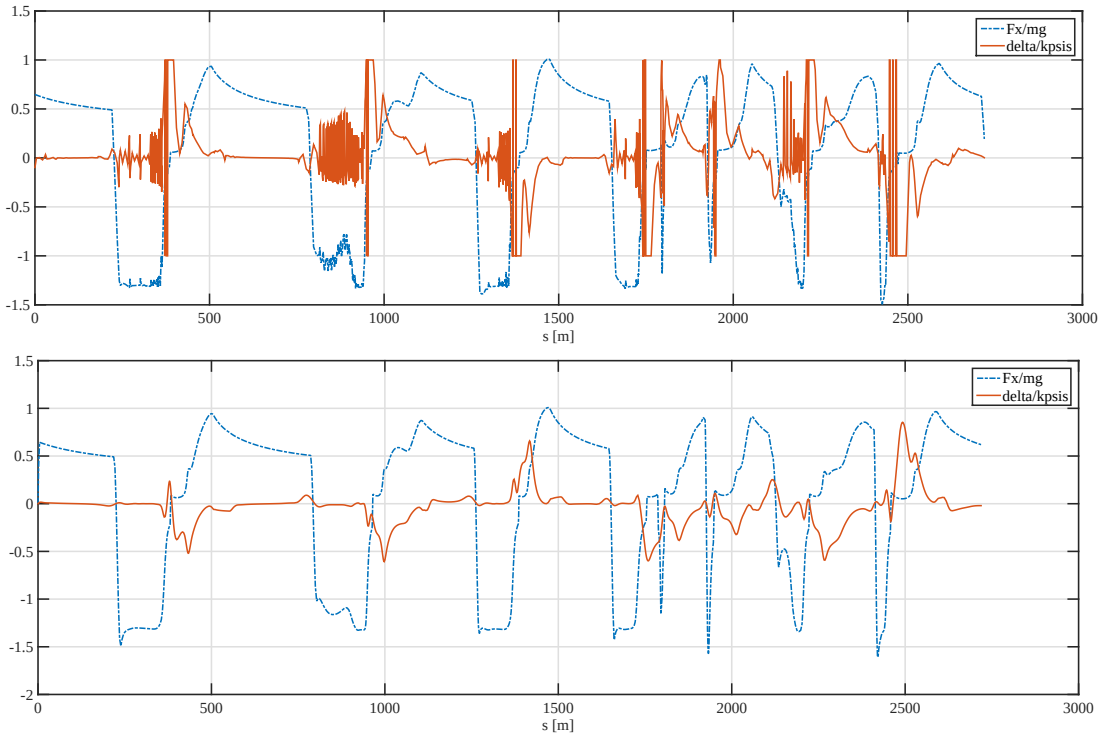

Figure 3.1: Comparison between the control method without using the derivatives of the input functions (top) and derivative control (bottom).

This control strategy requests a new series of path constraints for the definition of the normal loads; including the longitudinal and lateral behavior, the set of equations, that must be satisfied in each instant of simulation, can be obtained from the Euler equation around y axis (2.24), the Newton equation along z direction (2.25) and the relations between the lateral load transfer and the roll stiffness ratio (2.22).

$$\frac{1}{2}\left(N_{rl}-N_{rr}\right)T - m a_y\, h\,(1-\xi) = 0, \tag{3.11}$$

$$\left(\frac{1}{2}\,C_{Lf}\,A\,\rho\,u^2 - N_{fl} - N_{fr}\right)a + \left(-\frac{1}{2}\,C_{Lr}\,A\,\rho\,u^2 + N_{rl} + N_{rr}\right)b - hma_x = 0, \tag{3.12}$$

$$-mg - \frac{1}{2}\,C_{Lf}\,A\,\rho\,u^2 - \frac{1}{2}\,C_{Lr}\,A\,\rho\,u^2 + N_{fl} + N_{fr} + N_{rl} + N_{rr} = 0, \tag{3.13}$$

$$\frac{1}{2}\left(N_{fl}-N_{fr}\right)T - hma_y\,\xi = 0. \tag{3.14}$$

The comparison between the different control strategies presented for the *basic model* is resumed in table 3.1; it is important to notice that the *automatic differentiation method* allows a 46% of time advantage respect to the finite differentiating

Solver Type Adria	Lap Time [s]	CPU Time [s]	Mesh iter.	Time adv. [%]
sparseCD / N $\notin$ u	75.627	406	13	-
sparseCD / N $\in$ u	75.627	919	11	+126
***ADiGator* / N $\notin$ u**	75.627	221	12	−46
***ADiGator* / N $\in$ u**	75.627	203	10	−50

Table 3.1: Comparison between different solving strategies (with lift forces).

method (*sparseCD*) without using normal loads as controls. Although the controlling method proposed in (3.10) determines a significant drawback using the finite differentiation method (*sparseCD*), the combination of normal loads control and *ADiGator* permits the 50% of simulation time advantage: this choice will be used for all the models taken into consideration. However, it should be noticed that the greatest part of computational time advantage is due to *ADiGator*, while the advantage related to the normal load control, in this case, is only 4% with respect to the case in which N are not included in the controls.
Different modelling strategies imply different choices for the state variables and the controls; in fact with the *slip-slip* model a new set of equations become part of the dynamics of the system, including the variables of the longitudinal slips κ. Such as the previous model, also in this case the controls are defined with the derivatives of the variables.

$$\mathbf{x} = [n,\, \chi,\, u,\, v,\, \Omega,\, a_x,\, a_y,\, \kappa_{fl},\, \kappa_{fr},\, \kappa_{rl},\, \kappa_{rr},\, \delta/k_\delta]^T, \tag{3.15}$$

$$\mathbf{u} = \left[\dot{\kappa}_{fl},\, \dot{\kappa}_{fr},\, \dot{\kappa}_{rl},\, \dot{\kappa}_{rr},\, \dot{\delta}/k_{d\delta},\, N_{fl},\, N_{fr},\, N_{rl},\, N_{rr}\right]^T; \tag{3.16}$$

Although the choice of calculating the derivatives with *ADiGator* [1] allows a consistent advantage in terms of time of simulation, a few drawbacks have to be highlighted; in fact this automatic differentiation algorithm presents some issues concerning the code robustness: in other words *ADiGator* does not represent a flexible solution when using *if clauses*, *for cycles* or *user-defined functions* in the *continuous function* of GPOPS. In particular no abuse of *if clauses* is allowed, or rather no concatenated multiple conditional commands are permitted; moreover, during the definition of a sigle variable or constraint, an error occurs when multiple *user-defined functions* are employed.

3.2 Model Validation - Adria

[1] for these simulations was adopted *ADiGator* in version 1.1; version 1.2 has not been used because of some code issues.

Lap Time [s]	**CPU Time [s]**	**Penalties [s]**	**Real Time [s]**
76.398	191	0.075	76.630

Table 3.2: Simulation on *Adria* circuit.

The vehicle model has been validated taking into consideration the *Adria International Raceway*, for which has been possible a comparison between the model and the real car lap time: Adria in fact is the circuit used for testing the new vehicles. For this purpose has been adopted the *basic car model* that will be used as reference for the other models employed; in other words this model is set-up to generate a series of data that is properly comparable to the real vehicle behavior and that is useful for the comparison with different modelling strategies. This analysis is caused by the fact that no tyre or aerodynamics data is available for the GT3 vehicle; therefore the data has necessarily been fitted in order to obtain a behavior similar to the reality. In particular the "set-up" of the vehicle is made choosing a proper value for the D_y coefficient of the tyre formula, that represents the peak value of the curve; the aerodynamics is considered only with an estimated value for the drag area $C_D A = 0.65\text{m}^2$, while the lift forces are not employed.
The main parameters estimated for the simulation are summed up in table 3.3.

Model Validation	**Description**	**Value**
$\mathbf{C_L A}\,[\mathbf{m}^2]$	total lift area coefficient	0
$\mathbf{C_D A}\,[\mathbf{m}^2]$	drag area coefficient	0.65
$\mathbf{D_{yf}}\,[-]$	peak for the front tyre normalized lateral force	1.55
$\mathbf{D_{yr}}\,[-]$	peak for the rear tyre normalized lateral force	1.55
$\mathbf{D_{xf}}\,[-]$	peak for the front tyre normalized longitudinal force	1.75
$\mathbf{D_{xr}}\,[-]$	peak for the rear tyre normalized longitudinal force	1.75
$\mathbf{K_{yf}}\,[-]$	slope of the front tyre normalized lateral force	30
$\mathbf{K_{yr}}\,[-]$	slope of the rear tyre normalized lateral force	30

Table 3.3: Simulation parameters used for model validation.

The results obtained for the *Adria International Raceway* (table 3.2) are consistently similar to the real ones, with a simulated lap time of 76.398 s in comparison with a real lap time of 76.630 s. Also the trajectory (fig. 3.2) maintains the same form for the simulated data and the real GPS data: the most significant differences can be mostly connected to the GPS error, because the signal is obtained only from a sensor positioned on the vehicle, without the triangulation possible with a fixed track GPS station [2].

The velocity profiles, despite the fact that the form of the simulated values is very close to the real ones, have a significant difference in terms of maximum speed. If the form depends on the longitudinal acceleration, that is a function of the longitudinal tyre capabilities, the pure top speed depends on two main factors:

[2]This method is used mainly in Formula 1, for a more precise GPS tracking.

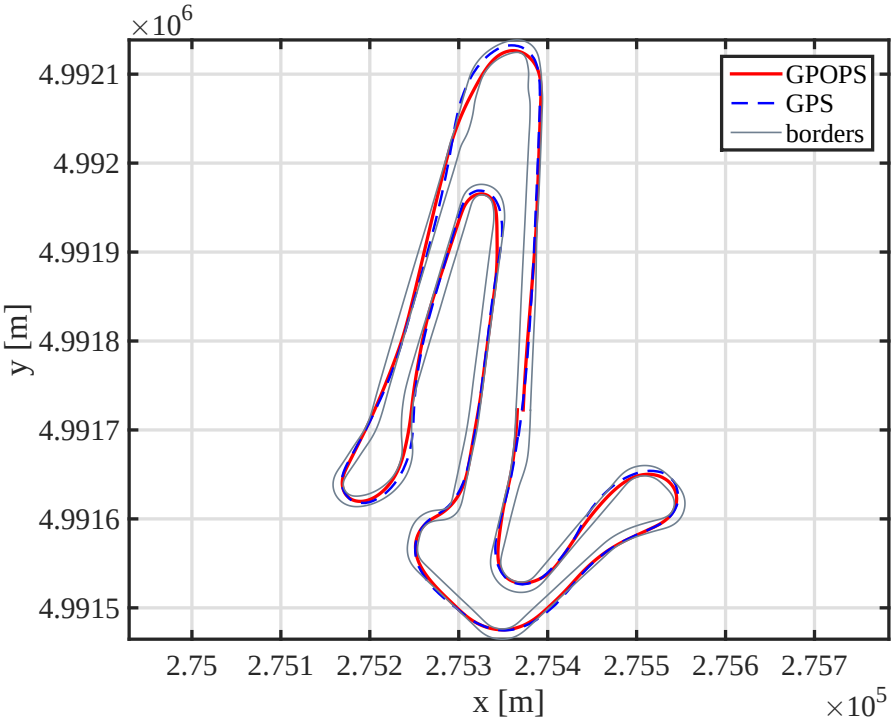

Figure 3.2: Comparison between the simulated trajectory (continuous line) and the real GPS data (dashed line).

the drag data estimated, that probably does not represent perfectly the reality, and the model itself that does not employ the longitudinal slip and the vertical load dependence of the adherence ellipses; consequently the simulated car takes an advantage during acceleration and braking conditions because the friction coefficients are not reduced increasing the normal loads (see fig. 2.7) and no longitudinal slip occurs neither at low nor at high speeds. It is important to underline that these considerations do not imply that the *basic model* with constant adherence ellipses offers a lower lap time than the *slip-slip* model: in fact the optimal control allows to reach the best performance for each model, exploiting the implemented variables coherently to the constraints. The control takes advantage of the lack of longitudinal slip to reach higher top speeds in the *basic model*, while, employing the formulation of κ, the system might be capable of improving this performance, leading the vehicle to its ultimate limit.
The combination of these issues permits a resulting speed profile that has similar slope and form to the real one, but with higher top speed in the straights (fig. 3.3). It should be considered that the initial speed is imposed by the boundary conditions at 182 km/h: this value represents approximately the speed reached at the end of the lap. Furthermore low initial velocities (i.e. $u \leq 40 \div 50$ km/h) determine significant difficulties for the convergence of the optimal control problem.

From the simulation results can be plotted the adherence ellipses diagrams (fig. 3.4), in which it is possible to observe that the front wheels (on the right) can develop negative F_x only, or rather are capable of braking and not to impress

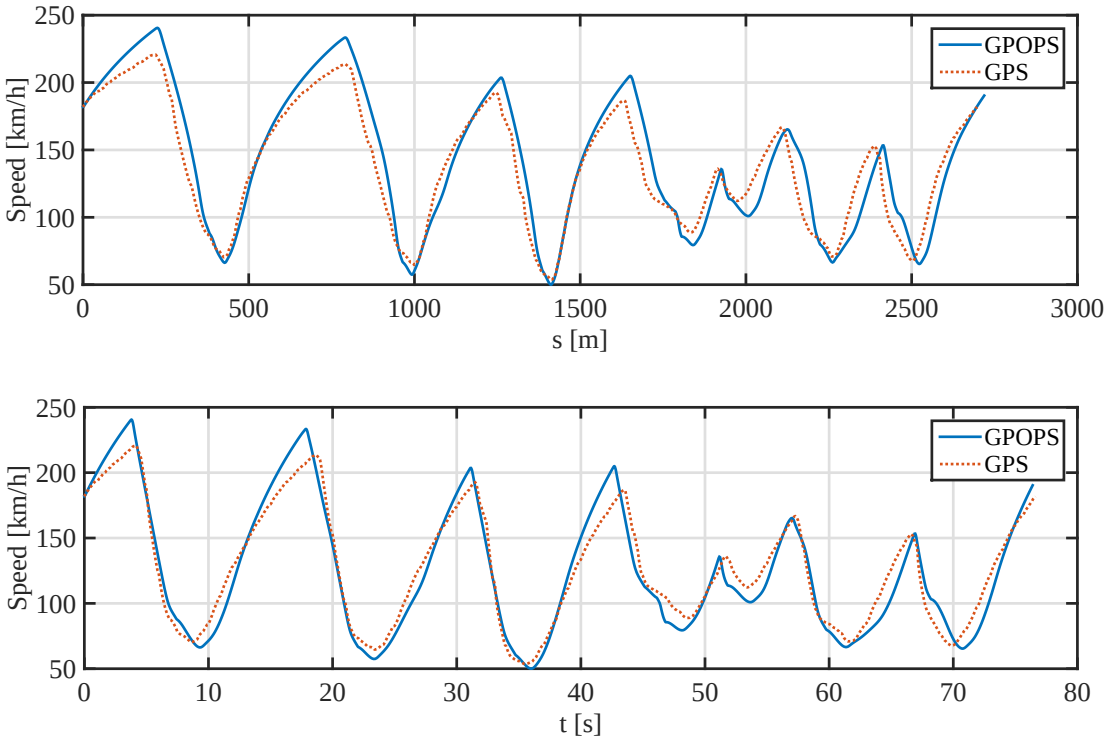

Figure 3.3: Comparison between the simulated speed (continuous line) and the real GPS data (dot-dashed line).

traction forces because the model is representative of a real wheel drive (RWD) car. Furthermore it can be noticed that the vehicle takes advantage of all the limit curves to achieve the best time performance, in accordance to the vehicle dynamics principles.

The model is controlled trough the derivatives of the total longitudinal force applied to the tires F_x and the steering angle δ; each quantity is normalized in order to obtain controls limited in the interval $[-1, +1]$. As demonstrated in fig. 3.5, the vibration of the controls does not affect F_x and δ.

In fig. 3.6 are reported the variation of the normal loads during the track (on top) and the longitudinal forces for the front and rear axle F_{xf} and F_{yf}. These two dynamic quantities are plotted in the same figure in order to highlight the effect of longitudinal and lateral load transfer during acceleration, braking and turning; in fact when the vehicle accelerates at the start of the track the front loads (dot-dash lines) decrease while the rear values (continuous lines) are increasing; both front and rear loads at the initial time (or at $s(t_0) = 0$) are defined at their static values. During the deceleration phase the effect is opposite with increasing front loads and decreasing rear loads; differently in cornering condition the effect of the lateral load transfer brings the load to the external wheels while the internal wheels are progressively unloaded. With this vehicle in particular the condition of completely unloaded wheels never occurs because of the limited rolling behavior and the high roll stiffness.
Regarding the longitudinal forces it is important to underline that the rear wheels

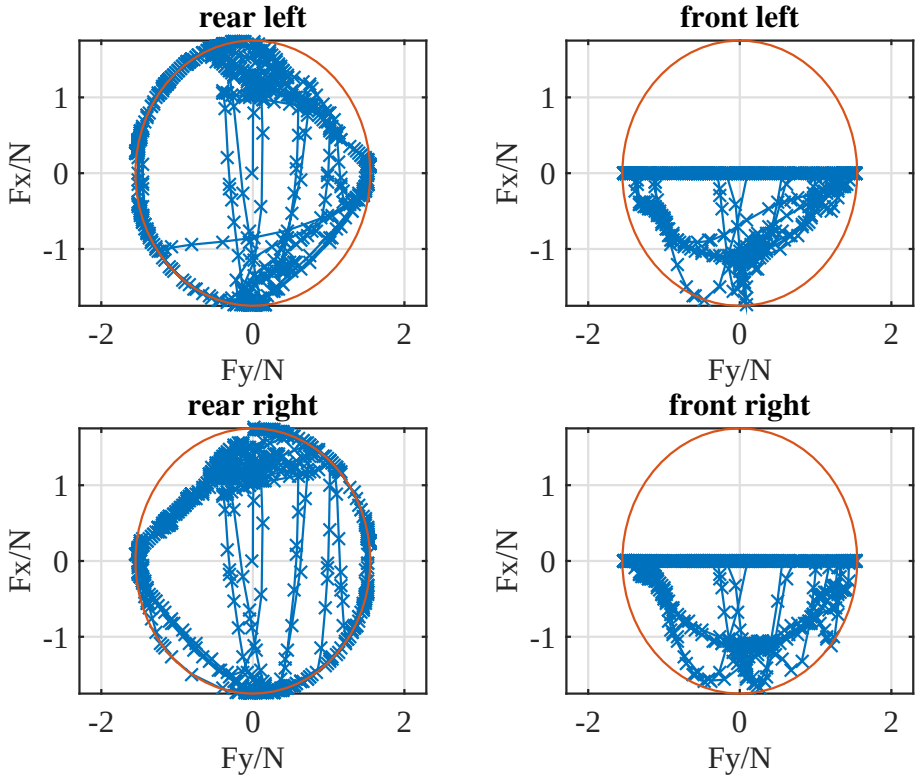

Figure 3.4: Adherence ellipses for each wheel (continuous lines) overlaid by the result data points (F_y/N, F_x/N) with cross mark.

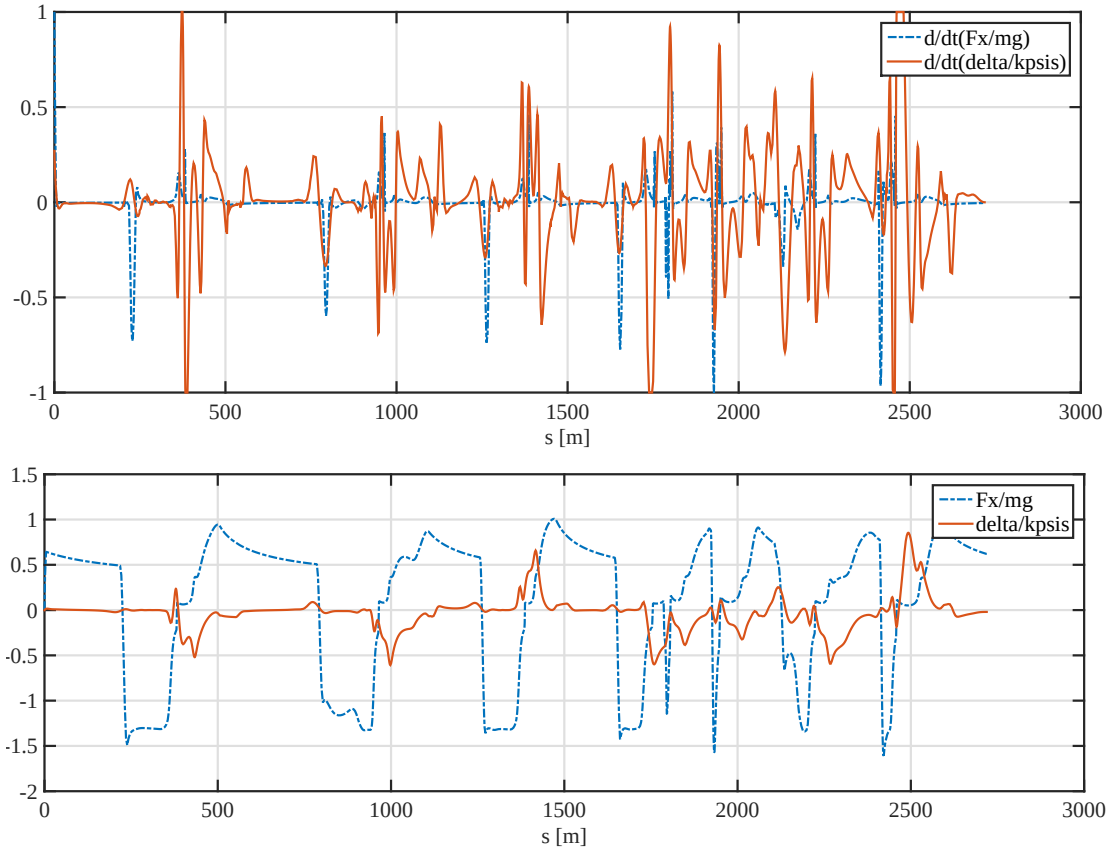

Figure 3.5: Control variables (top) and corresponding integrals (bottom).

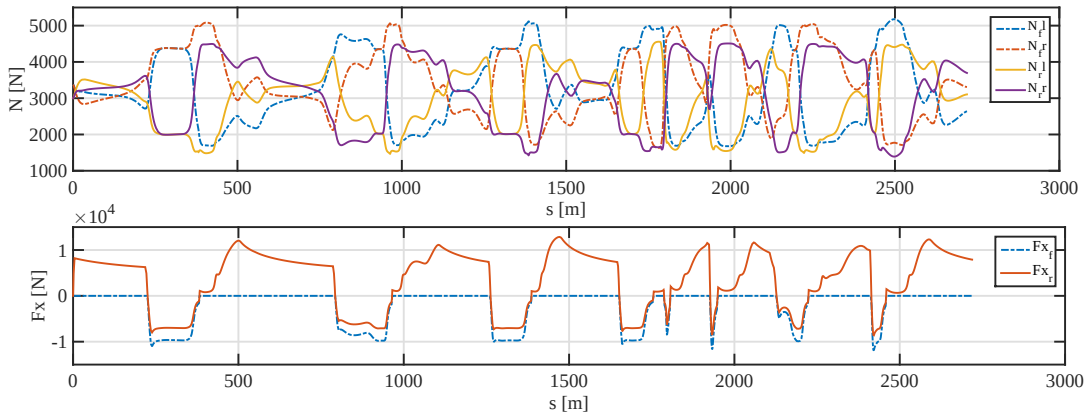

Figure 3.6: Normal loads (top) and longitudinal forces (bottom).

impress both positive and negative forces, while the front wheels are capable only of braking action and become zero during traction conditions. Moreover, it can be calculated that the ratio between front and total forces when negative values are applied to the four wheels is the constant *braking ratio* β.

As can be observed in fig. 3.7, the lateral acceleration of the CoM a_y remains in the interval $[-1.5g, 1.5g]$ and assumes positive values when the curvature is positive (right curves); the longitudinal CoM acceleration a_x, instead, is positive during traction and negative when the vehicle brakes; its value are limited in $[-1.4g, 1g]$. The intervals individuated depend mostly on the tyre characteristics, which are set in order to reach a realistic behavior. The real values (bottom figure) are obtained from the data unit positioned in the vehicle; as for a_y values the limits are overall respected, with exception to the effect of data noise and sampling distance. The considerations are much different for the a_x values, because during traction the real vehicle is capable of a lower acceleration: this observation has already been underlined when the real speed and the simulated data were compared; with the *basic model* the vehicle is capable of stronger longitudinal accelerations because the load transfer does not affect the adherence ellipses limits and no longitudinal slip occurs. Despite of that the overall profile form is respected and the vehicle is set up with enough accuracy to reach realistic behaviors of the dynamic quantities.

Thanks to the similarities between the real car dynamics and the model, this simulation is taken in consideration as a reference set of values, that allows to stress the main differences with the other modelling strategies and the different estimates for parameters. Therefore this *basic model* consists in a valid start point, from which can be implemented some complications, in order to simulate a more realistic vehicle behavior and, as a consequence, to discuss different strategies to improve the overall performance.

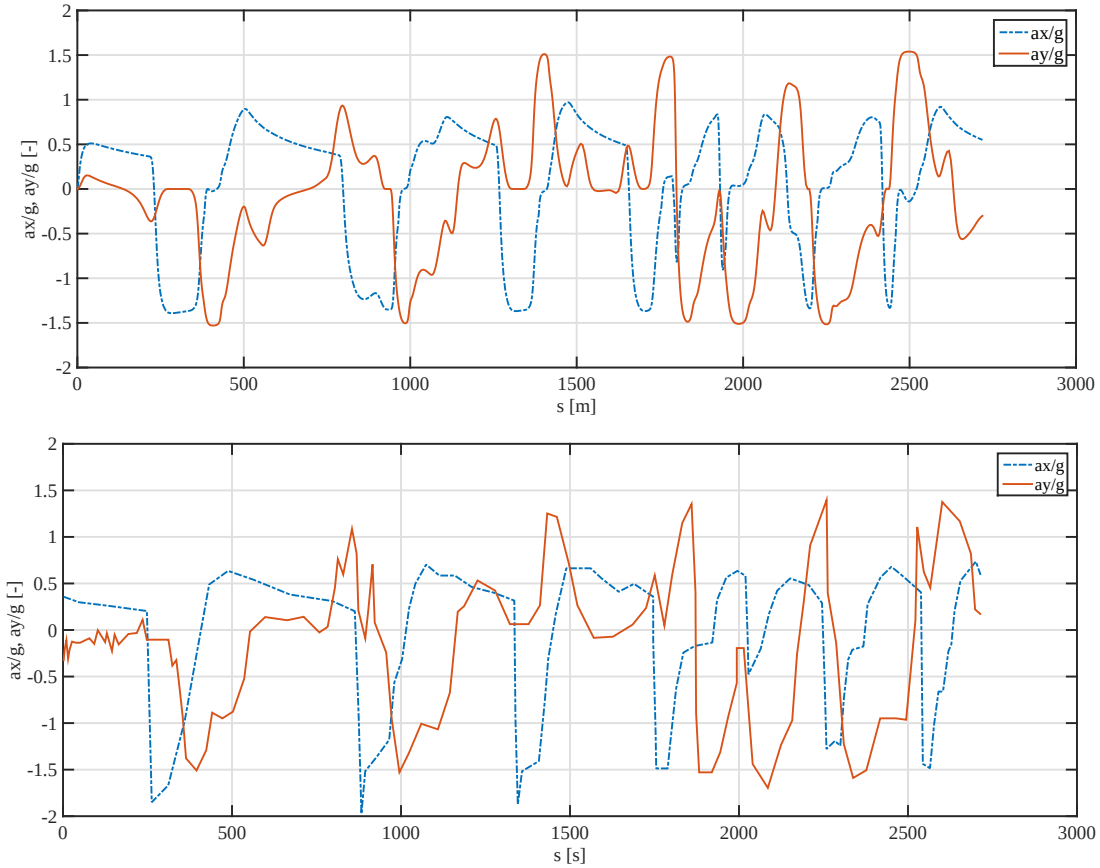

Figure 3.7: Simulated longitudinal a_x and lateral a_y acceleration of the CoM (top) and real values from vehicle unit (bottom); each value is normalized by the gravity acceleration g.

3.3 Simulation - Basic

After validating the car model with a circuit for which the real data was available, the simulations have been extended to different tracks, with peculiar characteristics, in order to achieve the best lap time performance. For the circuit of *Monza* it has not been considered the lift downforce for the vehicle, while for the track of *Imola* a value for the lift coefficient has been estimated, in order to obtain more realistic results; furthermore with this track both 2D and 3D road modelling are considered. A further analysis for the lift aerodynamic parameter is provided in sec. 4.8, where is developed a research of the optimum aerodynamic setup. In spite of that the model has been initially tuned up using proper tyre parameters that allowed to reach a realistic set of simulated quantities, without considering the lift forces: consequently the adherence parameters are able to compensate part of the aerodynamic lack.

3.3.1 Monza

Lap Time [s]	**CPU Time [s]**	**Penalties [s]**	**Real Time [s]**
107.645	237	0.065	107.584

Table 3.4: Simulation on *Monza* circuit.

The *Autodromo Nazionale di Monza* is a circuit with long straights and most of the curves, with exception of *Variante 1 e 2*, are passed trough at high speeds: the average speed is one of the highest of the whole GT3 championship calendar. Because of that the lift forces are not influent and the approximation of zero downforce is acceptable; these forces are obtained in the most part with the front spoiler and (for most) with the rear wing. In fast tracks it is important to reduce the drag force at minimum values and the rear wing is consequently set to reduce the attack angle, reducing inevitably both drag and lift (the ratio between drag and lift is typically constant).
The simulation leads to a lap time of 107.645 s that is comparable to a real time of 107.584 s (table 3.4). In this case the simulated time is slightly higher than the real one, owing to the estimated zero lift coefficient; nevertheless the real performance is close to the best performance affordable.
The whole track is represented in fig. 3.8 and underneath are magnified the most interesting curves. Considering the curves called *Variante 1* (mid left) and the *Variante Ascari* (mid right) it is possible to notice that the trajectory mirrors what should be expected: the vehicle attempts to exploit the whole track width to pass trough the corners with the maximum speed possible; moreover the distance between the CoM and the internal wheels is considered in the model constraints in order to obtain a more realistic behavior. Nevertheless these images are representative of an aspect that is difficult to introduce in the road modelling: the curbs both in the interior and exterior side of the corner. These parts of the track

are fundamental for the vehicles, that typically pass above the curbs to reduce the length of trajectory and to achieve a better traction after the curve exit, or braking before the entrance. With the models adopted the curbs are taken into consideration during the road point-to-point sampling, in which the borders are positioned adding part of the curb. In spite of that the dynamics of the model is not influenced by these borders and the vehicle, due to the constraints, is not capable of exploiting the whole curb.
The *Parabolica* curve allows to underline a realistic behavior for the vehicle that enlarges the trajectory for a better driving of the second part of the curve; furthermore the car, after enlarging the trajectory at the exit of the curve, maintains a rectilinear direction to better exploit the longer straight of the circuit.

In fig. 3.9 are reported the speed profiles for u, v, $V = \sqrt{u^2 + v^2}$ and Ω: the total velocity profile reaches values of more than 300 km/h; the modelled vehicle probably has some speed advantage in the straights respect to the real car, but it looses time when is turning in the fast curves, because of the aerodynamic setup chosen. The total velocity V is almost coincident to the longitudinal values u because the lateral speed v is not zero only when the car turns and reaches values of $10 \div 20$ km/h at maximum; the *yaw angular velocity* Ω (bottom figure) is positive for positive curvatures and reaches top values of $0.5 \div 0.8$ rad/s or $30 \div 45$ $^\circ$/s.

The *adherence ellipses* graphics (fig. 3.10) show that a good deal of points are recorded during straight acceleration or braking maneuvers; moreover the front wheels never use the full tyre capabilities neither when are directed as the symmetry axis of the vehicle nor when steering occurs. The rear tires exploit the entire limit ellipse only with the external wheel, although for these wheels is evident a better use of the adherence limits.

The normal loads (fig. 3.11) reach almost the same maximum values in the curves and the load transfer never causes the loss of load at any wheel; the longitudinal forces respect the constraints on all the domain of integration although are present some negligible high dynamic behaviors. These effects can be individuated also in the plot of the integrals of controls, that permits to evidence that the cause of this little vibrations are the controls themselves: to avoid this behavior it is possible to add penalties to the cost integrand and making consequently less favorable the use of controls (eq. (3.2)). The acceleration limits are almost the same of the simulation on the circuit of Adria.

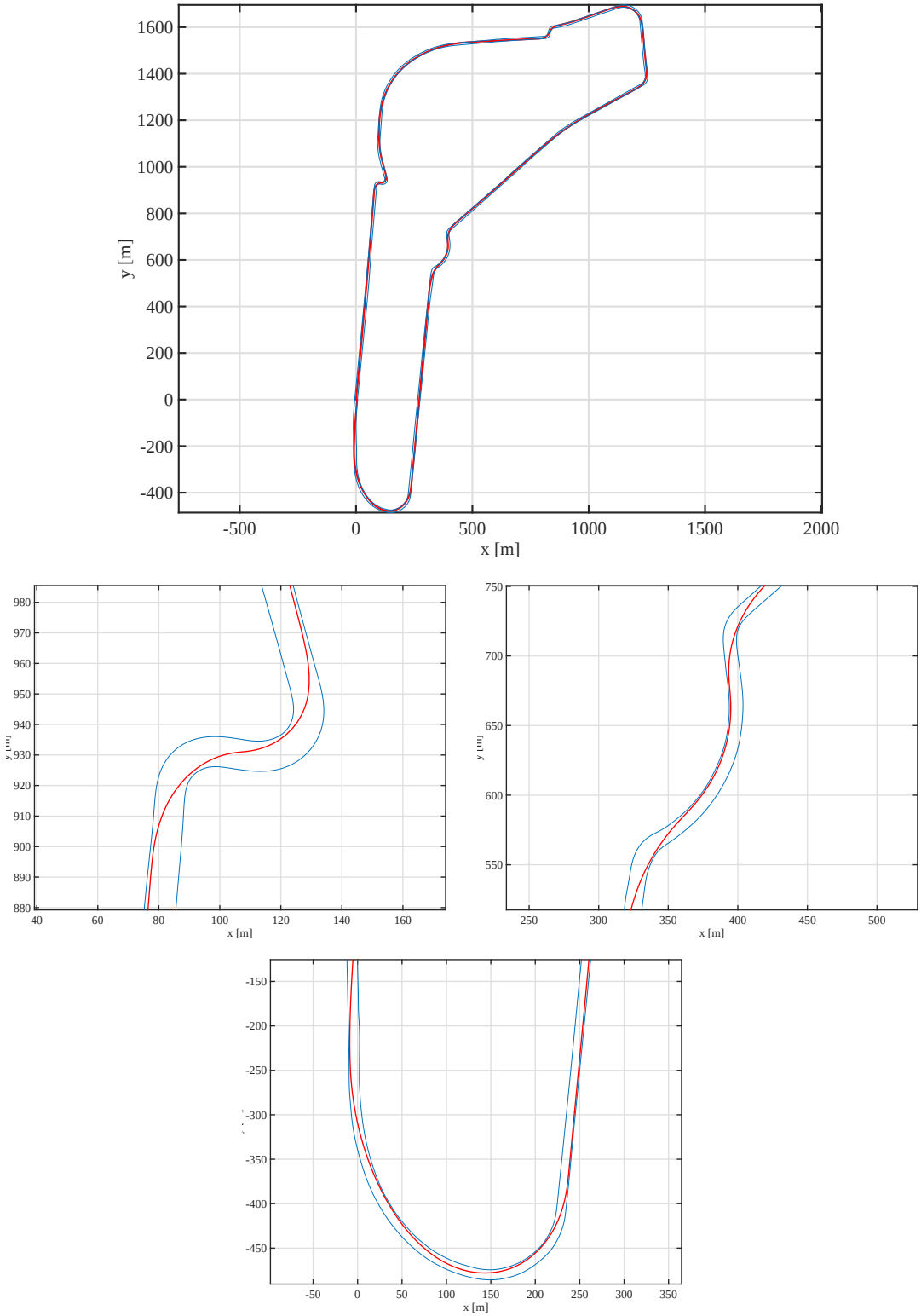

Figure 3.8: Monza circuit and simulated trajectory (top) with magnifications of *Variante 1* (mid left), *Variante Ascari* (mid right) and *Parabolica* (bottom).

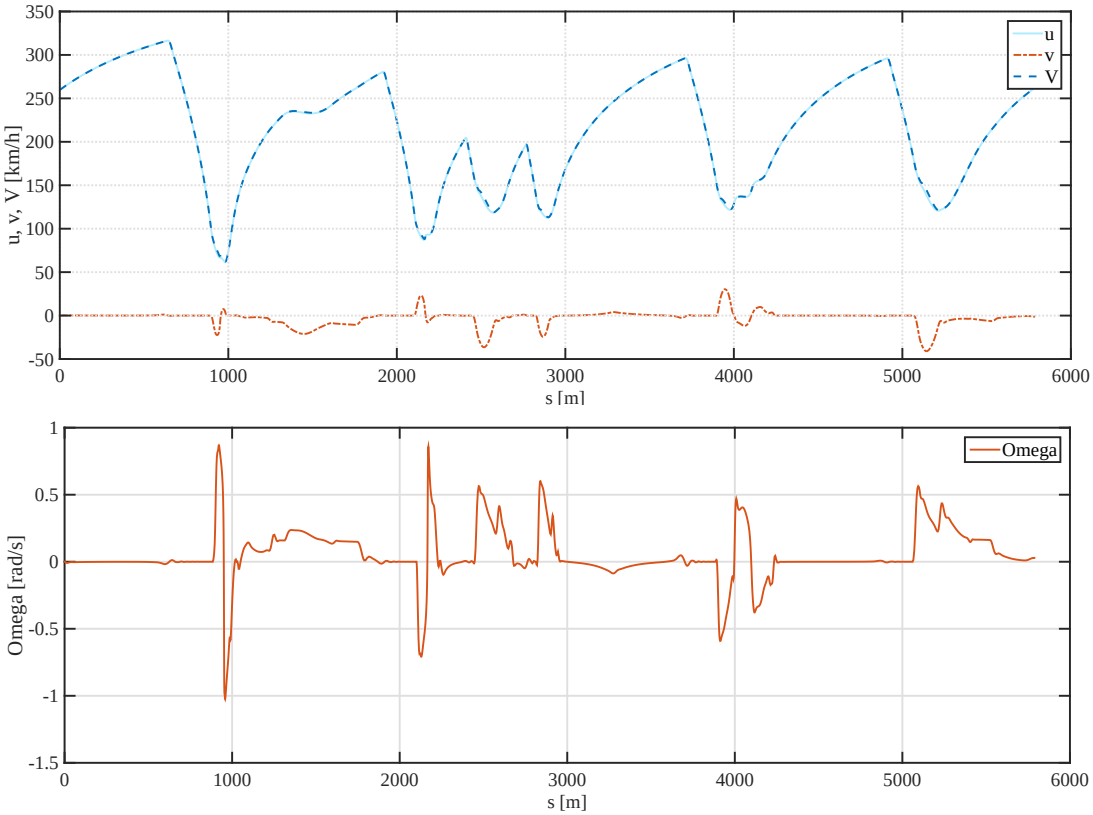

Figure 3.9: Simulated longitudinal, lateral and total speed profiles and angular velocity in z axis.

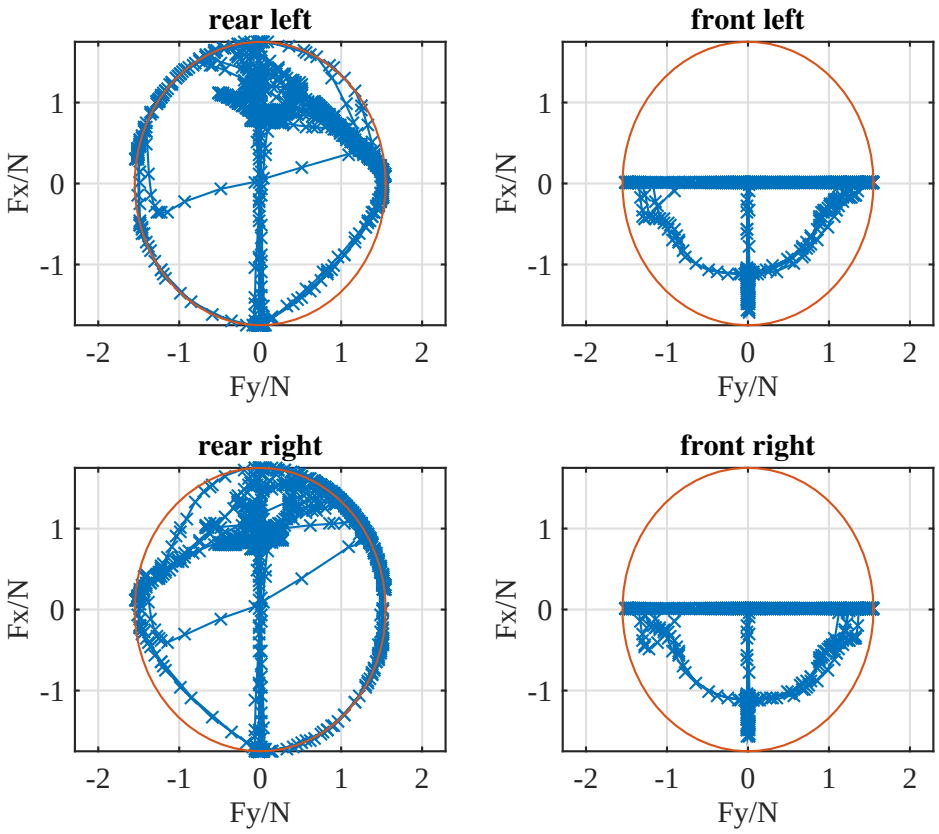

Figure 3.10: Adherence ellipses for the four wheels.

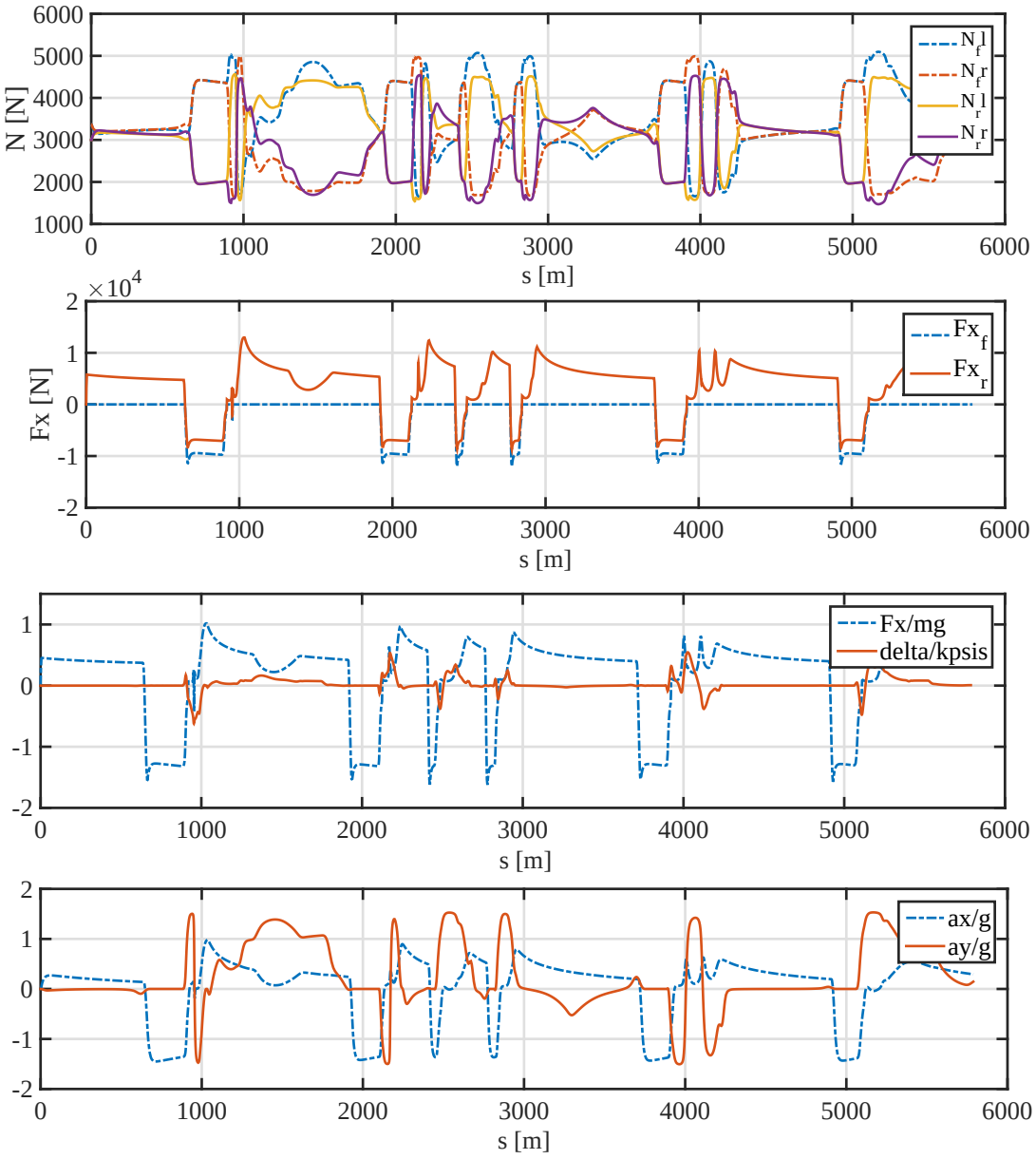

Figure 3.11: Normal loads (top) and longitudinal forces and controls (mid) and accelerations (bottom).

3.3.2 Imola

The *Autodromo Internazionale Enzo e Dino Ferrari* of Imola is known for the high technical complexity and for the altitude variation during the track. Because of that, the track has been built considering the altitude profile of the road and the car model employs the simplified tridimensional equations described in sec. 2.2.5. Moreover with this track the assumption of zero downforce does not allow realistic results and it is assumed a total lift area $C_L A = 2.8$ m^2 with $C_D A = 0.8$ m^2; the lift area is split in 70% for the rear and 30% at the front of the vehicle.
In terms of lap time (table 3.5) the 3D simulation is significantly close to the real best lap time while the flat track simulation determines a lap time advantage of 0.513 s, owing to the lack of parallel gravity component with a non-zero slope, and the effect of the *pitch inertia* I_y.

Imola 2D/3D	**2D**	**3D**	**Real**
Lap Time [s]	100.087	100.600	100.565
CPU Time [s]	490	492	–
Penalties [s]	0.104	0.100	–

Table 3.5: Simulation comparison between 2D and 3D simplified road reconstruction.

The circuit is reported in fig. 3.12 and the elevation is defined by a color scale from the blue (low elevation) to the yellow (high elevation); three famous corners are taken in consideration in order to underline the differences between the two-dimensional and tridimensional approach (fig. 3.13): the *Acque Minerali* downhill curve, the *Variante Villeneuve* with the following *Tosa* uphill curve and the *Variante Tamburello*.
As for the *Acque Minerali* the main difference is related to the entrance to the second part of the turn, that is anticipated for the 3D model in order to prepare the following uphill phase; in the *Variante Villeneuve* and *Tosa*, instead, the trajectory differences are not outstanding from the image, although a small difference is demonstrated comparing the curvilinear coordinate $n(t)$. Also in the *Variante Tamburello* is shown an evident difference for the two trajectories: the 3D one (left) employs more rounded variations of direction, in order to prepare the following uphill part of the track. These considerations can be also observed comparing the *lateral curvilinear coordinate* $n(t)$ in the two cased of study (fig. 3.14). In fact the *Acque Minerali* curve lays approximately at the curvilinear abscissa $s(t) \approx 2500 \div 2950$ m, the *Variante Villeneuve* and *Tosa* are at $s(t) \approx 1300 \div 1800$ m and the *Variante Tamburello* is at $s(t) \approx 600 \div 900$ m from the start point; it should be noticed that, correspondently to the curvilinear abscissa of the first and last corner described, the difference $\Delta n = |n_{2D} - n_{3D}|$ assumes the maximum values.

The normal loads show different profiles (fig. 3.15) because the longitudinal load transfer is more effective for the 3D model, due to the effect of the *pitch inertia* I_y during a variation of the slope. In fact higher peak values are available

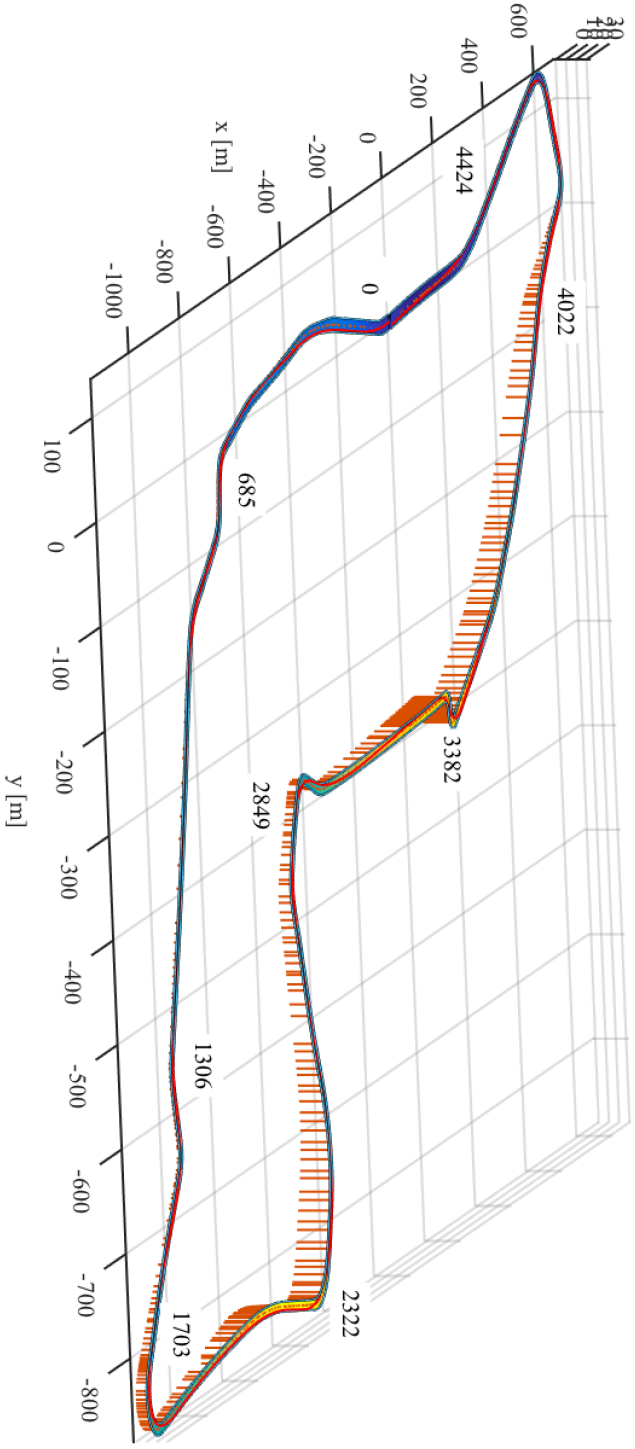

Figure 3.12: Track reconstruction, elevation (from blue for low values to yellow for high values) and trajectory.

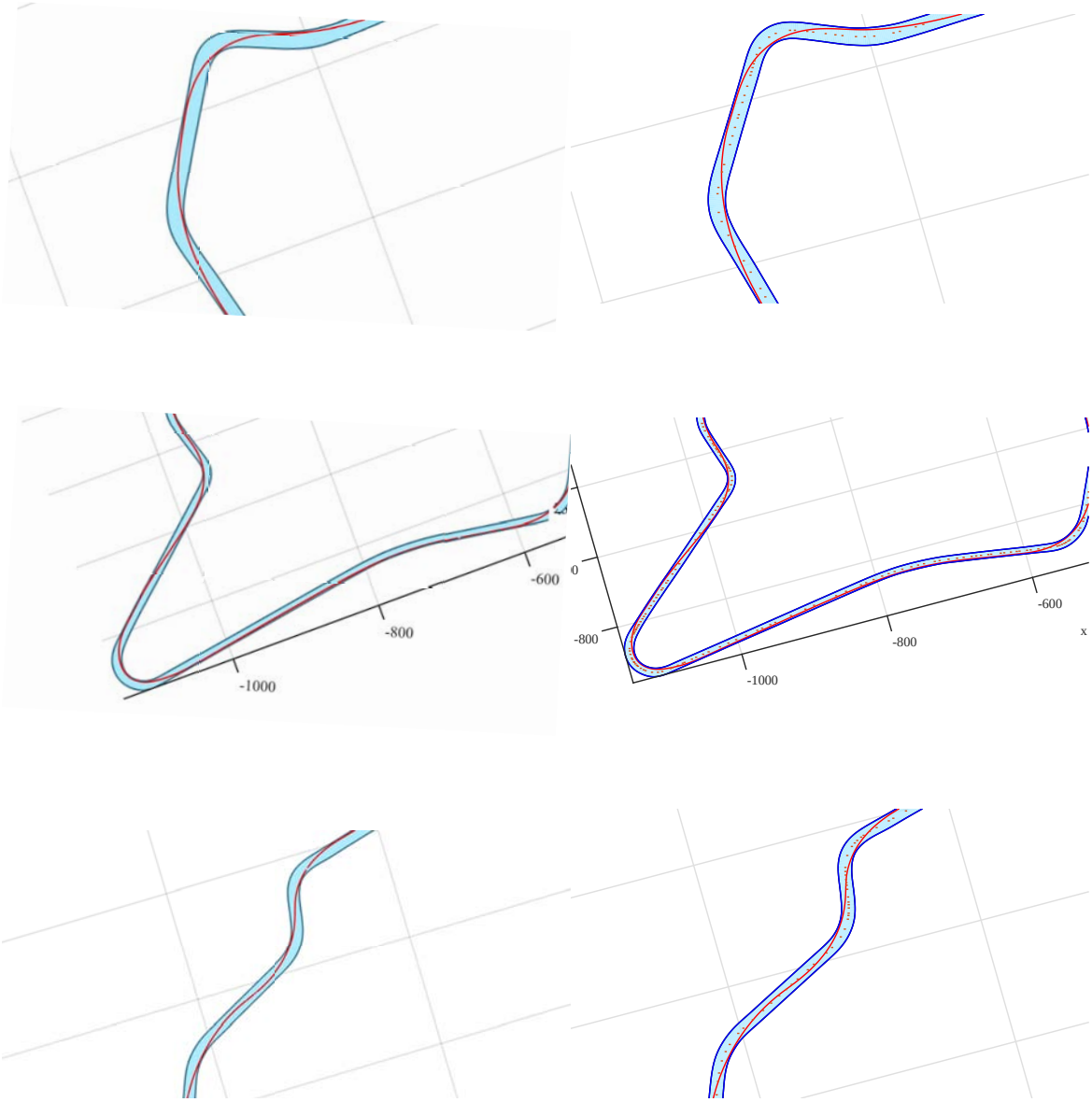

Figure 3.13: Magnified views of the corners *Acque Minerali* (top), *Variante Villeneuve* with the following *Tosa* (mid) and *Variante Tamburello* (bottom): the 3D turns are on the left side while the 2D curves on the right side.

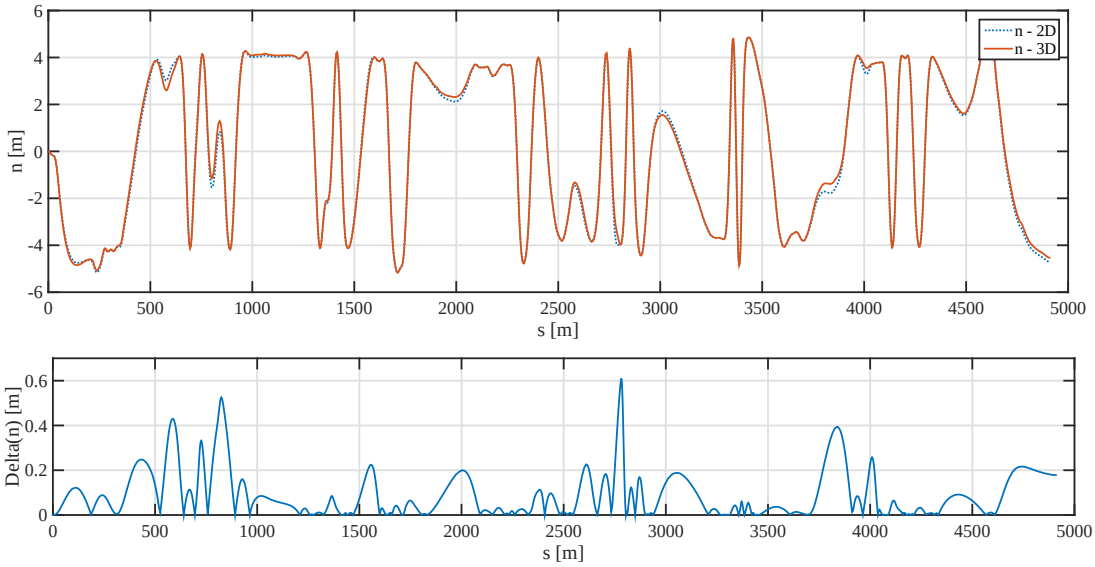

Figure 3.14: Curvilinear coordinates n for 2D and 3D representation (top) and difference between these values $\Delta n = |n_{2D} - n_{3D}|$.

for the model that implements the elevation, although the minimum values are approximately the same. Moreover different trajectories, as underlined previously, cause different effects on loads.
In fig. 3.16 are represented the longitudinal and lateral load transfer for the two models; the first ones are calculated for the right wheels and are positive when the rear loads are incremented, while the lateral transfers are shown for the rear wheels, with positive values for positive curvatures. It can be observed that the difference is not negligible where the road is subjected to a variation of elevation, although the overall behavior is maintained in the two cases. The difference between the longitudinal load transfer for 2D and 3D model presents negative peaks at s values of 1600 m, 2200 m and 3250 m from the start point: these points are all relative to uphill parts of the track where the longitudinal load transfer is positive and is greater for the 3D model. The positive peaks are related to the curvilinear abscissa of 2700 m and 4000 m, where the vehicle proceeds downhill; in these parts the load transfer becomes negative and the value for the 3D model is more negative than the one for the 2D simulation. As for the lateral load transfer the peaks are mainly connected to the differences of trajectory and occur where the slope changes, or rather almost in the same points of the longitudinal transfer peaks.

Also the velocity profiles of fig. 3.17 are macroscopically the same, although can be seen some slight differences in the main peaks: the 3D car is faster where the road proceeds downhill, while slower speeds than the two-dimensional model are registered in the uphill parts of the track. The 2D simulation reaches higher velocities at $s \approx 2200$, 3000 and 4000 m while the 3D simulation registers greater speed values for $s \approx 2600$ and 3900 m; these results are due to the road slope. Particular attention should be focused on the last peaks at $3900 \div 4000$ m, where the vehicle proceeds downhill until the following corners: in these conditions the 3D model reaches initially higher speeds although it anticipates the braking to

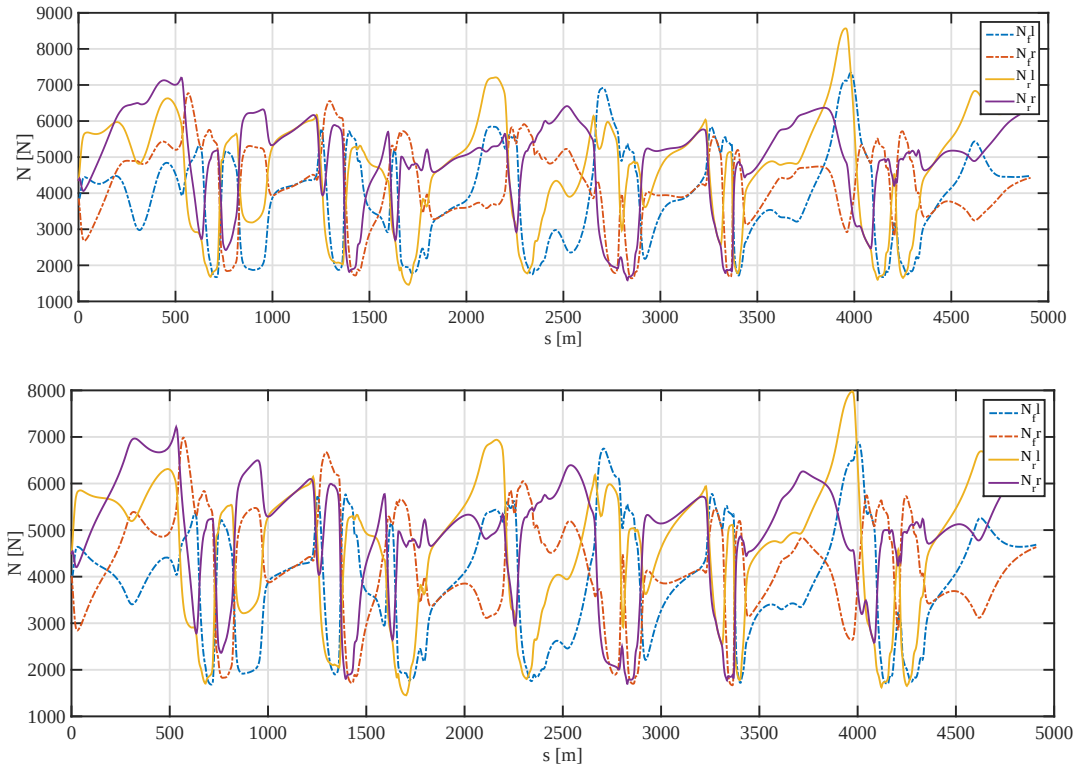

Figure 3.15: Normal loads for 3D model (top) and 2D model (bottom).

prepare the entrance to the curve, while the 2D simulation is capable of delaying the braking of a few meters; the two models, however, reach the corner with almost the same speed.

The same conclusions can be drawn considering the profiles of F_x and δ: although the differences are quite difficult to find comparing the complete curves, better results are obtained calculating the difference between the two different simulations (fig. 3.18). Positive peaks have the meaning of more power employed for the 2D model: this condition occurs at curvilinear abscissa values of 2700 m and 4000 m, or rather where the road is downhill; on the contrary negative values are connected to a lower power request for the 2D model, where the vehicle faces to positive slopes at $s = 1600$, 2200 and 3350 m. It should be noticed that the peaks occur when the longitudinal force passes from positive to negative: in other words it means that the main differences are due to different instants for starting the braking action: this is delayed uphill and anticipated downhill for the 3D simulation.

As for the *adherence ellipses* of figure 3.19 no overall differences can be highlighted: the two simulations are characterized by a similar exploitation of the tyre limits and both the front and rear tires present almost a complete usage of their capabilities. This result allows to underline the fact that the complete exploitation of the adherence capabilities is the real core of the time optimization: the achievement of the best performance depends most on reaching the ultimate adherence limits in any model used.

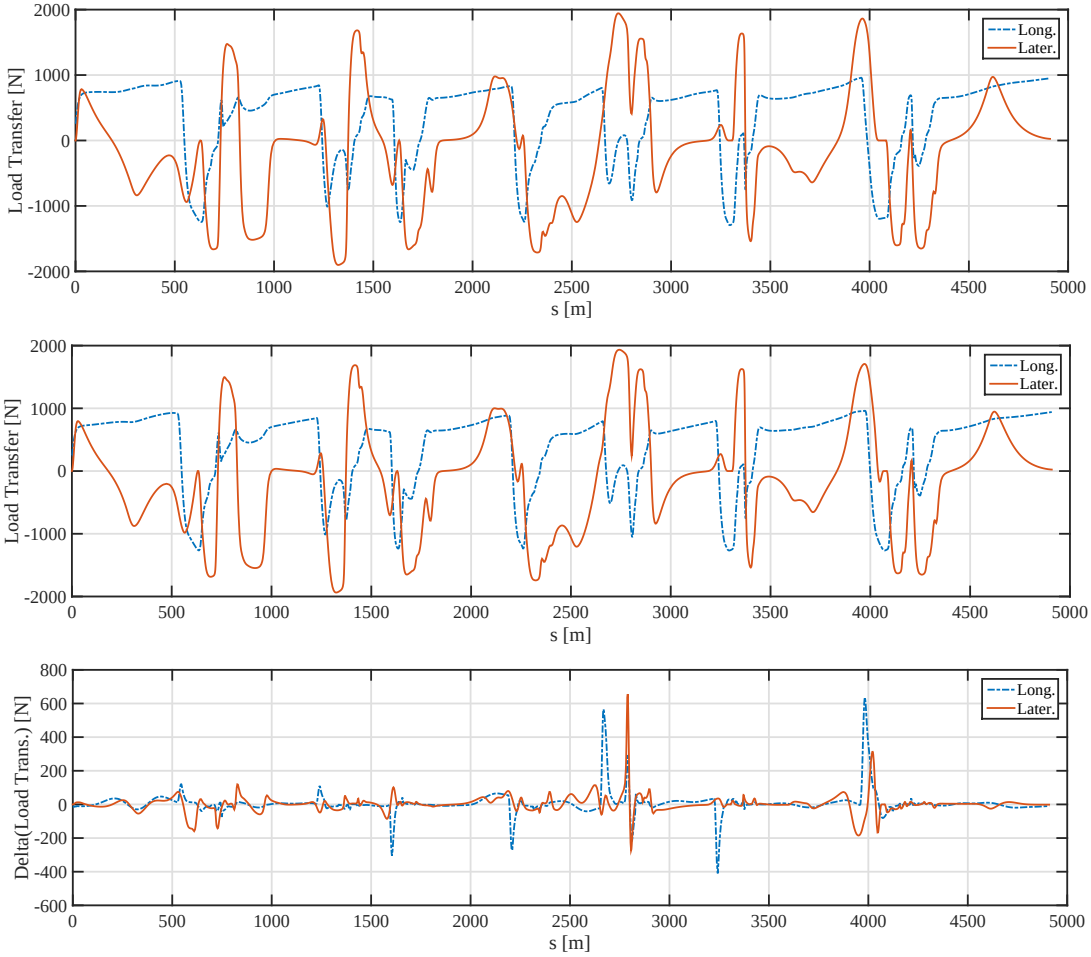

Figure 3.16: Normal loads transfer for 3D model (top) and 2D model (mid) and difference between 2D and 3D, $\Delta(\Delta N) = \Delta N_{2D} - \Delta N_{3D}$ (bottom).

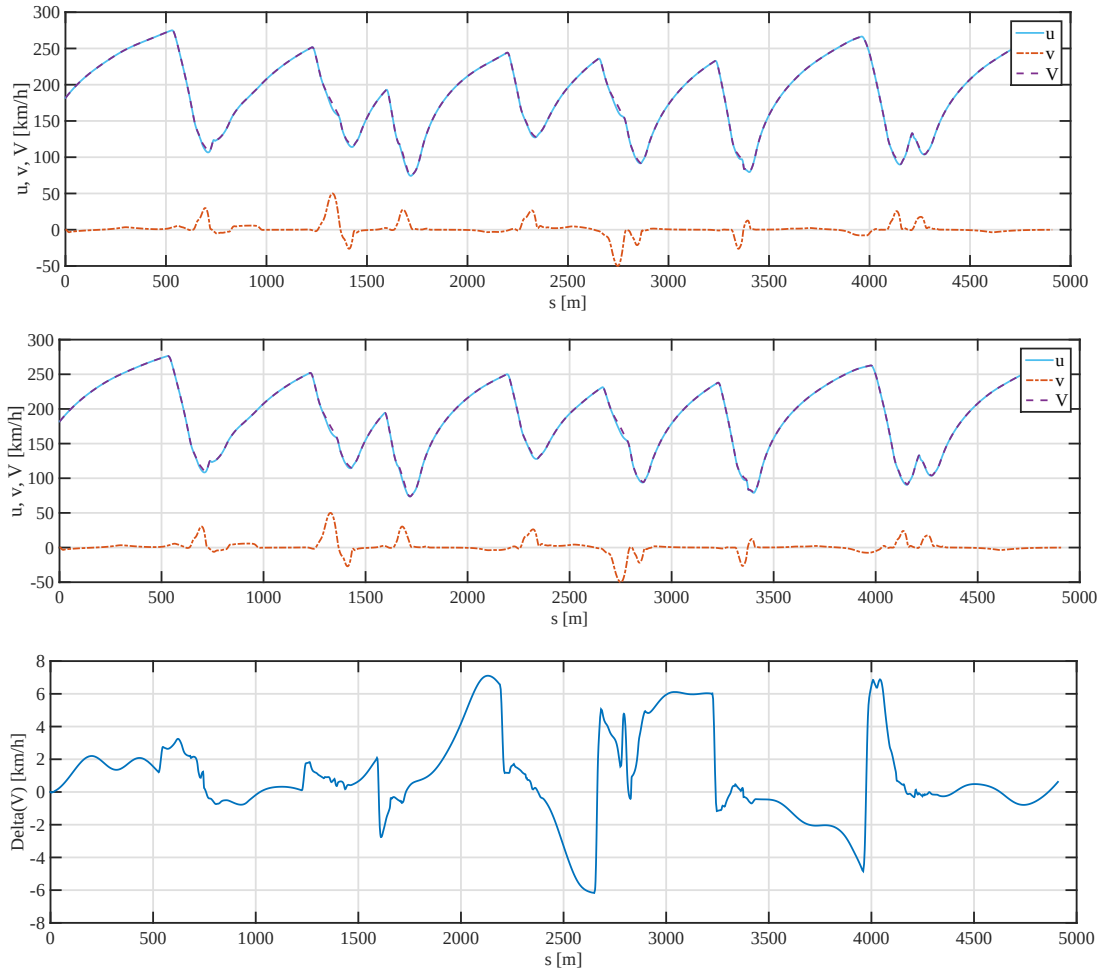

Figure 3.17: Velocities for 3D model (top) and 2D model (mid) and difference between 2D and 3D, $\Delta V = V_{2D} - V_{3D}$ (bottom).

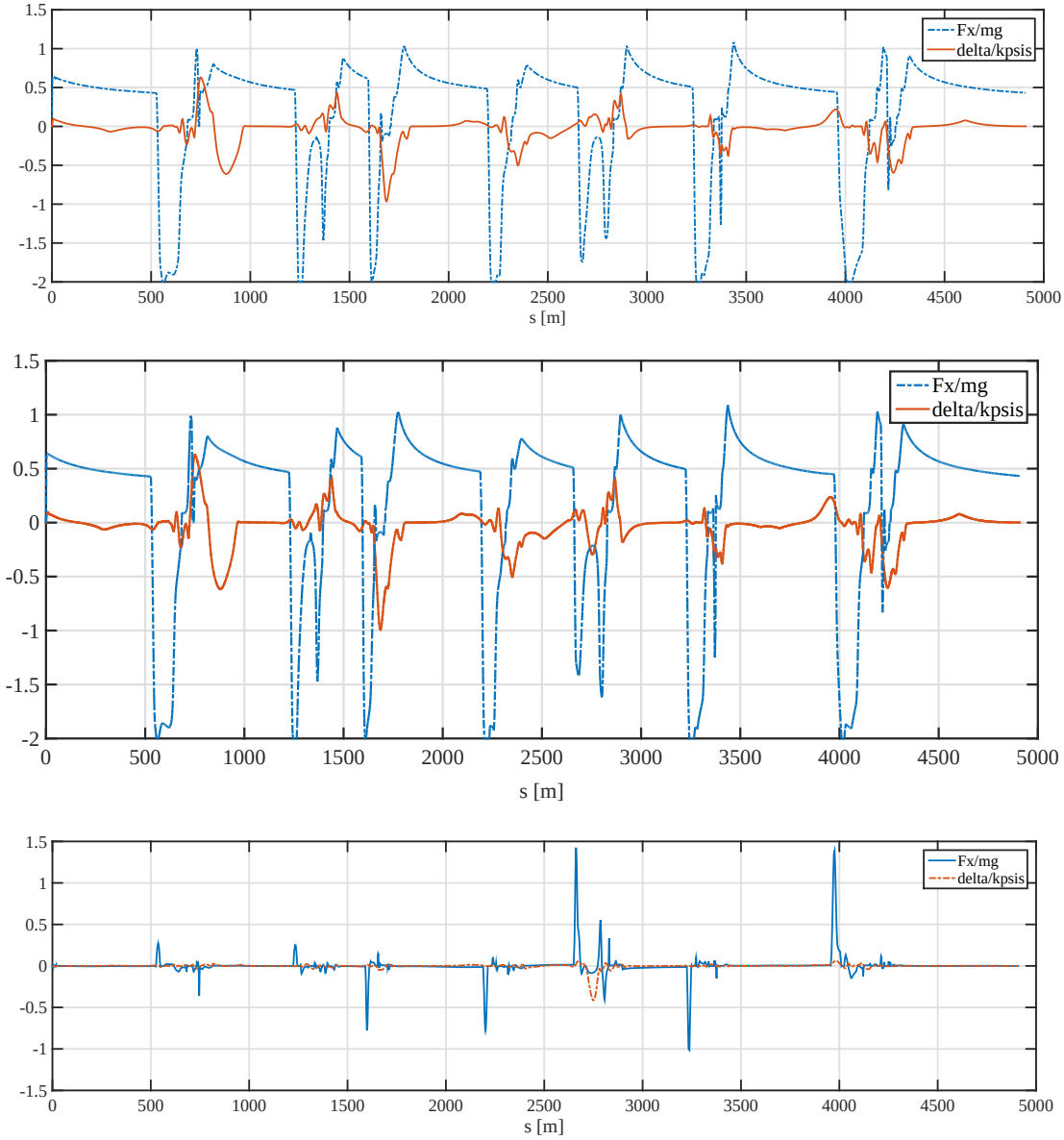

Figure 3.18: Integrals of the controls for 3D model (top), 2D model (mid) and difference of 2D and 3D values: $\Delta(Fx/mg) = (Fx/mg)_{2D} - (Fx/mg)_{3D}$, $\Delta(\delta/k_\delta) = (\delta/k_\delta)_{2D} - (\delta/k_\delta)_{3D}$.

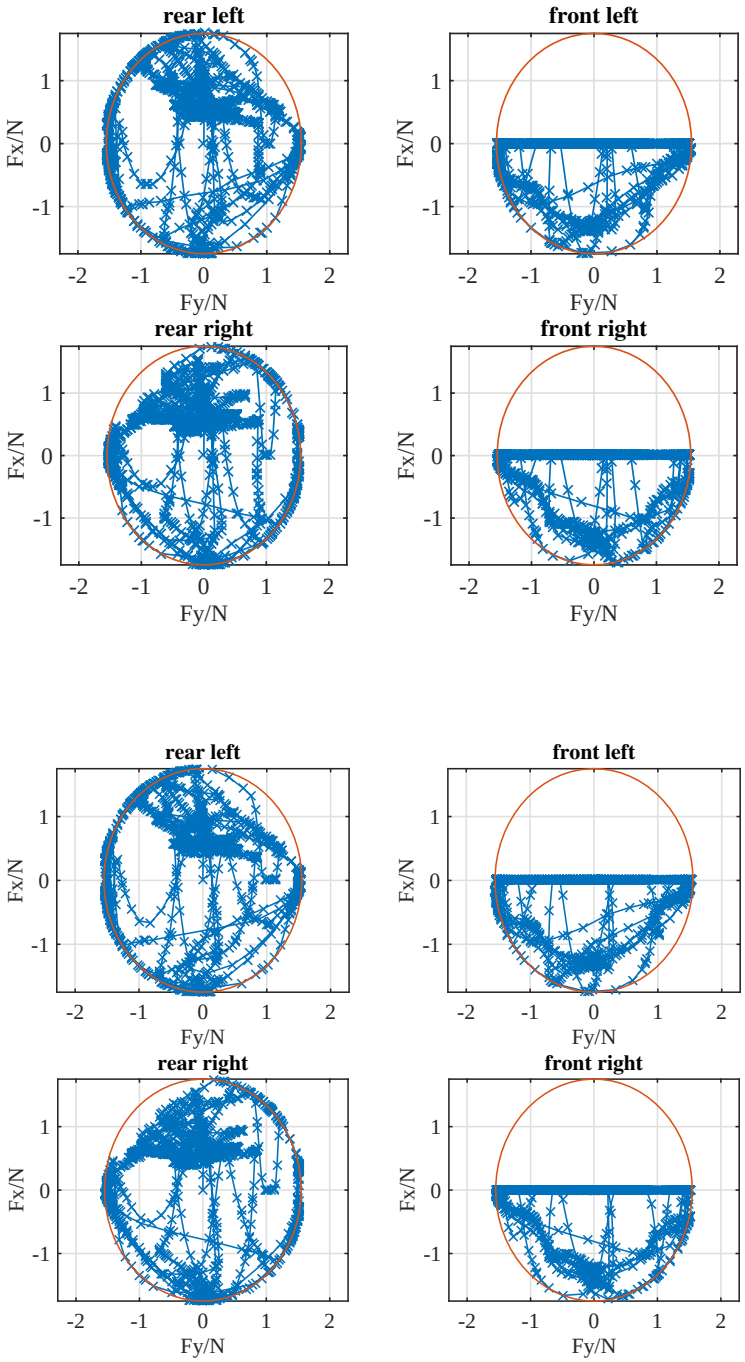

Figure 3.19: Adherence ellipses for 3D model (top) and 2D model (bottom).

3.4 Simulation - Slip-Slip

The *slip-slip* model offers some complications respect to the *basic* model that can be summarized in the implementation of the longitudinal slip κ and the Pacejka *Magic Formula*, developed in sec. 2.4. These two main differences determine different control strategies (eq. 3.16) and a substantially different dynamics that involves a complete combination of longitudinal and lateral tyre forces: in fact in the *basic model* the forces combination was only modelled with a constant elliptic boundary, independent from the loads; in this case, instead, the combination is load-dependent and the adherence diagrams are no more elliptic. Consequently the optimal control solution is drastically tougher to be reached and the computation time rises significantly. Moreover, because of the fact that no real tyre data is available, the *Magic Formula* coefficients are realistically assumed in order to obtain similar values to the previously ones adopted.
All these considerations may justify the achievement of different optimal solutions, although it must be underlined that including all the combined slip quantities, represents in general a drawback for the utter exploitation of the adherence limits of the vehicle.
However, the simulations proposed will emulate the same circuits and the same parameters used in the previous section, in order to develop a proper comparison of these different strategies of modelling.

3.4.1 Adria

The simulation on the *Adria International Raceway* has permitted to improve the ideal performance lap time from 76.398 s of the *basic* model to the 75.211 s of the *slip-slip* model of the vehicle, although the time needed to complete the simulation is incremented of more than three times (table 3.6). These results are due to a more complex model of tyre in which the longitudinal and lateral forces are not calculated independently. Moreover the tyre data has been assumed in order to obtain similar values to the coefficients used in the previous model, considering static conditions. In spite of that, it must be underlined that the coefficients chosen for the *slip-slip* model, which define a more detailed form for the curves, generate slightly larger adherence ellipses: this becomes clear in fig. 3.20 and determines a relevant advantage for the dynamics.

Adria	**Slip-Slip**	**Basic**
Lap Time [s]	75.211	76.398
CPU Time [s]	884	191
Penalties [s]	0.138	0.075
Prev. Sol.	yes	yes

Table 3.6: Simulation comparison between *basic* and *slip-slip* model.

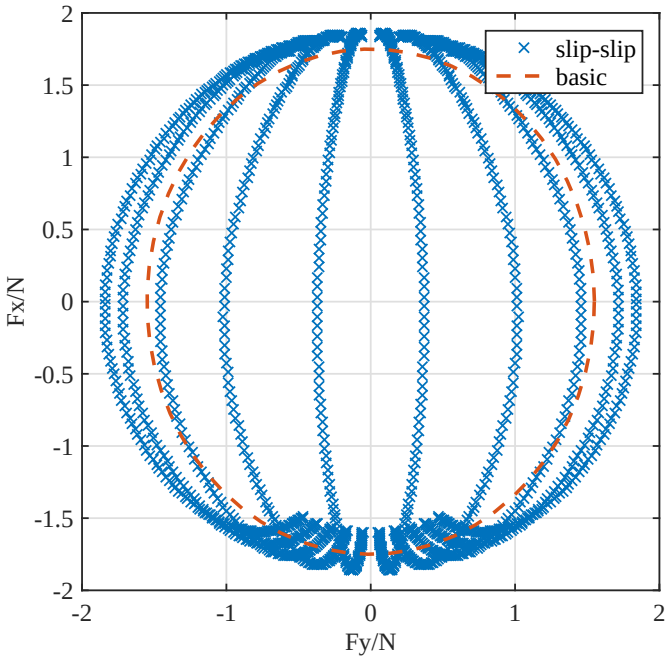

Figure 3.20: Adherence ellipses of the two models at static load value.

In figure 3.21 is reported the trajectory of the vehicle: the most evident differences from the *basic model* simulation are related to the third corner ($s \approx 1300 \div 1500$ m) and the last corner ($s \approx 2400 \div 2500$ m). As for the third corner it can be observed that the slip model adopts a more rounded curvature both in the entrance and in the exit part, with a more complete usage of the road width; on the other hand the basic model uses a more straight trajectory before and after the corner, in order to better exploit the traction and braking phases. In fact, because of the complete forces combination and the effect of the lateral load transfer, the vehicle needs to limit the slip and the difference between the slip quantities of the interior and exterior wheels respect to the curve: this is achieved adopting a rounded and more gradual trajectory. On the contrary the basic model is not affected by the lateral load transfer and a more sharp trajectory is chosen to delay the braking and anticipate the full throttle phase. A different behavior can be observed for the last corner: the slip model uses a less gradual trajectory than the basic simulation while the curve exit are very similar; probably the first maneuver of approach of the corner, in which the slip model adopts a less evident steering action towards the exterior part of the curve, allows a lower load transfer variation that becomes an advantage for the slip quantities, that can be exploited for a faster maneuver.
The comparison of trajectory is also highlighted in fig. 3.22 considering the difference between the absolute value of the curvilinear coordinate $n(t)$ of the two models; it is clear that for $s(t) \approx 1300 \div 1500$ m and $s(t) \approx 2400 \div 2500$ m the maximum difference is calculated.

The optimal control problem has the peculiar property that it handles the control variables to reach the best performance and, therefore, obtain favorable

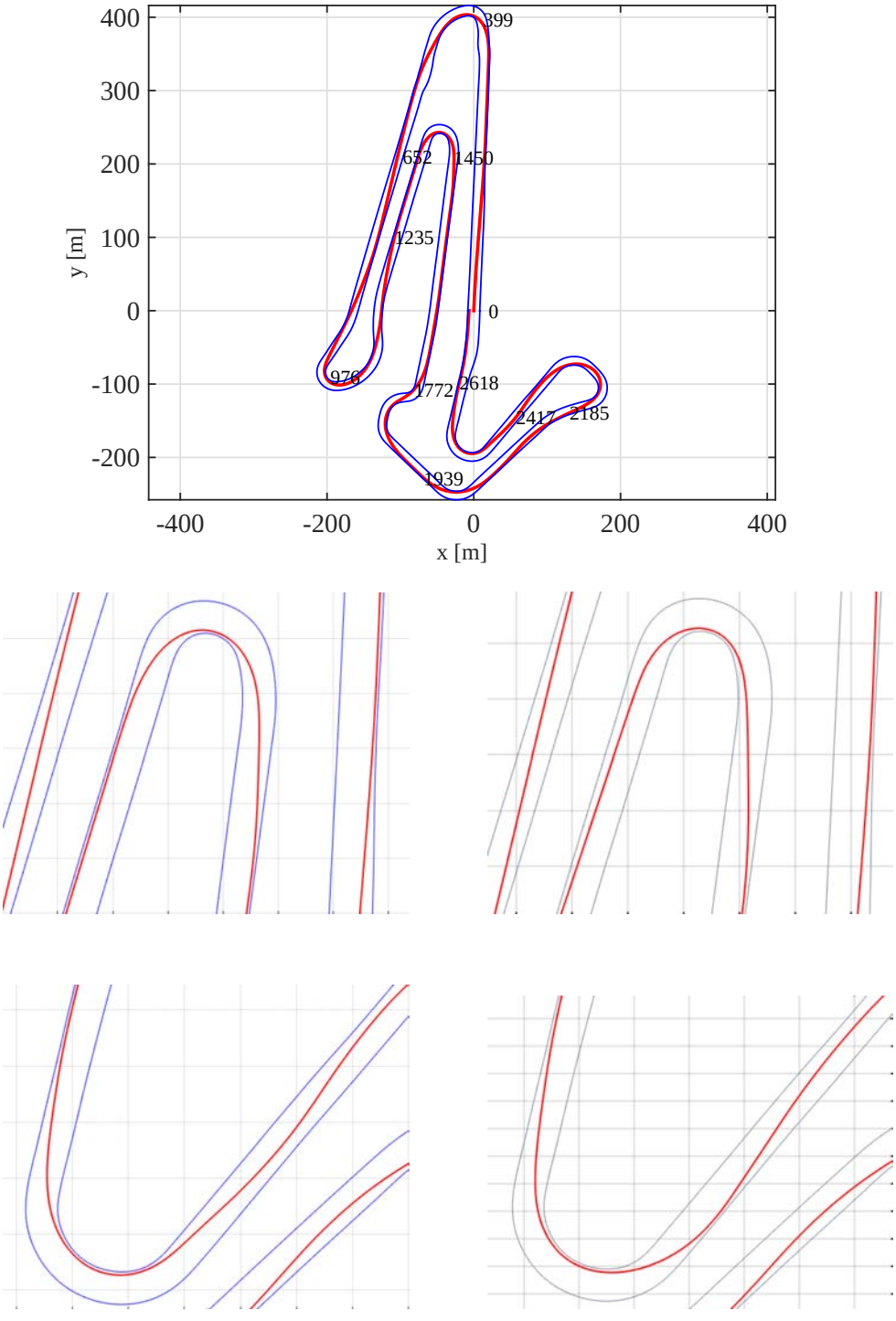

Figure 3.21: Track reconstruction and trajectory (top), turn 3 and turn 8 for *slip-slip model* (left) and *basic model* (right).

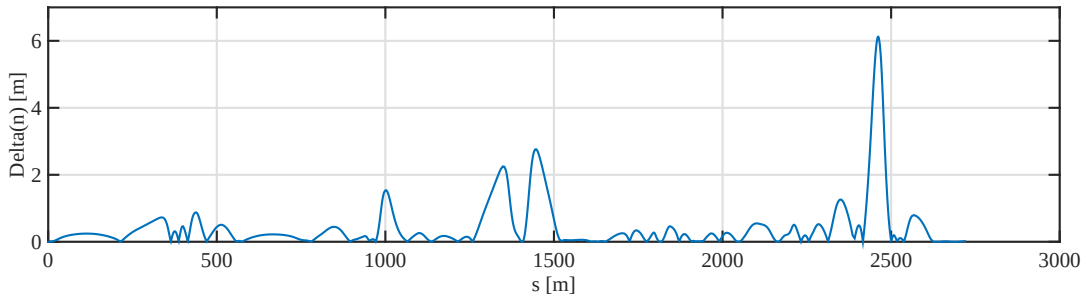

Figure 3.22: Absolute value of the difference between the curvilinear coordinate n of the *basic* and *slip model*: $\Delta n = |n_b - n_{ss}|$.

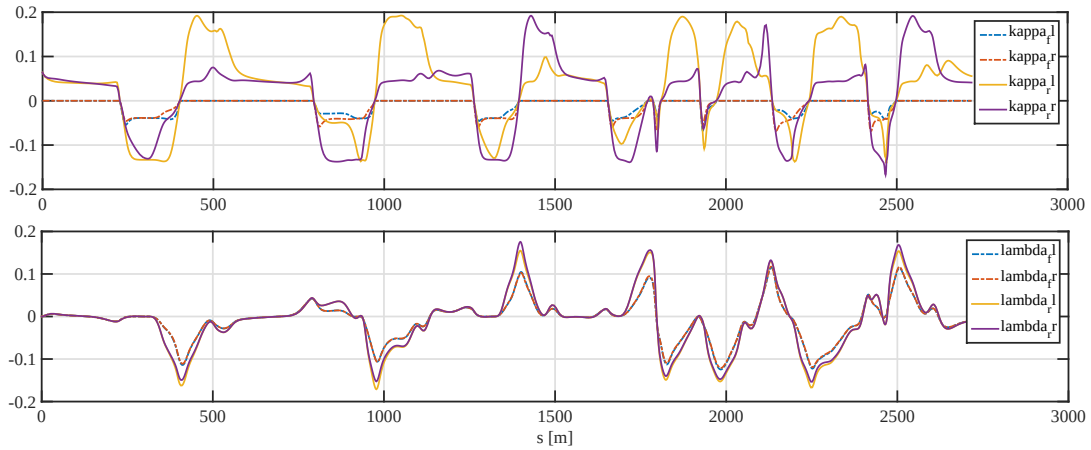

Figure 3.23: Longitudinal κ and lateral λ slip values for the *slip-slip* model.

values for the most important quantities. The profiles of the longitudinal and lateral slips, shown in fig. 3.23, demonstrate this observation: the controls, in fact, are related to the longitudinal slip κ while the lateral slips λ are calculated as a consequence. Owing to the lateral load transfer and the *lateral slip angle* in turning conditions, a greater κ value for the external tyre is needed, because the higher load reduces the slip limit; consequently proper values of λ are obtained with proper maneuvers, in order to reach the maximum slip value at the peak of the force profile.

Regarding loads and loads transfer for the slip model (fig. 3.24) the profiles emulate the ones of the basic model, although some differences are underlined because of the different points in which the vehicle starts braking or full accelerating phases. A significant difference is obtained at the last corner of the track: during the braking action the slip model achieves a lower longitudinal load transfer and a lower value for the lateral load transfer; in these conditions, in fact, $\Delta N_{lon} = N_{rr} - N_{fr}$ is negative and the value of the basic model is more negative than the value of the slip model; moreover $\Delta N_{lat} = N_{rl} - N_{rr}$ is also negative because the vehicle is moving towards the external part of the track with reference to the corner. During the curve the signs of ΔN_{lon} and ΔN_{lat} become positive and the slip model reaches lower values of both the load transfers until the middle

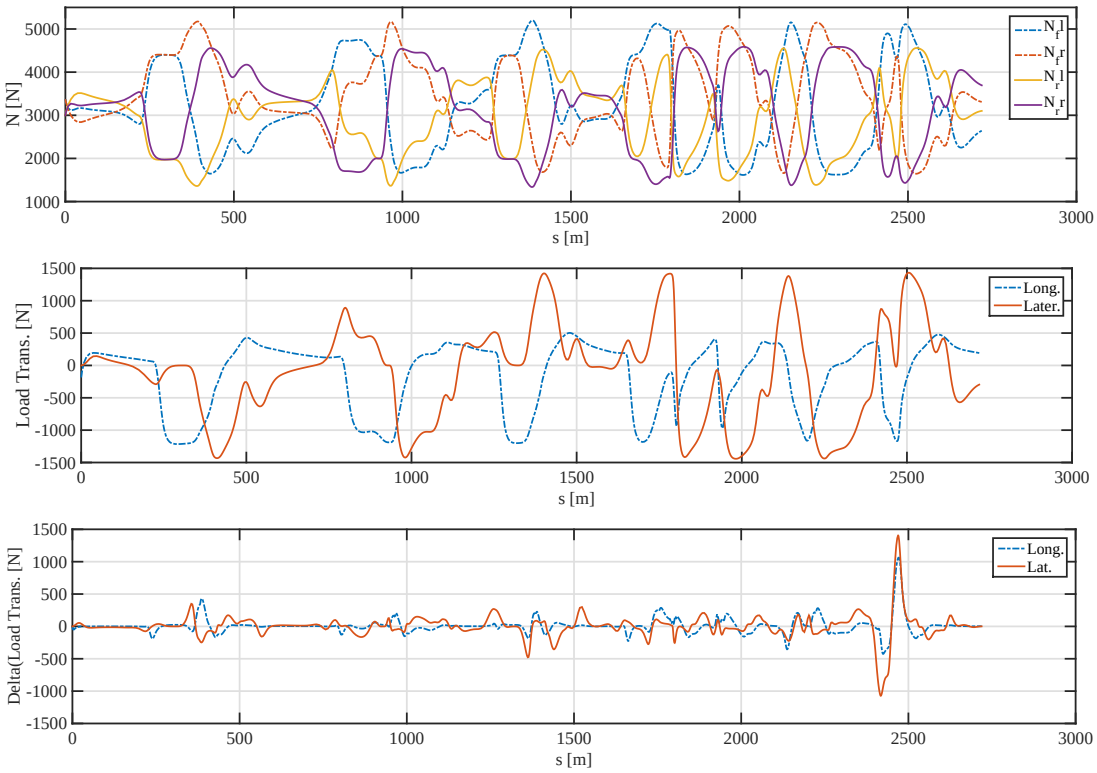

Figure 3.24: Normal loads (top) and loads transfer (middle) for the *slip-slip* model and difference between slip and basic model, $\Delta(\Delta N) = \Delta N_b - \Delta N_{ss}$ (bottom).

of the corner ($s \approx 2500$ m), where the values become more similar. Therefore the slip-slip model employs the strategy of reaching lower load transfer values in order not to penalize the adherence limits, that are decremented by a higher load value on the wheels.

The total longitudinal force $F_x = F_{xfl} + F_{xfr} + F_{xrl} + F_{xrr}$ (fig. 3.25) permits to express similar considerations for each corner: during braking the slip model exploits a lower force request, while in cornering conditions a lower power employment is requested. This means that the vehicle is capable of reaching good slip conditions with more gradual changes in the longitudinal forces; in other words the car avoids eccessive slip, or eccessive lack of adherence, with less braking action or acceleration. This behavior is magnified in the last corner, that seems significantly difficult for the slip-slip vehicle model.

The previous considerations are completed with the speed profiles of fig. 3.26, in which is clear that the module of vehicle velocity V is higher for the slip model during braking and lower in the first part of the corner; the vehicle is faster before the curve, because it brakes less, and is slower during the turning condition because less speed was dissipated: the vehicle enters faster in the curve, reduces gradually the speed, loosing time in the first half of the corner and definitely takes advantage of a better traction during the exit. These considerations are verified for most of the corners except the third turn, in which the slip model is faster, in average, than the basic one.

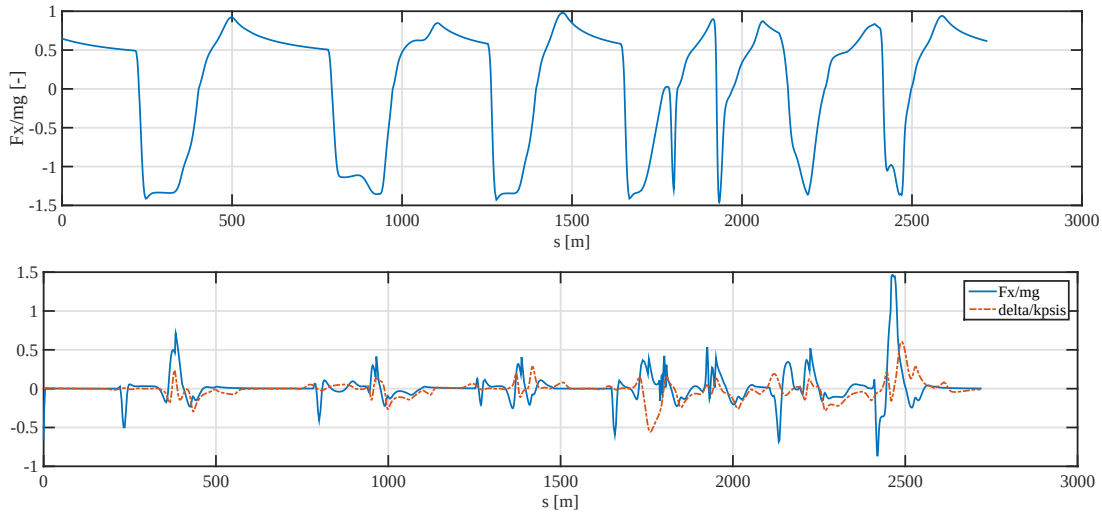

Figure 3.25: Total longitudinal force profile for the slip model, normalized by the weight force (top), and comparison between slip and basic model: $\Delta(Fx/mg) = (Fx/mg)_b - (Fx/mg)_{ss}$ (bottom).

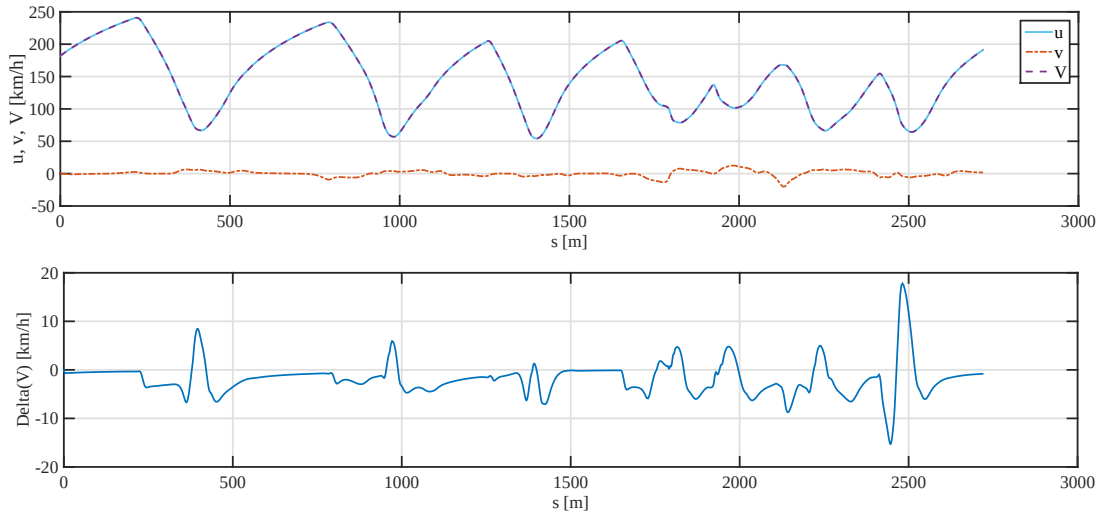

Figure 3.26: Velocity profiles for the slip model (top) and comparison between slip and basic model: $\Delta V = V_b - V_{ss}$ (bottom).

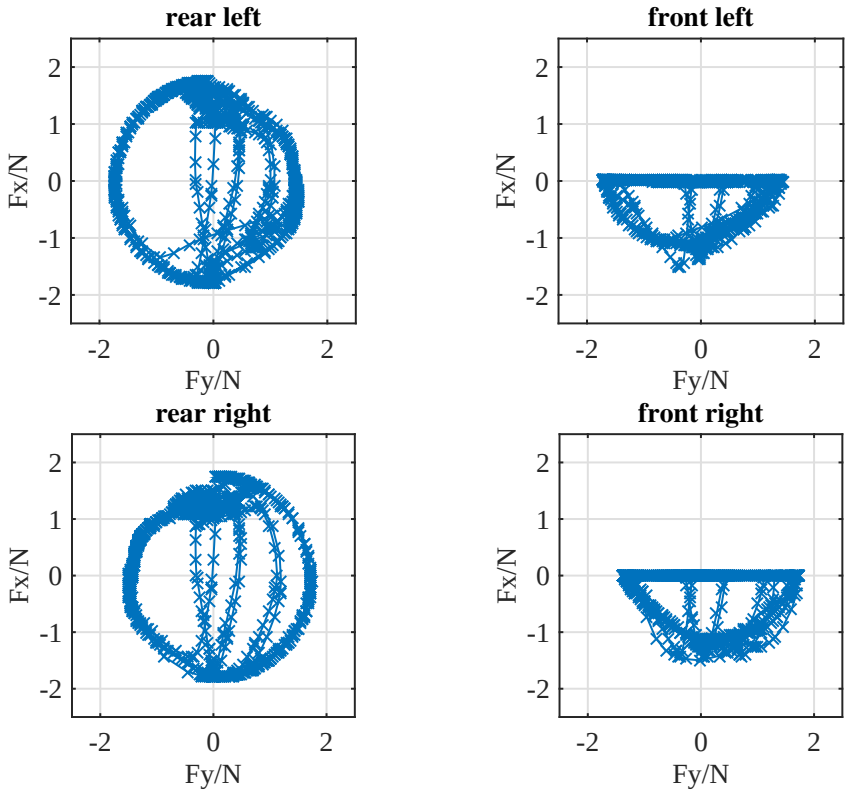

Figure 3.27: Adherence ellipses for the slip model.

In fig. 3.27 are represented the adherence ellipses obtained with the slip-slip model; in this case the adherence limits are not constant with the load and the form is not properly elliptic because present the typical curls for which, decreasing the lateral adherence coefficient F_y/N, the longitudinal friction coefficient F_x/N increases until, under certain values of F_y/N, F_x/N is definitely reduced (see fig. 2.8). However the vehicle exploits almost the whole adherence domain, which is tightly connected to the achievement of the best performance.

3.4.2 Monza

Also simulating the vehicle dynamics on the *Autodromo Nazionale di Monza*, the lap time reached with the *slip-slip* model (106.298 s) is lower than the result obtained with the *basic* model (107.645 s); in the same way the time requested for the simulation is extremely larger, also because of the lack of a previous solution from which can be set the initial guess of the problem. The tougher numerical characteristics of the problem are also stressed by the larger penalty time, due to the high usage of the control variables. For this simulation, as well as for Adria, no lift forces are provided and the drag area is assumed as $C_D A = 0.65$ m^2.

Monza	**Slip-Slip**	**Basic**
Lap Time [s]	106.298	107.645
CPU Time [s]	2025	237
Penalties [s]	0.132	0.065
Prev. Sol.	no	yes

Table 3.7: Simulation comparison between *basic* and *slip-slip* model.

In fig. 3.28 is reported the road profile and two particular corners are magnified: the *Curva Biassono*, located at $s \approx 1100 \div 1700$ m and the *Parabolica* at $s \approx 4900 \div 5600$ m. These values of the curvilinear abscissa represent the parts of the track in which it is more evident the trajectory difference between the slip and the basic model. With reference to the entrance of the first corner considered, the two profiles are slightly different: in particular the slip model adopts a more gradual trajectory, while the basic model anticipates the entrance. At the curve exit the situation is similar: the slip model drives with a gradual strategy, enlarging the trajectory from the middle point of the corner; the basic model instead delays significantly the point in which the inner curb is left. The slip model therefore attempts to limitate the load transfer and consequently to optimize the adherence available, in order to have an advantage in the second part of the corner. On the contrary the basic model abuses of the constant adherence available and adopts straight trajectories to reduce the distance traveled. The considerations made can be transferred to the *Parabolica* curve: the *slip-slip* model anticipates the maneuvers of entrance and exit of the corner, for a more gradual use of the adherence limits, while the basic model privileges a more rectilinear trajectory, delaying the entering and anticipating the exit. Moreover a difference can be also noticed in the middle part of the corner, in which the basic model uses a larger trajectory while the slip model remains in contact with the curb, in order to anticipate the exit maneuver.
The representation of the parameter Δn between the two models (fig. 3.29) remarks the differences individuated.

The slip quantities are represented in fig. 3.30, which shows that the two curves taken into consideration are related to high slip values with a long duration: this is the cause of the significant difference of trajectory. It should be observed that

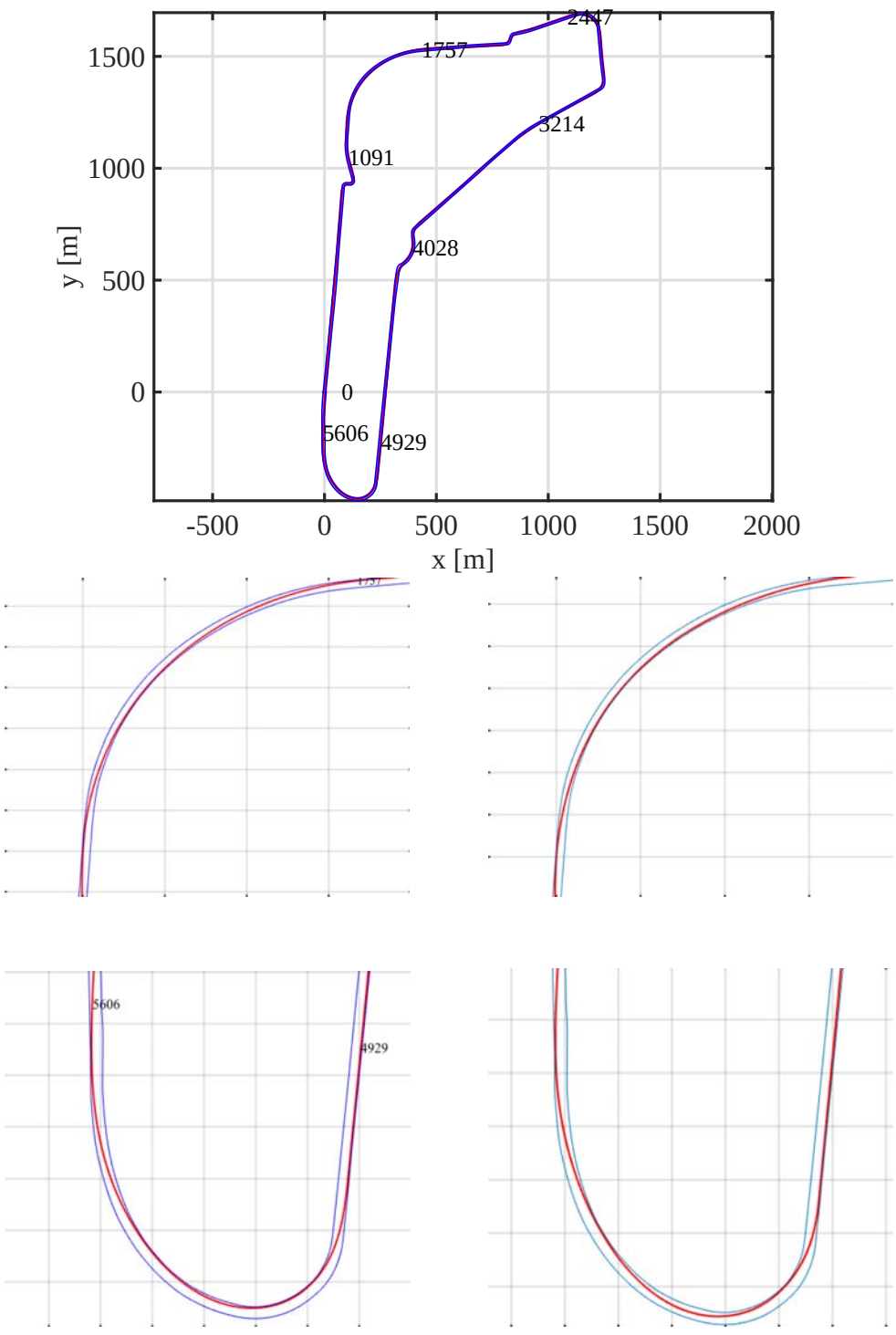

Figure 3.28: Track reconstruction and trajectory (top), *Curva Biassono* and *Parabolica* for *slip-slip model* (left) and *basic model* (right).

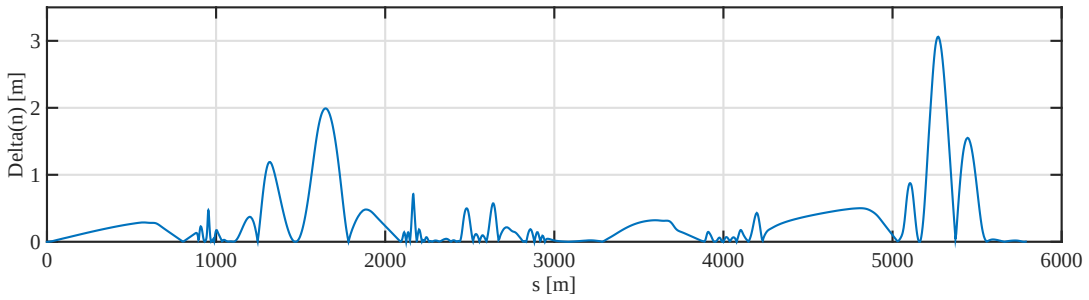

Figure 3.29: Absolute value of the difference between the curvilinear coordinate n of the *basic* and *slip model*: $\Delta n = |n_b - n_{ss}|$.

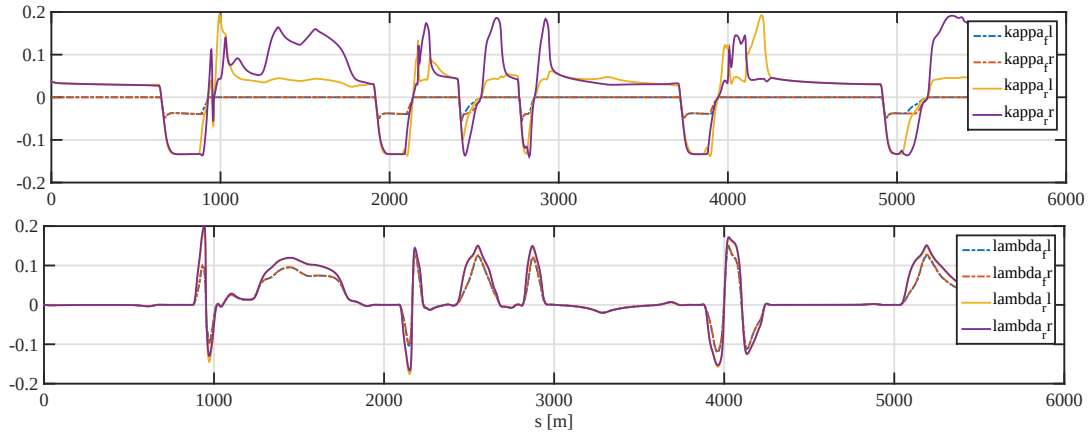

Figure 3.30: Longitudinal κ and lateral λ slip values for the *slip-slip* model.

during traction the longitudinal load transfer determines a lower slope for the tyre function and definitely higher values for κ are needed in order to achieve proper longitudinal forces; the lateral slips λ are lower for the front wheels because of the steering angle δ (see eq. 2.8).

The load transfer profiles are regular and free from vibrations; it should be observed that the loads never approach the unloaded condition, thanks to the high roll stiffness K_ϕ of the car and the elevate value of the track T. As considered for Adria, the longitudinal load transfer for the slip model is lower both during braking and in phase of acceleration owing to the possibility of using higher values for the adherence; this behavior is easy to observe in the *Parabolica* curve. In the *Curva Biassono*, instead, longitudinal and lateral load transfer are both positive and the values for the slip-slip model are greater than the ones which characterize the basic model: in fact, as shown previously, the slip model uses a more gradual trajectory that allows to travel in the second part of the curve with a higher speed, without reaching the adherence limits that, on the other hand, are reduced by the load transfer.

The normalized longitudinal force F_x/mg applied to the tyre contact points permits to confirm the previous analysis: the slip model approaches the corners with less braking force and proceeds using a lower force for traction; in that way the vehicle is able of using the whole adherence capabilities of the tires. Particular

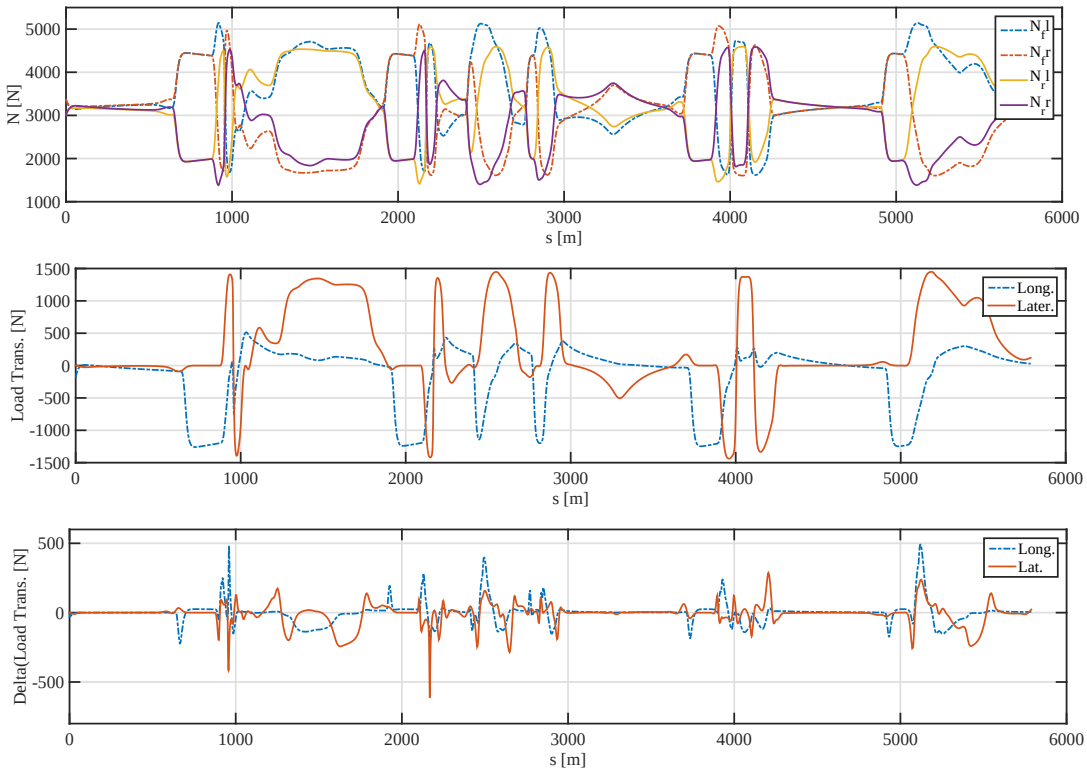

Figure 3.31: Normal loads (top) and loads transfer (middle) for the *slip-slip* model and difference between slip and basic model, $\Delta(\Delta N) = \Delta N_b - \Delta N_{ss}$ (bottom).

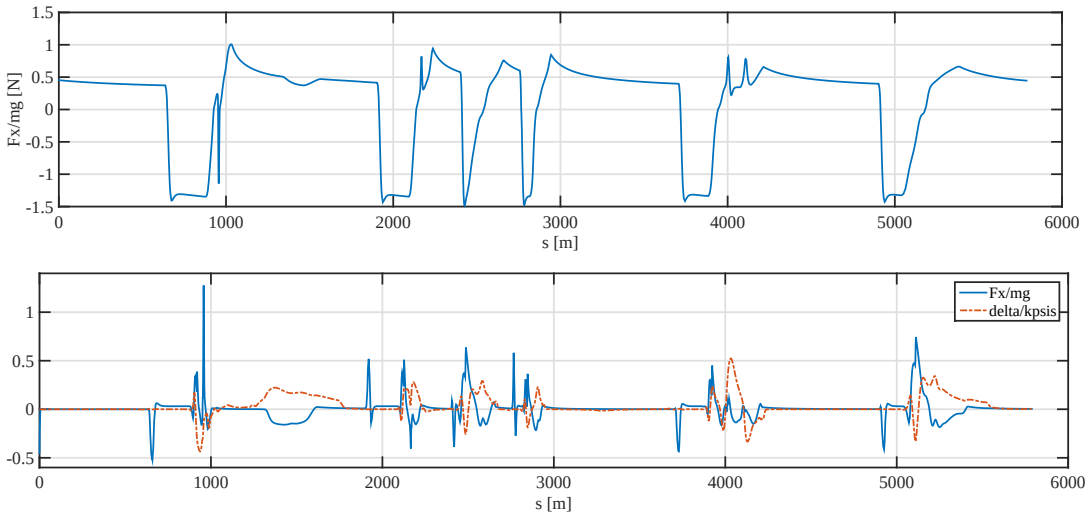

Figure 3.32: Total longitudinal force profile for the slip model, normalized by the weight force (top), and comparison between slip and basic model: $\Delta(Fx/mg) = (Fx/mg)_b - (Fx/mg)_{ss}$ (bottom).

attention should be focused on the *Curva Biassono* ($s \approx 1100 \div 1700$ m) in which the slip-slip vehicle adopts higher values for F_x and lower values for the steering angle δ: because of the gradual maneuvers of cornering entrance and exit, the ideal driver exploits the possibility of accelerating during the curve and, owing to the oversteering behavior and the lack of necessity of high slip limits, he manages to maneuver the vehicle with a lower steering angle.

The behavior described is highlighted also by the comparison of the total velocity V (fig. 3.33): in particular the *Curva Biassono* is travelled with a significant advantage of speed (15 km/h) by the slip model. In the other corners should be useful to notice that, once again, the slip-slip vehicle enters faster in the curves, looses consequently speed in the first part of the corner and exits faster because of the better traction condition.

As usual the adherence ellipses (fig. 3.34) are almost completely utilized both for front and rear tires. The points that seem not to follow the utter elliptic form of the curve in the front right tyre are probably due to the effect of the "curl".

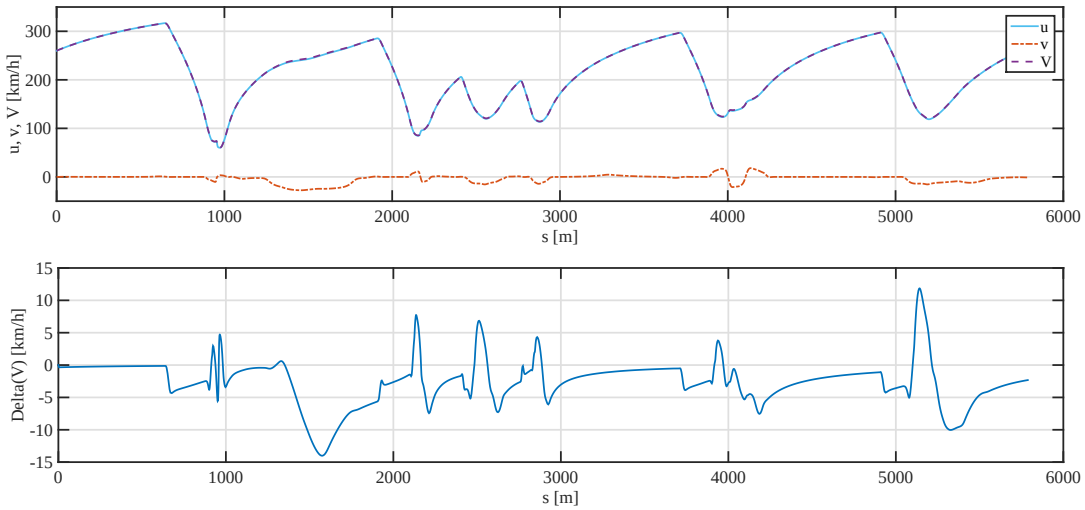

Figure 3.33: Velocity profiles for the slip model (top) and comparison between slip and basic model: $\Delta V = V_b - V_{ss}$ (bottom).

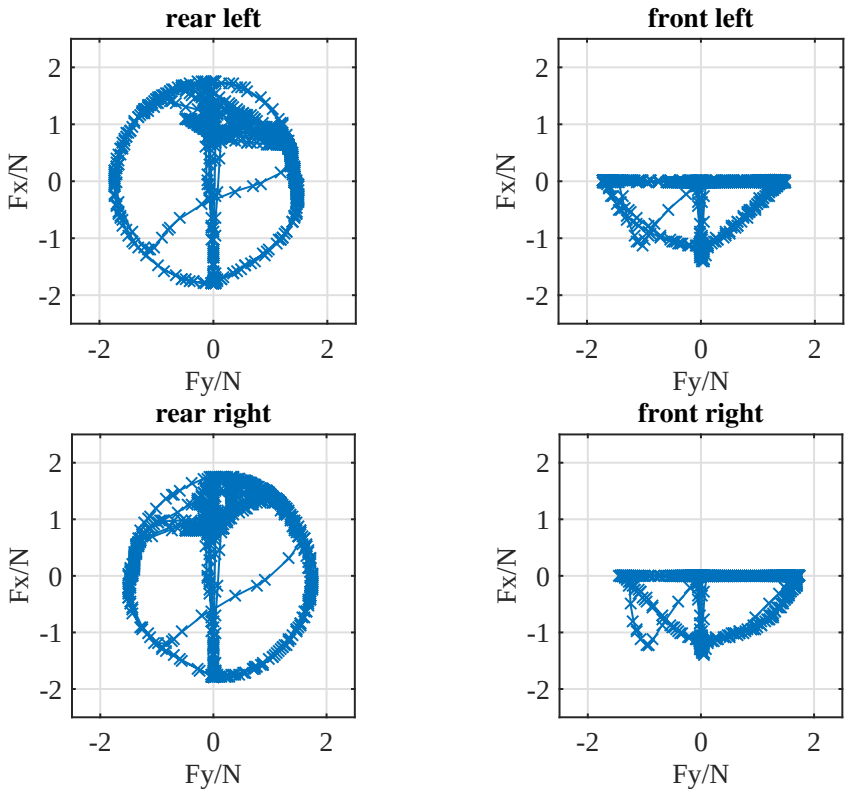

Figure 3.34: Adherence ellipses for the slip model.

3.4.3 Imola

The *Autodromo Internazionale Enzo e Dino Ferrari* is a complex track both for the real pilots and for the ideal pilot simulated by the optimal control problem; consequently high time for the simulation are needed also setting a previous solution saved, with slightly different parameters, as the initial guess for the problem. In this case the first solution has been found without employing the lift forces, with a duration of almost 6000 s, while the solution adopted for the analysis is reached starting from the previous results and including the lift area coefficient $C_L A = 2.8$ m^2, split in 70% at the rear axle and 30% at the front. Both the first and second solutions implement a drag area $C_D A = 0.8$ m^2. This simulation moreover presents an important difference respect to Adria and Monza: the lap time obtained with the slip-slip model is slightly higher than the best performance achieved with the basic vehicle; the high speed of variation of the car dynamics is due to a series of curves that does not allow the establishment of an almost *steady state* condition during the corners. This behavior determines a significant drawback for the slip-slip model, that presents some difficulties to reach the best adherence condition limiting the load transfer. This strategy, in fact, allowed an advantage for the previous simulations analyzed while in these conditions is no more effective in most of the curves.

Imola	**Slip-Slip**	**Basic 2D**
Lap Time [s]	100.200	100.087
CPU Time [s]	2837	490
Penalties [s]	0.191	0.104
Prev. Sol.	yes	yes

Table 3.8: Simulation comparison between *basic* and *slip-slip* model.

In fig. 3.36 is represented the parameter Δn, or rather the difference of the curvilinear coordinate n between the *slip-slip* model and the *basic* one. This parameter records significant differences in particular at $s = 750 \div 900$ m, at $s = 1000 \div 1250$ m and at $s = 2900 \div 3400$ m, that correspond respectively to the corners *Variante Tamburello*, the entrance of *Variante Villeneuve* and the *Variante Alta*. These curves are magnified in fig. 3.35, which allows to underline the main visible differences.
The *Variante Tamburello* is defined by a sequence of three curves: a chicane and a fast curve travelled in acceleration; the main difference between the models is not related to the entrance and exit maneuvers, but is connected to the part of the track that prepares the third corner. The basic car adopts a greater variation of trajectory, using the external curbs at the exit of the chicane and then steering oppositely to prepare the entrance of the third turn, but without using the whole road width in this second maneuver. The slip vehicle, instead, adopts an opposite strategy privileging the entrance of the third corner and suffering in terms of speed at the exit of the chicane; this choice can be justified considering that the

slip model makes use of a more gradual maneuver that limits the load transfers and consequently reduces the decrease of the adherence coefficients.
The analysis of the rectilinear before the *Variante Villeneuve*[3] permits to show another important maneuver that can be captured with the slip-slip model: the ideal driver in fact chooses a trajectory that is initially more distant to the border reached in the exit of the previous corner; just before the new corner (on the left) a steering action drives the car to the external curb, preparing the entrance maneuver, while the consequent opposite steering action leads the vehicle into the corner. Therefore the ideal driver starts the entrance of the corner steering oppositely to the curve and then steering in the same direction of the curve: this choice allows to limit the lateral load transfer in the curve and allows a proper use of the slip quantities, accentuating the oversteering behavior of the vehicle. This behavior is not shown in the basic model, in which the adherence is not affected by the load transfer; the vehicle, in fact, remains near the border from the exit of the previous curve to the entrance of the following one.
Considering the *Variante Alta* similar conclusions can be drawn: the slip vehicle anticipates the curve entrance for a more gradual maneuver, while in the straight before the corner it privileges a trajectory that uses the whole road width to induce an opposite lateral load transfer and reduce the effect of load increment on the adherence limits.

No particular surprises are reported by the slip quantities in fig. 3.37. It should be noticed that before most of the curves the *lateral slip angle* λ assumes an opposite sign respect to the values calculated during the corner, while in the curve the lateral slip quantities are almost identical in all the wheels. This is related to the opposite steering maneuver described at the *Variante Villeneuve*. The front longitudinal slips, moreover, are lower than the rear value in traction because of the load transfer: in fact higher values are requested at the rear tires, owing to the increase of rear loads, to obtain enough longitudinal force; during braking it is not possible to highlight the opposite behavior because most of the braking action is due to the front wheels in which, nevertheless, the incremented load reduces the slope of the tyre force function; the rear wheels, instead, are unloaded and, despite of the fact that less braking force is available at the contact point, the adherence limits are lower.

The loads profile highlights in fig. 3.38 the complexity of this track, with an evident combination of longitudinal and lateral load transfer. The normal loads curves, in fact, are really entangled and the maximum values are higher than the previous simulations on different circuits, although the minimum values are also higher due to the implementation of the lift forces in the vehicle dynamics equation. As for the longitudinal load transfer the main differences between the slip model and the basic car are located $s = 1250 \div 1500$ m, $s = 1600 \div 1750$ m, $s = 2600 \div 2900$ m, $s = 3250 \div 3400$ m and $s = 4000 \div 4300$ m. These intervals correspond respectively to the *Variante Villeneuve*, the *Tosa*, the *Acque Minerali*, the *Variante Alta* and the *Rivazza*: this means that in most of the curves the difference is significant. In all these corners the behavior is similar

[3]note that the image is rotated of 90° to the right for space optimization; thus the corner is travelled from right to left.

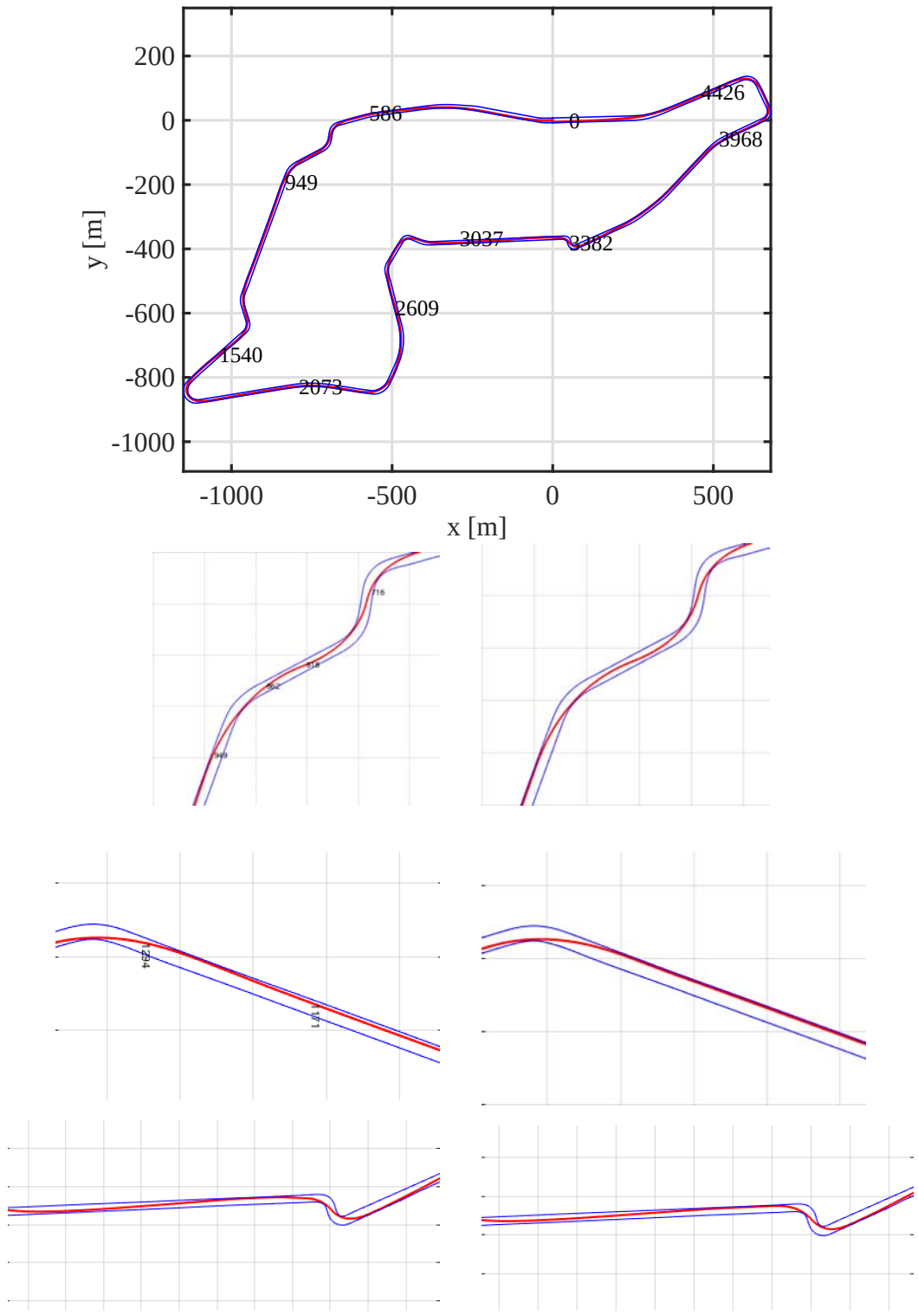

Figure 3.35: Track reconstruction and trajectory (top), *Variante Tamburello*, *Variante Villeneuve* and *Variante Alta* for *slip-slip model* (left) and *basic model* (right).

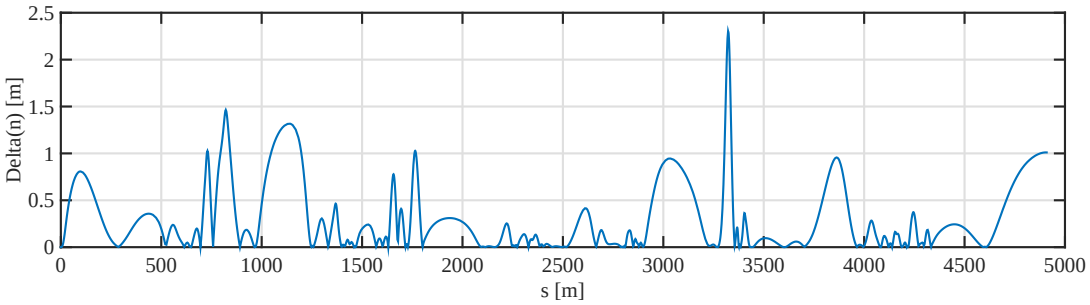

Figure 3.36: Absolute value of the difference between the curvilinear coordinate n of the *basic* and *slip model*: $\Delta n = |n_b - n_{ss}|$.

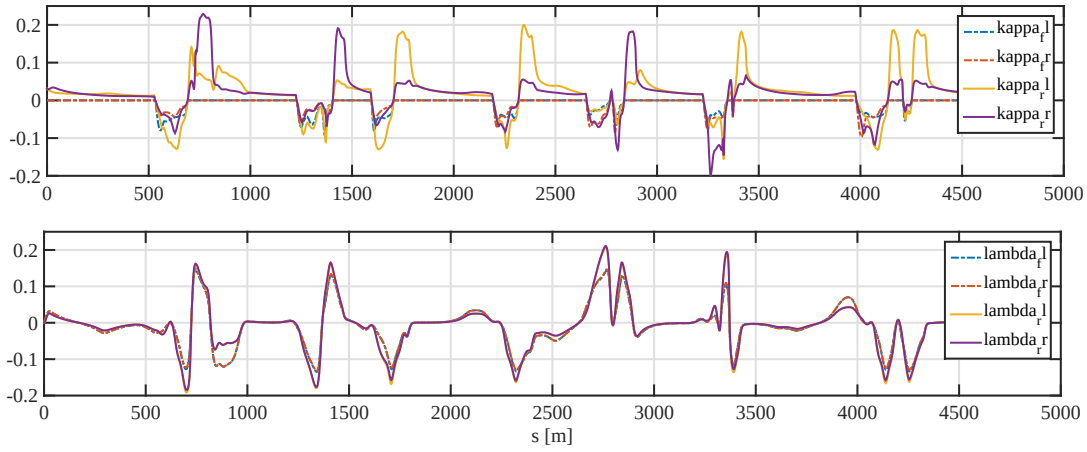

Figure 3.37: Longitudinal κ and lateral λ slip values for the *slip-slip* model.

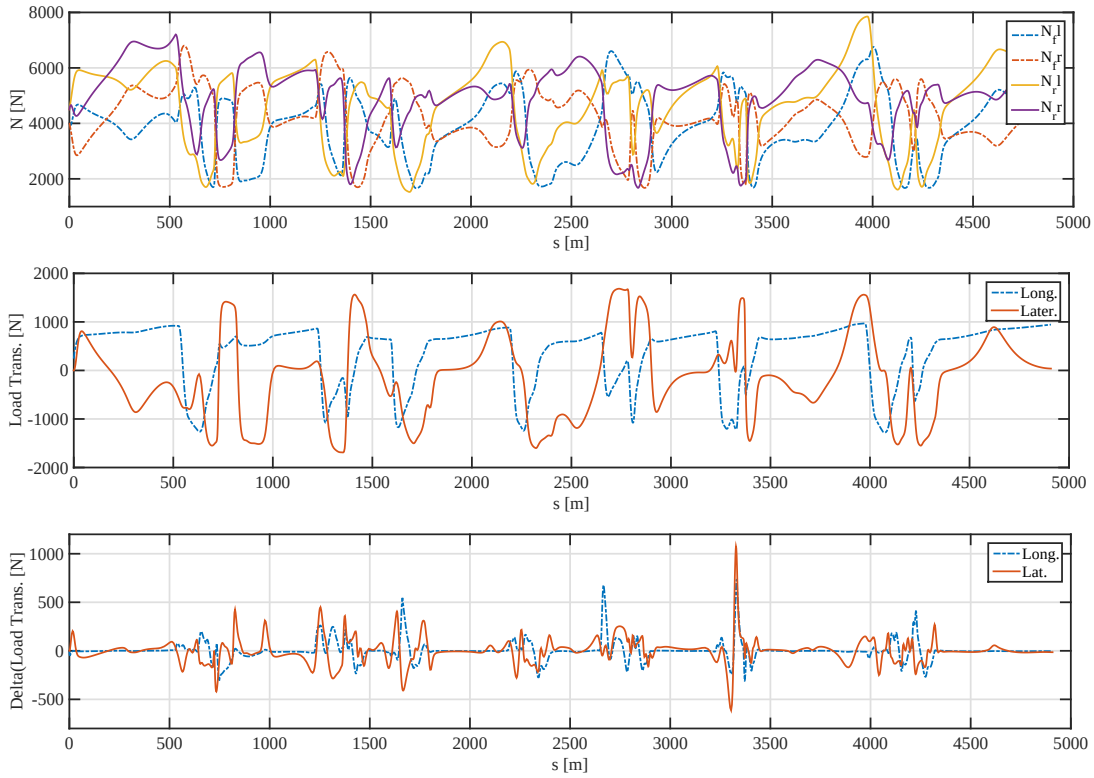

Figure 3.38: Normal loads (top) and loads transfer (middle) for the *slip-slip* model and difference between slip and basic model, $\Delta(\Delta N) = \Delta N_b - \Delta N_{ss}$ (bottom)..

and the slip vehicle maintains lower values of the longitudinal load transfer both in braking and in traction. A different behavior can be noticed at the *Variante Alta* corner, where the load transfer is initially lower for the slip model until, during the braking phase, is reached a higher value than the basic model; this consideration permits to deduce that the vehicle delays the braking action and starts earlier the acceleration. Correspondently to the straight before the *Variante Villeneuve* it is possible to notice a small positive peak for the lateral load transfer, which underlines the opposite steering maneuver adopted by the slip model; in this condition a higher value for the lateral load transfer is registered in the slip model, while, consequently, in the middle of the curve is achieved a lower load transfer, that determines an advantage for the adherence limits. A major peak is calculated at the *Variante Alta*, where the slip model registers initially higher values for the lateral load transfer, although lower values are determined in the second part of the corner: the slip-slip vehicle anticipates the cornering maneuver, in order to travel a more gradual trajectory.

In fig. 3.39 is represented the total longitudinal force normalized by the weight force of the car. During the *Tosa* curve ($s \approx 1600$ m) the slip vehicle uses more longitudinal force with a lower steering angle, thanks to the oversteering characteristic: this behavior can be shown in the *slip-slip* model only, because the adoption of constant values for the tyre parameters, that are assumed equal for the front and rear wheels, generates a constant neutral behavior of the vehicle;

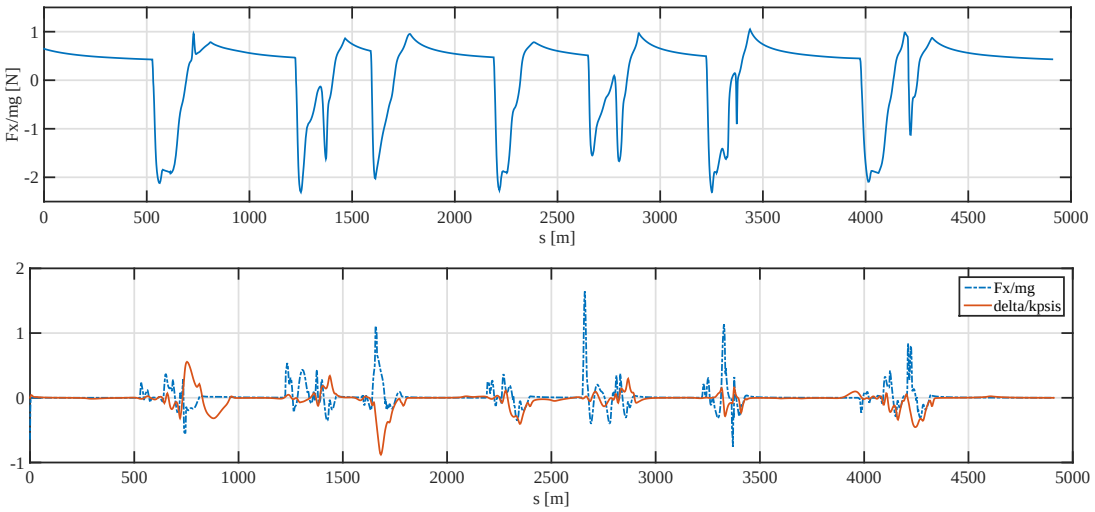

Figure 3.39: Total longitudinal force profile for the slip model, normalized by the weight force (top), and comparison between slip and basic model: $\Delta(Fx/mg) = (Fx/mg)_b - (Fx/mg)_{ss}$ (bottom).

on the contrary the variation of the tyre properties with the normal loads permits to change the behavior, that depends on the static load distribution and on the load transfer. The major peak at the *Acque Minerali* demonstrates that the slip car anticipates the cornering maneuver while at the *Variante Alta* the driver anticipates the braking action and exploits more traction at the exit.

The velocity profiles (fig. 3.40) remark the considerations expressed: the slip vehicle enters slower in the curves in order to exploit a better traction and obtain higher speeds at the exit of the corner. These maneuvers, nevertheless, do not permit an overall time advantage for the slip model.

The adherence ellipses of fig. 3.41 show an almost complete usage of the forces available and the "curls" of these curves are particularly evident in the front wheels diagrams. In spite of that it must be underlined that the real-right tyre does not present a complete usage of the adherence because at high values of positive F_x, the negative F_y are not fully utilized; in other words during negative curvature corners and in traction conditions, the external tyre is not completely exploited.

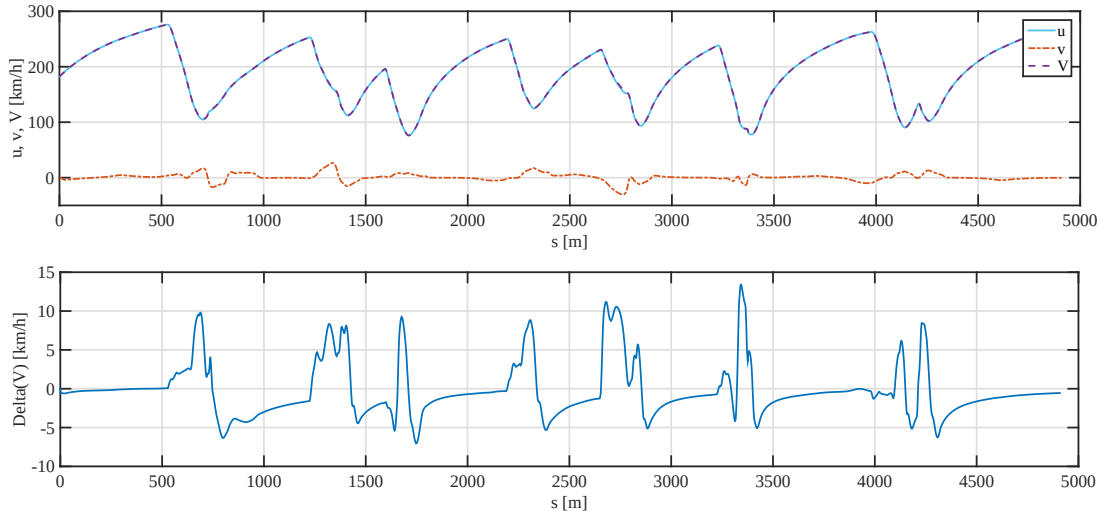

Figure 3.40: Velocity profiles for the slip model (top) and comparison between slip and basic model: $\Delta V = V_b - V_{ss}$ (bottom).

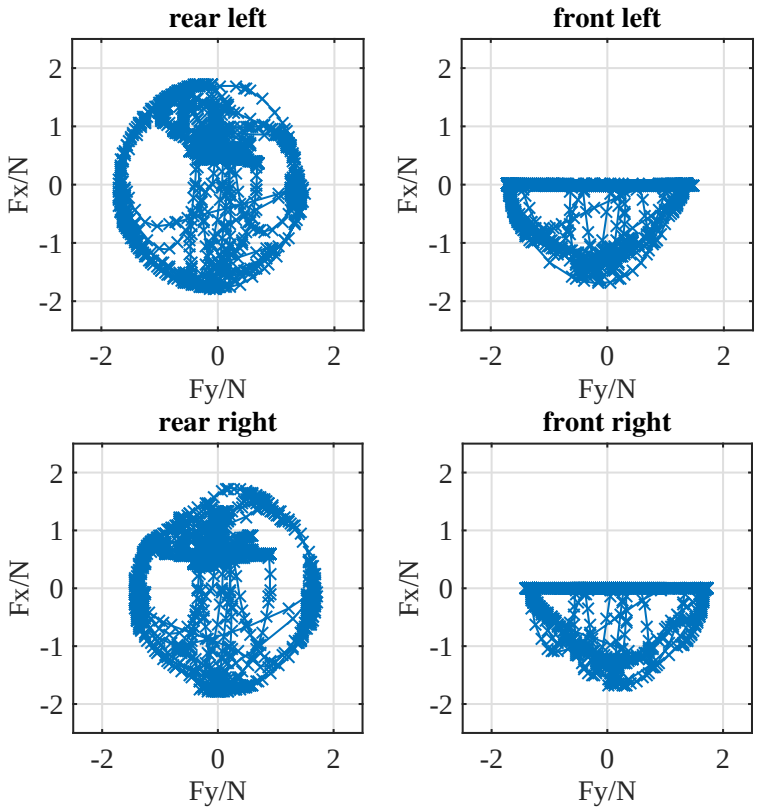

Figure 3.41: Adherence ellipses for the slip model.

Chapter 4

Parametric Analysis

4.1 Introduction

Different simulations can be employed in order to study the effect of the main parameters on the vehicle model and to identify the best and most effective characteristics that allow an improvement in the lap time performance. For this analysis the *slip-slip* model will be adopted: only with this choice, in fact, it is possible to capture the peculiar behaviors related to the usage of a complete formulation of the slip quantities and the tyre forces combination.
The parameters that will be taken in consideration are the *roll stiffness ratio* $\xi = K_{\phi f}/K_{\phi}$, the longitudinal position of the CoM (b) and the CoM height h, the wheelbase w, the *track* of the vehicle or vehicle width T, the *yaw inertia* I_z, the *viscosity coefficient* of the differential k_d and the aerodynamic coefficients for drag ($C_D A$) and lift ($C_L A$). For each of these cases of study all the parameters that are not the object of the analysis are set at the same values, in order to obtain comparable results; in particular, with clear exception of the aerodynamics analysis, the drag area coefficient $C_D A$ is assumed of 0.65 m^2 and no lift forces are considered.
GPOPS provides a built-in parametric optimization program, that attempts to find the absolute minimum of the lap time in function of the parameter analyzed; to validate the real behavior of this function, a set of values will be simulated with the usual optimal control solution and changing the parameters in each simulation: this procedure is employed to avoid the achievement of relative minimums and to draw some considerations on the form of the lap time curve, varying the parameter of interest. The set of parameter values is chosen with reference to an average value, that corresponds to a realistic vehicle characteristic, incremented or reduced of the 20%. Furthermore for each analysis the optimal parameter results will be compared to the simulations in which are implemented lower and higher values of the parameter respectively, in order to stress the effect on the lap time.
The track chosen for each simulation is the *Adria International Raceway*; this circuit was used for the *basic* model validation and, moreover, is the location of most of the real car tests.

4.2 Roll Stiffness Ratio

The roll stiffness ratio $\xi = K_{\phi f}/K_{\phi}$ represents the ratio between the front roll stiffness and the total roll stiffness of the vehicle; this parameter takes an important role in the determination of the lateral load transfer and in its distribution in each axle of the car (see eq. (2.22)). If all the roll stiffness concerns the front axle only, the parameter assumes the value of $\xi = 1$, while if the front axle makes no contribute for the roll stiffness, and therefore all the stiffness concerns the rear axle, is verified the equation $\xi = 0$.
The load transfer is peculiar for the determination of the adherence limits and for the capability of transmitting the tyre forces to the ground; high values of the front roll stiffness causes elevated lateral load transfer at the front axle, while small $K_{\phi f}$ are related to high load transfer at the rear axle.
Table 4.1 and fig. 4.1 show the variation of lap time obtained simulating the system with different values of $\xi \in [0, 1]$: it should be noticed that a minimum is found for $\xi = 0.87$ and the other simulated points confirm this result. Excessively elevated values of the roll stiffness at the front or at the rear of the vehicle determine high lateral load transfer which cause a reduction of the friction limits of the external tires, while the internal ones are subjected to significantly lower loads and can express lower forces; the optimum value is identified at high front roll stiffness: therefore the front axle undergoes the effect of high lateral load transfer while the rear, thanks to the rolling action, employs low lateral load transfer and a better force transmission to the ground is granted; this represent an advantage during the exit of the corners and in the entrance phases, because the traction and braking actions are more effective using the rear tires.

Parametric Opt. Adria	$\overline{\xi} \cdot 0.8$	$\overline{\xi}$	$\overline{\xi} \cdot 1.2$	ξ_{opt}	$\overline{\xi} \cdot 1.8$
ξ	0.424	0.53	0.636	0.869	0.954
Lap Time [s]	75.996	75.211	74.569	73.852	74.029
CPU Time [s]	748	996	794	1782	1075
Penalties [s]	0.105	0.138	0.154	0.158	0.175
Previous Solution Guess	yes	yes	yes	yes	yes

Table 4.1: Simulation parameters used for roll stiffness ratio optimization.

In this case are evaluated the differences comparing the optimal system to the systems considered with a lower and a higher value of $\xi_{low} = 0.464$ and $\xi_{high} = 0.954$ respectively. As for the orthogonal coordinate n (fig. 4.2), the main differences of trajectory respect to the lower value can be found at $s \approx 400 \div 500$, $s \approx 1000 \div 1100$, $s \approx 1400 \div 1500$ and $s \approx 2200 \div 2400$. In the first corner the optimal vehicle uses a trajectory close to the internal curb, traveling the lowest distance, while for the lower value of ξ the car adopts a larger trajectory because the load transfer is higher at the rear axle and must be reduced in order to start the acceleration phase at the exit. Also the entrance phase is different because

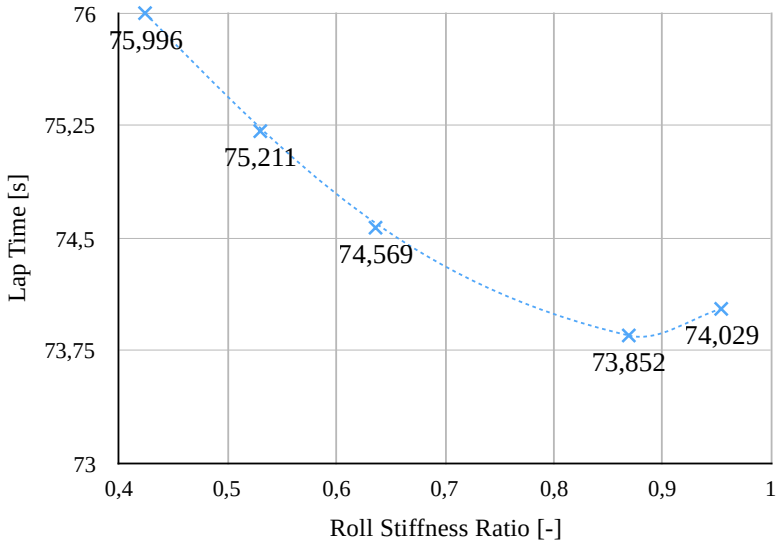

Figure 4.1: Variation of the lap time in terms of roll stiffness ratio ξ.

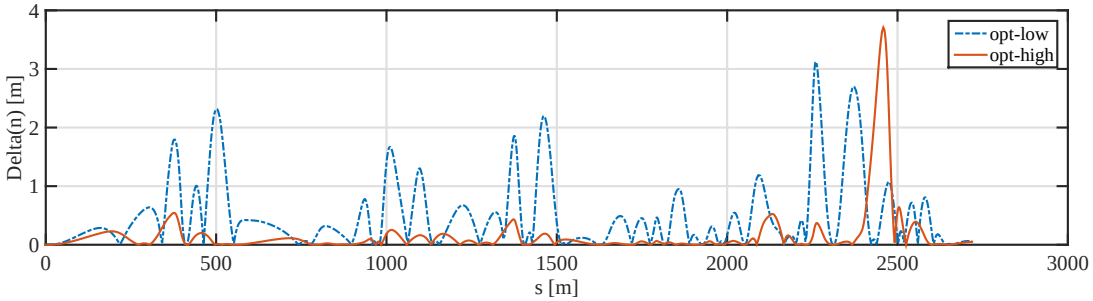

Figure 4.2: Absolute value of the difference between the curvilinear coordinate n for lower, optimal and higher value of ξ: $\Delta n = |n_{opt} - \xi_{low}|$ and $\Delta n = |n_{opt} - n_{high}|$.

the optimal vehicle is capable of anticipating the steering and following the internal profile of the corner for a shorter distance traveled; on the contrary with ξ_{low} the car needs to follow a more gradual trajectory and consequently reduce the lateral load transfer. The same conclusion can be drawn considering the second and third corner, in which the optimal parameter allows to reduce the distance to travel, with sharper trajectories. An opposite strategy, instead, is adopted for the second-last corner: in this part of the track there is a series of nearly located curves and no long straights separate the corners. In this kind of path a high value of the lateral load transfer represents an important drawback while a more balanced distribution of the roll stiffness is an advantage in order to front with the sequence of corners; the vehicle with ξ_{opt} in fact needs to follow larger and more rounded trajectories before, during and after the second-last curve because, in that way, it is possible to limit the excessive front load transfer.

The load transfer profile obtained using the optimal parameter (fig. 4.4) is significantly different to the previous results; in particular the greatest differences are registered respect to the model with ξ_{low}, both for the longitudinal and for the

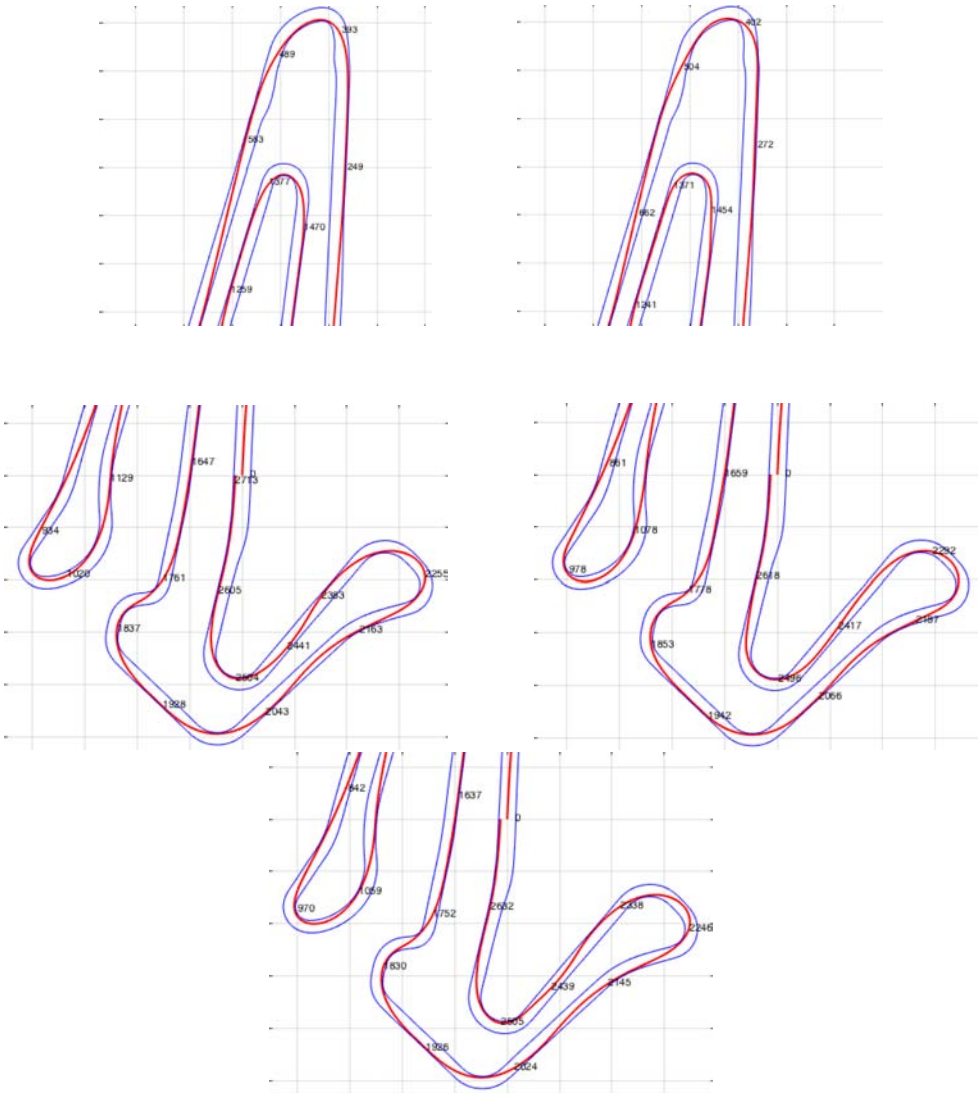

Figure 4.3: Magnified views of the corners for optimal (left) and lower value (right) of the parameter; at the bottom is reported the trajectory for the higher value of ξ.

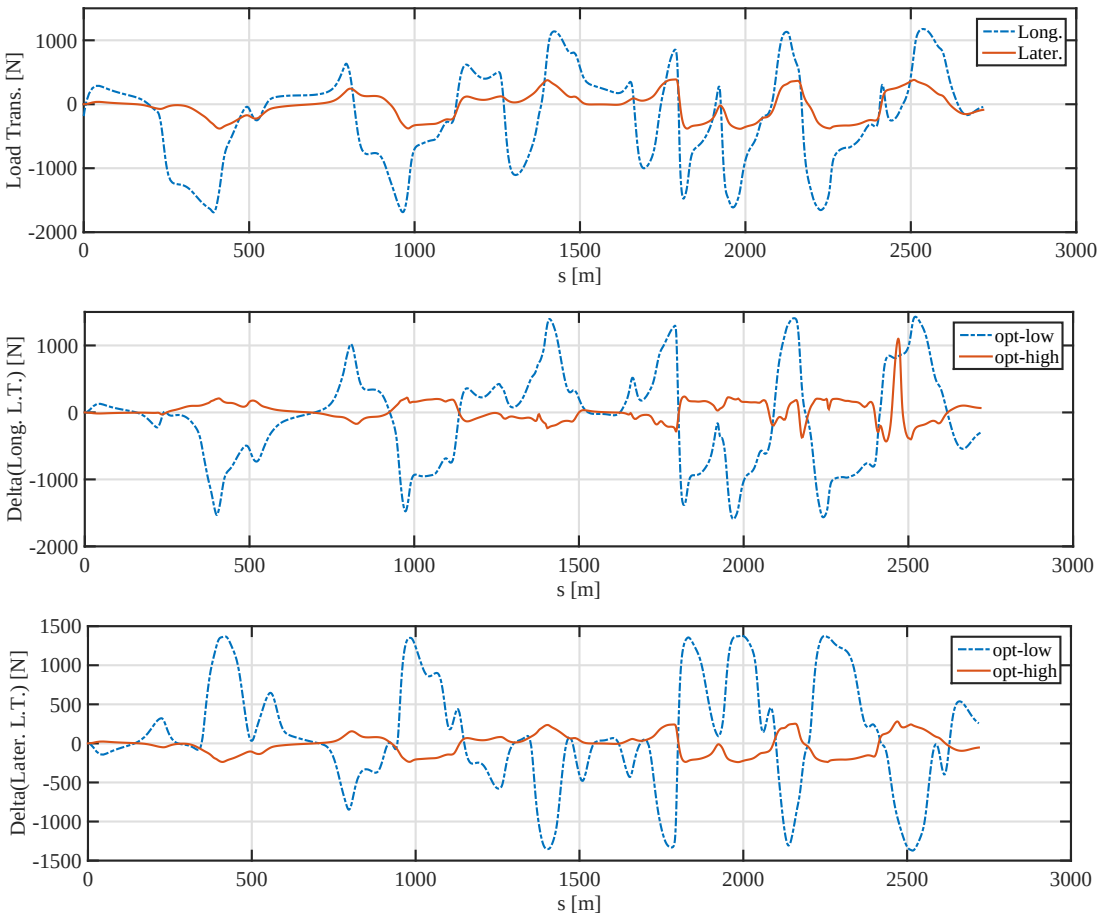

Figure 4.4: Load transfer for ξ_{opt} (top) and difference between the longitudinal (mid) and lateral (bottom) load transfer for lower, optimum and higher value of ξ: $\Delta(\Delta N) = \Delta N_{opt} - \Delta N_{low}$ and $\Delta(\Delta N) = \Delta N_{opt} - \Delta N_{high}$.

lateral load transfer. The differences are calculated in analogy with the previous simulations: $\Delta N_{lon} = N_{rr} - N_{fr}$ and $\Delta N_{lon} = N_{rl} - N_{rr}$: it should be noticed that the lateral value is calculated for the rear axle, or rather the axle in which the roll stiffness is lower for ξ_{opt} and ξ_{high}.
The longitudinal load transfer is higher for ξ_{opt} in braking and in traction condition because these phases are delayed and anticipated respectively and shorter distances are travelled. On the contrary the rear lateral transfer is lower for all the corners because the roll stiffness is lower. The model with the highest value of ξ considered, instead, presents higher values for the longitudinal and lower value for the lateral load transfer than the vehicle with ξ_{opt}, because a higher roll stiffness is provided at the front. In this case the delay due to the poor performance in the second part of the track is more significative than the advantage obtained on the fist part of the track, where a high value for $K_{\phi f}$ determines an improved maneuverability.

The total longitudinal force profile of the optimized vehicle (fig. 4.5) differs from the simulation with ξ_{low} in a similar way for the first three corners, while in the second part of the track the dynamics becomes more complex and no repeated schemes can be identified. For the first corners, the model with ξ_{opt} enters delaying

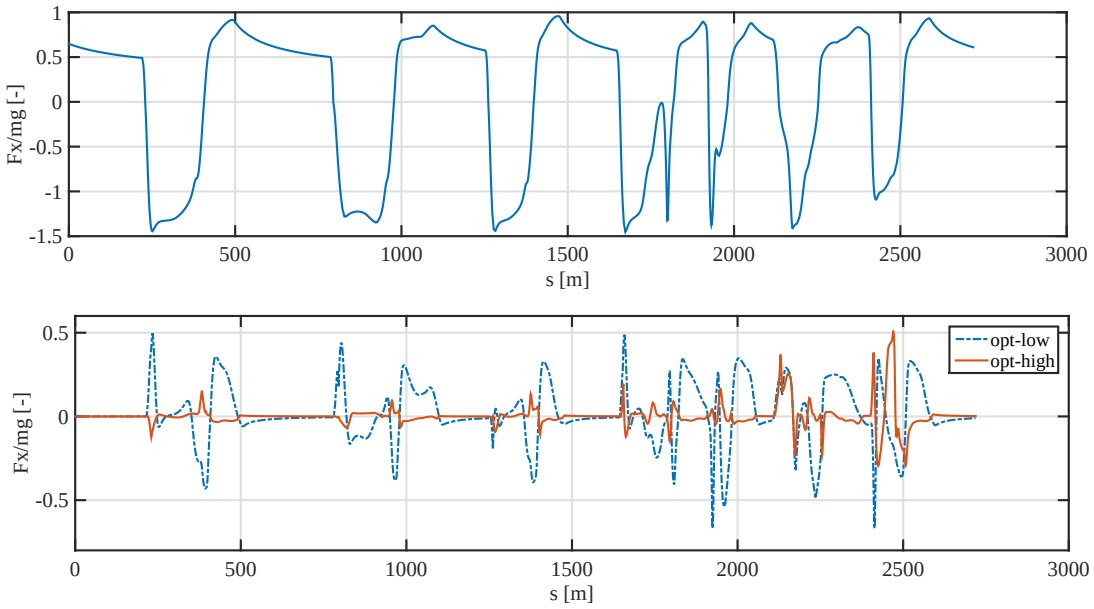

Figure 4.5: Longitudinal force for ξ_{opt} (top) and difference between the longitudinal force for lower, optimum and higher value of ξ: $\Delta(F_x/mg) = (F_x/mg)_{opt} - (F_x/mg)_{low}$ and $\Delta(F_x/mg) = (F_x/mg)_{opt} - (F_x/mg)_{high}$.

the braking action and accentuating the braking force, thanks to the lower load transfer at the rear axle; at the same way also the first part of the acceleration in the exit phase is performed with more longitudinal force. Employing ξ_{high} the vehicle makes more evident the behavior obtained with the optimal parameter in the first half of the track: braking delayed, stronger braking action and more powerful acceleration; in the second part of the track the dynamics becomes complex and more difficult to follow.
The speed profile of fig. 4.6 shows the same concept: the optimal car enters faster in the corner, becomes slower during the corner because of the sharper trajectory and exits faster; in the second part of the track, although for ξ_{opt} the vehicle maintains an overall higher speed, the slower phases are more frequent and the profiles become less repeatable: the vehicle in fact adopts more rounded trajectories, traveling at higher speed but using a longer distance. Respect to ξ_{high}, instead, the increment of $K_{\phi f}$ accentuates further the behavior described for ξ_{opt}, although in the second part of the track the vehicle becomes slower.

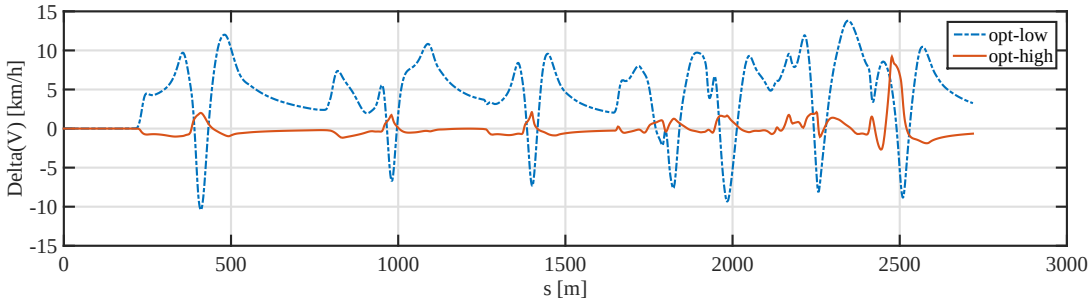

Figure 4.6: Absolute value of the difference between the speed profile for lower, optimum and higher value of ξ: $\Delta V = V_{opt} - V_{low}$ and $\Delta V = V_{opt} - V_{high}$.

4.3 CoM Position

The position of the centre of mass of the vehicle (CoM) determines most of the dynamic aspects connected to handling and maneuverability; in fact the static loads distribution and the stability characteristics depend on the CoM longitudinal positioning, while the vertical position is related both to the lateral and longitudinal load transfer. In this section all these aspects will be investigated with reference to the distance from the CoM to the rear axle (b) and the CoM height from the ground (h). Moreover a few considerations will be underlined focusing the attention on the vehicle stability and its importance for the determination of the dynamic behavior.

4.3.1 Longitudinal Position

The analysis of b is focused on the realistic range of $b \in [1, 2.5]$ m and two different cases are studied: the usual vehicle without lift downforce and the effect of the lift forces to the CoM position.
In table 4.2 and in fig. 4.7 are summarized the results of the simulations with different values of b, without considering the lift forces and for a constant value of the wheelbase w; due to numerical difficulties no simulation could have been performed under b_{opt}, probably because of the instability of the model in these conditions (see sec. 4.3.2). Therefore it can be assumed that reducing the distance between the CoM and the rear axle, the vehicle is capable of better lap time performances. This behavior is mainly due to the more significant *oversteering* behavior obtained reducing the parameter b: in these condition the ideal driver can control the handling capabilities using the throttle properly to induce a more effective steering action, in order to reduce the distance to travel.

In the first, third and last corner are registered the greatest differences in terms of n between the model that uses b_{opt} and the one with a higher value $b_{high} = 1.842$ m (fig. 4.8). As it can be seen in fig. 4.9, the optimal model adopts a sharper trajectory in the first and third corner of the track and travels a shorter

Parametric Opt. Adria	$\overline{\mathbf{b}} \cdot \mathbf{0.8}$	$\overline{\mathbf{b}}$	$\overline{\mathbf{b}} \cdot \mathbf{1.2}$	$\mathbf{b_{opt}}$
b [m]	1.228	1.535	1.842	1.112
Lap Time [s]	73.159	75.211	78.976	72.774
CPU Time [s]	738	996	1038	1934
Penalties [s]	0.143	0.138	0.133	0.151
Previous Solution Guess	yes	yes	yes	yes

Table 4.2: Simulation parameters used for CoM longitudinal position optimization b (without lift).

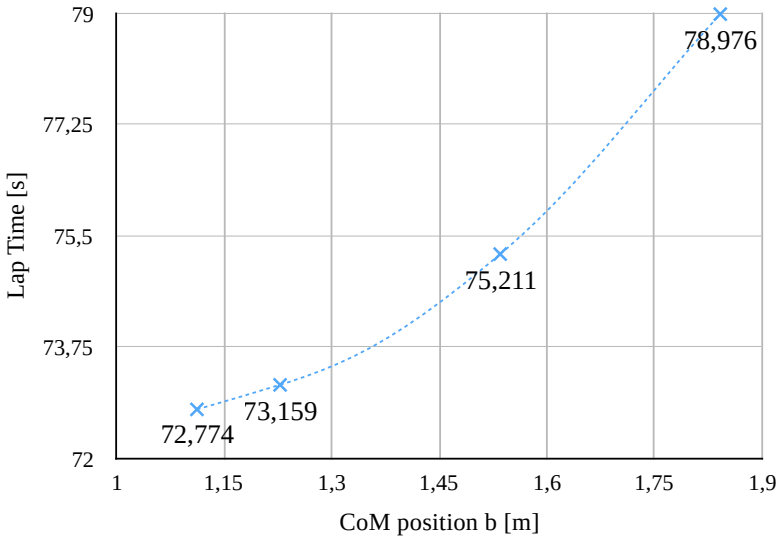

Figure 4.7: Variation of the lap time in terms of CoM longitudinal position b.

distance; on the contrary the model with b_{high} needs to use the whole road width in order to minimize the lap time, because it is less maneuverable into the corners. In the last curve the behavior is similar and the best lap time is obtained simply reducing the distance traveled and avoiding the change of direction to prepare the corner; this is possible because the driver is able to control the vehicle instability, taking advantage of the possibility of changing direction faster.

Regarding the load transfer (fig. 4.10) the longitudinal CoM position affects the static load distribution between the front and rear wheels; hence the longitudinal load transfer is incremented in the whole circuit because the weight is now located towards the rear part of the car. Moreover it should be noticed that a similar scheme for $\Delta(\Delta N) = \Delta N_{opt} - \Delta N_{high}$ is repeated for the first part of the track: approaching the corner the load transfer increases because the optimal model delays the braking action; then $\Delta(\Delta N)$ is reduced because of the effective braking action, which is due to the higher friction coefficients at the front tires. During the following acceleration the difference newly increases because the optimal car anticipates this phase. In the second part of the track the sequence of curves make more difficult the adoption of this strategy and the load transfer profile becomes less regular. The lateral transfer profile is oscillating but in most of the curves the vehicle which adopts the optimal parameter achieves higher values, because of the

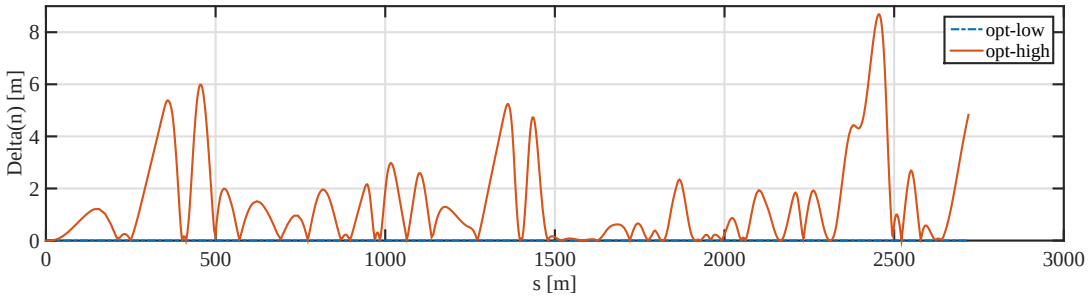

Figure 4.8: Absolute value of the difference between the CoM longitudinal position b for lower (optimum) and higher value of b: $\Delta n = |n_{opt} - n_{high}|$.

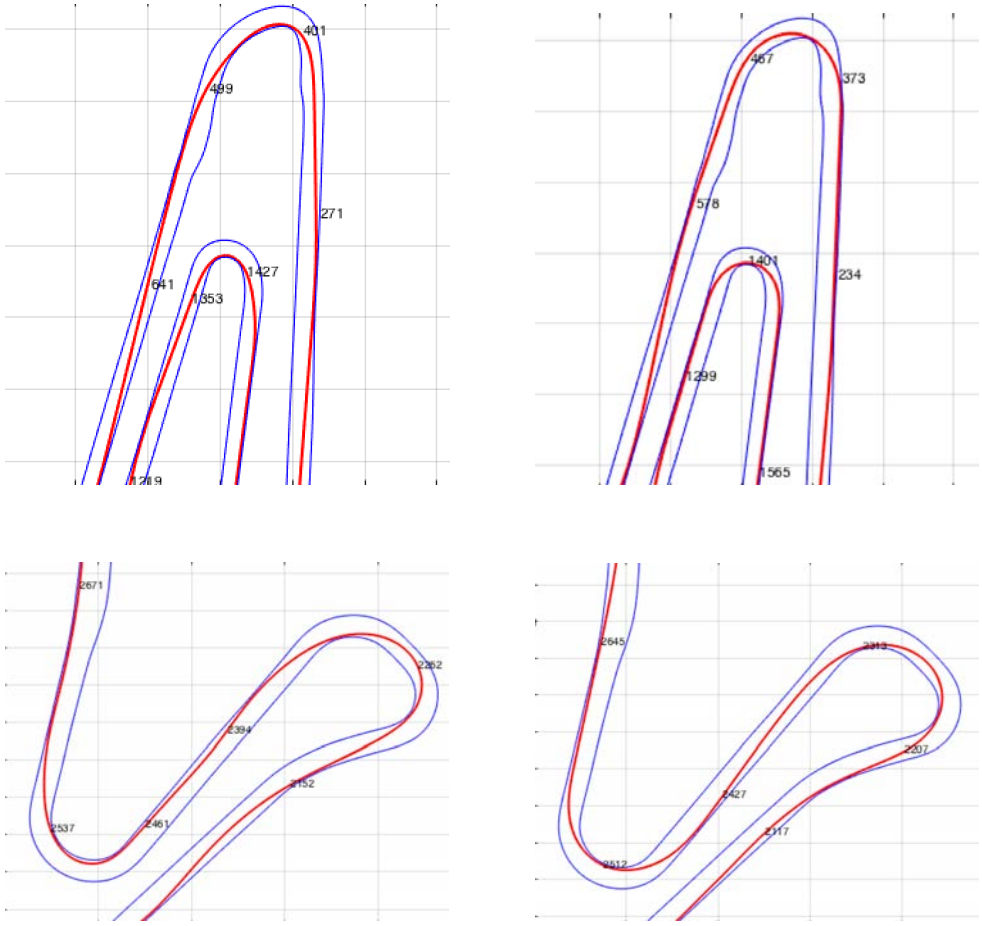

Figure 4.9: Magnified views of the first, third, last and second-last curves for optimal (left) and higher value (right) of the parameter.

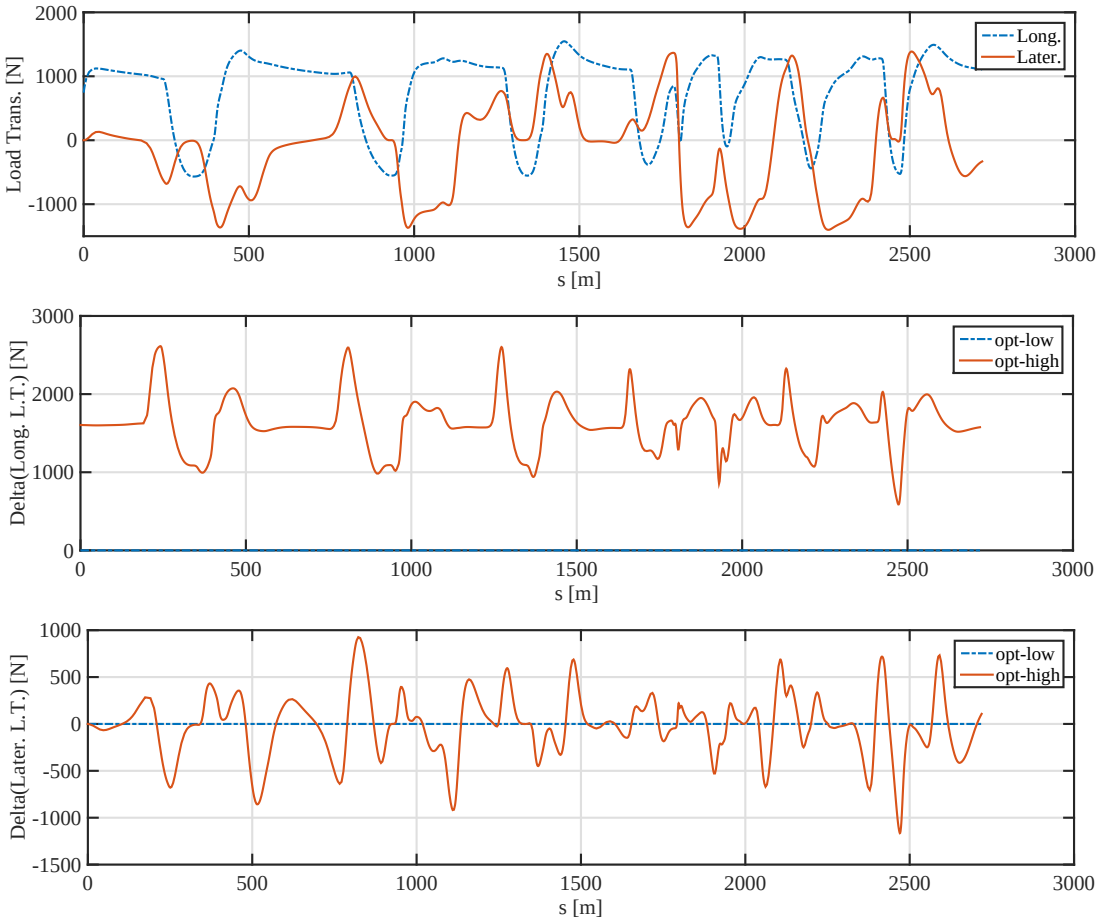

Figure 4.10: Load transfer for b_{opt} (top) and difference between the longitudinal (mid) and lateral (bottom) load transfer for lower (optimum) and higher value of b: $\Delta(\Delta N) = \Delta N_{opt} - \Delta N_{high}$.

sharper trajectories.

In fig. 4.11 is provided the study of the total longitudinal force applied to the contact points; it can be observed that the optimal vehicle delays the braking phase and, as concluded previously, is capable of a more effective braking action and a better traction at the curve exit: the vehicle exploits its oversteering capabilities and the load distribution to reach the best performance.
The speed profile of fig. 4.12 confirms that the car enters faster in the corner, decelerates strongly and increases the speed during traction.

In table 4.3 and fig. 4.13 are provided the simulation results obtained varying b and simultaneously implementing the lift forces. In this analysis are set the parameters $C_{Lf}A = 0.72$ m^2, $C_{Lr}A = 1.68$ m^2 and $C_DA = 0.8$ m^2. The overall profile is the same: lower b determine an advantage in terms of lap time; nevertheless the optimal value passes from $b = 1.112$ m, without lift forces, to $b = 1.128$ m, considering the lift. This result is not surprising because the rear wing provides a good deal of the utter normal load and there is a lower need to position the CoM near the rear axle; moreover it must be considered that only a little increment of b is obtained because the incremented load on the rear wheels determines an

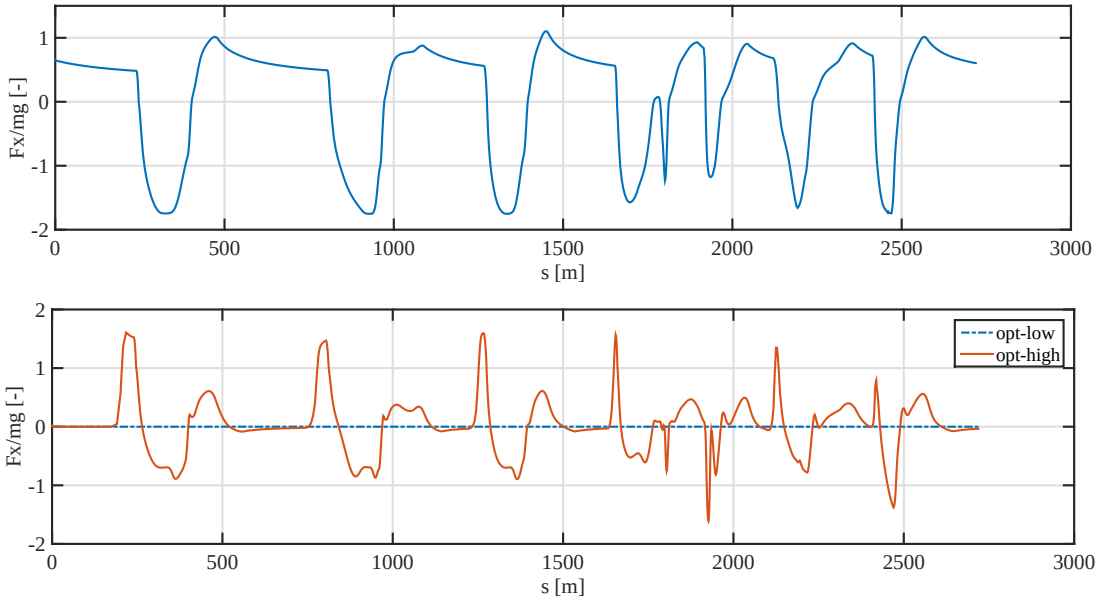

Figure 4.11: Longitudinal force for b_{opt} (top) and difference between the longitudinal force for lower (optimum) and higher value of b: $\Delta(F_x/mg) = (F_x/mg)_{opt} - (F_x/mg)_{high}$.

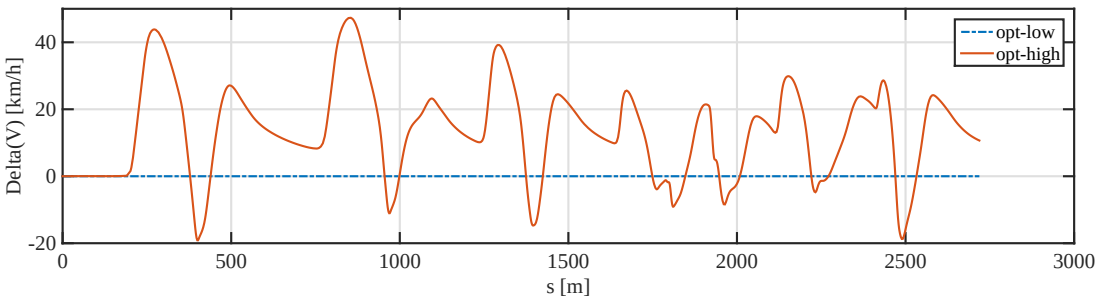

Figure 4.12: Difference between the speed profile for lower (optimum) and higher value of b: $\Delta V = V_{opt} - V_{high}$.

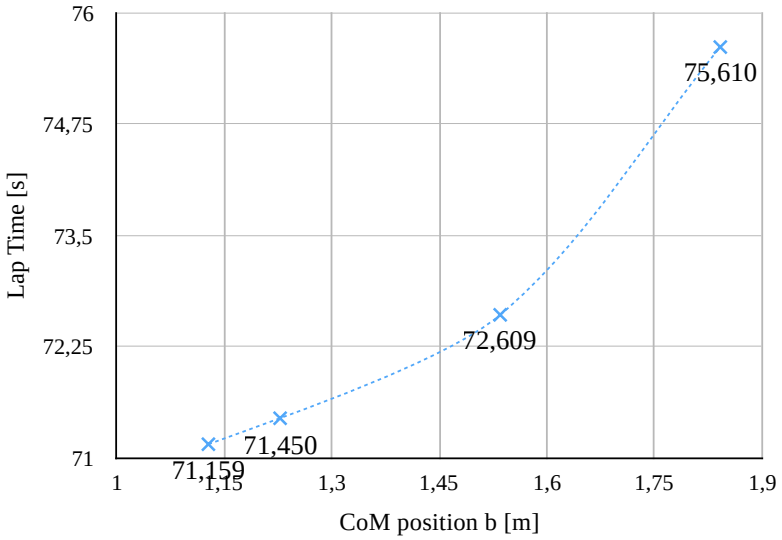

Figure 4.13: Variation of the lap time in terms of CoM longitudinal position b with lift.

increase of the rear cornering stiffness and a consequent reduction of the *over-steering* behavior, that have to be compensated by a low value of b, or rather a backward position of the CoM.

Parametric Opt. Adria	$\overline{\mathbf{b}} \cdot \mathbf{0.8}$	$\overline{\mathbf{b}}$	$\overline{\mathbf{b}} \cdot \mathbf{1.2}$	$\mathbf{b_{opt}}$
b [m]	1.228	1.535	1.842	1.128
Lap Time [s]	71.450	72.609	75.610	71.159
CPU Time [s]	4964	1565	2139	1135
Penalties [s]	0.143	0.135	0.178	0.125
Previous Solution Guess	yes	yes	yes	yes

Table 4.3: Simulation parameters used for CoM longitudinal position optimization b (with lift).

4.3.2 Stability

Considering now the *cornering stiffness* of the tires, a value for static conditions can be obtained from:

$$C_f = K_{yf}\, N_f = K_{yf}\, mg\, \frac{b}{w}, \qquad C_r = K_{yr}\, N_r = K_{yr}\, mg\, \frac{a}{w}; \tag{4.1}$$

K_{yf} and K_{yr} are calculated from eq. (2.92).
Applying the *Routh-Hurwitz criterium* to the *single-track* model, the stability of the vehicle is then determined; it is possible to distinguish three different conditions that correspond to three different behaviors:

$$\begin{cases} C_r\, b - C_f\, a > 0, & \text{understeering} \\ C_r\, b - C_f\, a = 0, & \text{neutral} \\ C_r\, b - C_f\, a < 0, & \text{oversteering.} \end{cases} \tag{4.2}$$

The vehicle is characterized by an *understeering* behavior if the rear has a greater roadholding than the front and is *oversteering* if the front has a better roadholding than the rear; the vehicle is *neutral* if neither front nor rear prevale in terms of roadholding behavior. For *oversteering* vehicles the dynamic system admits real and distinct eigenvalues, that become negative when the car reaches the *critical speed* u_{cr}, for which the instability occurs. The expression for u_{cr} derives from the *Routh-Hurwitz criterium*:

$$u_{cr} = \sqrt{\frac{C_f\, C_r\, w^2}{m\,(C_f\, a - C_r\, b)}}; \tag{4.3}$$

at this speed the vehicle becomes unstable and uncontrollable.
Reasonably realistic values for the vehicle in static conditions are $C_f \approx 14.8\,10^4$ N/rad and $C_r \approx 14.2\,10^4$ N/rad with $b = 1.535$ m and $w = 2.901$ m; in this case the vehicle is characterized by a slightly understeering characteristic: this does not represent an unexpected result especially considering the normalized *cornering stiffness* $K_{\lambda f} = C_f/N_f \approx 22$ rad^{-1} and $K_{\lambda r} = C_r/N_r \approx 24$ rad^{-1}. In fact, the case in which $K_{\lambda f} < K_{\lambda r}$ implies an understeering dynamic behavior because, introducing eq. (4.1), the criterium inequality becomes:

$$C_r\, b - C_f\, a = K_{\lambda r}\, N_r\, b - K_{\lambda f}\, N_f\, a = mg\frac{ab}{w}\,(K_{\lambda r} - K_{\lambda f}) \gtreqless 0. \tag{4.4}$$

Therefore the *critical speed* does not exist and the dynamics admits real negative or complex conjugated eigenvalues. The cause of this is related to the position of the centre of mass towards the front of the car, but actually near to a 50-50 mass distribution; moreover it must be underlined that in this model the front and rear tires are defined using the same coefficients and these results are obtained only considering the stability behavior at static conditions and constant speed. In general the dynamic characteristic may vary during the motion, thanks to the load transfer and the variation of the tyre stiffness slope.
Table 4.4 reports the results of the stability considerations, varying the longitudinal position of the CoM: it should be noticed that, moving towards the optimized parameter b_{opt}, or rather reducing b, the vehicle increases continually the *oversteering* behavior, that allows a better maneuverability in the corners. Moreover, for $b < b_{opt}$ the *critical speed* becomes too low and the vehicle becomes unstable during the curves; in spite of that u_{cr} does not create any issue for stability using b_{opt} because the instability occurs only when a steering maneuver is imposed.

Stability	$\overline{\mathbf{b}} \cdot \mathbf{0.8}$	$\overline{\mathbf{b}}$	$\overline{\mathbf{b}} \cdot \mathbf{1.2}$	$\mathbf{b_{opt}}$
b [m]	1.228	1.535	1.842	1.128
a [m]	1.673	1.366	1.059	1.789
$\mathbf{C_f}$ **[N/rad]**	135823	148070	153670	129050
$\mathbf{C_r}$ **[N/rad]**	151290	142280	125520	153090
$\mathbf{K_{\lambda f}}$ **[1/rad]**	25	22	19	26
$\mathbf{K_{\lambda r}}$ **[1/rad]**	21	24	27	19
$\mathbf{C_r\, b - C_f\, a}$ **[Nm/rad]**	−41450	+16140	+68470	−60630
$\mathbf{u_{cr}}$ **[km/h]**	203.93	∞	∞	165.34

Table 4.4: Stability considerations varying b, at constant wheelbase $w = 2.901$ m.

4.3.3 Vertical Position

The vertical position affects mainly the lateral and longitudinal load transfer in dynamic conditions: high values of h cause high lateral and longitudinal load transfer. The results of the simulations are reported in table 4.5 and in fig. 4.14, with the boundary condition $h \in [0.1, 1]$ m. The optimal value is obtained correspondently to the lowest value of the range: therefore a low CoM allows to improve the vehicle performance reducing the lateral and longitudinal load transfer and consequently limiting the effect of reduction of the adherence coefficient or the dual decrease of the tyre dimensional stiffness KN.

Parametric Opt. Adria	$\overline{\mathbf{h}} \cdot \mathbf{0.8}$	$\overline{\mathbf{h}}$	$\overline{\mathbf{h}} \cdot \mathbf{1.2}$	$\mathbf{h_{opt}}$
h [m]	0.264	0.330	0.396	0.1
Lap Time [s]	72.599	75.211	73.819	72.593
CPU Time [s]	1651	996	858	2096
Penalties [s]	0.146	0.138	0.145	0.148
Previous Solution Guess	yes	yes	yes	yes

Table 4.5: Simulation parameters used for CoM height optimization h.

As shown in fig. 4.15, the main differences in terms of trajectory are related to the third and the last curve of the track, represented in fig. 4.16. With the CoM at h_{opt}, the vehicle is capable to enter in the corner with a straight maneuver and to exit rapidly to start the full throttle phase; this kind of maneuver is possible thanks to the low load transfer induced, that allows to face with higher adherence limits. Moreover in the last corner is shown that the optimal vehicle enlarges the trajectory in order to prepare a straight entering in the curve; this maneuver permits to reduce the effect of the lateral load transfer.

Fig. 4.17 shows that the braking action is delayed in the optimal simulation and lower values for the longitudinal load transfer are obtained both in braking and in acceleration; the lateral load transfer is also minor to the one reached for h_{high} in all the domain of simulation.

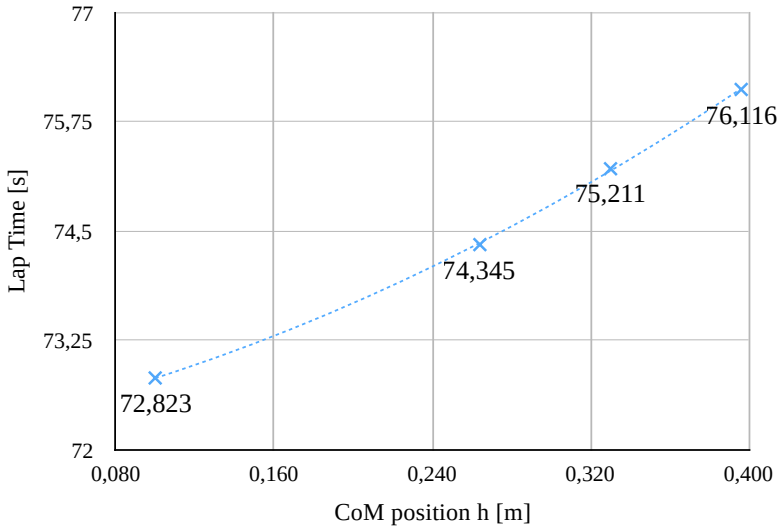

Figure 4.14: Variation of the lap time in terms of CoM height h.

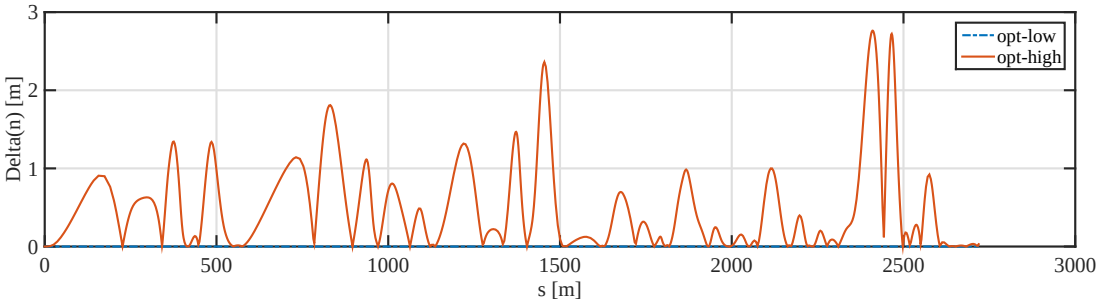

Figure 4.15: Absolute value of the difference between the CoM vertical position h for lower (optimum) and higher value of h: $\Delta n = |n_{opt} - n_{high}|$.

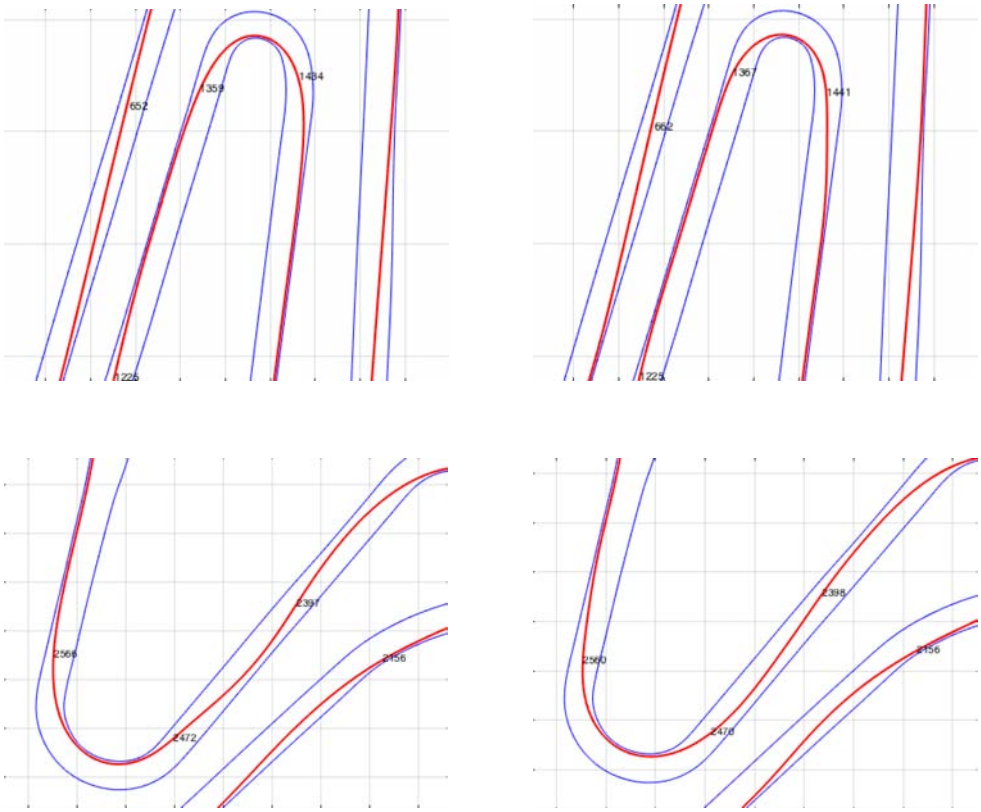

Figure 4.16: Magnified views of the third and last curve for optimal (left) and higher value (right) of the parameter.

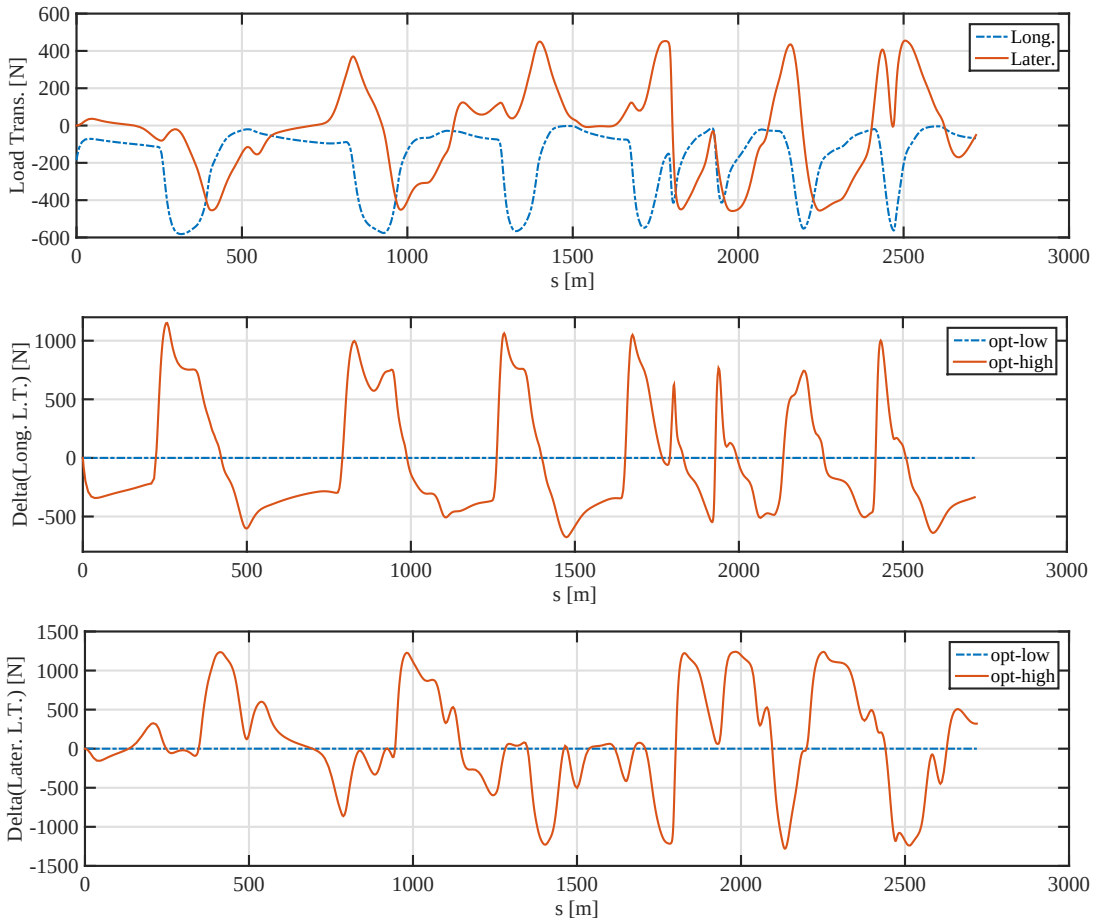

Figure 4.17: Load transfer for h_{opt} (top) and difference between the longitudinal (mid) and lateral (bottom) load transfer for lower (optimum) and higher value of h: $\Delta(\Delta N) = \Delta N_{opt} - \Delta N_{high}$.

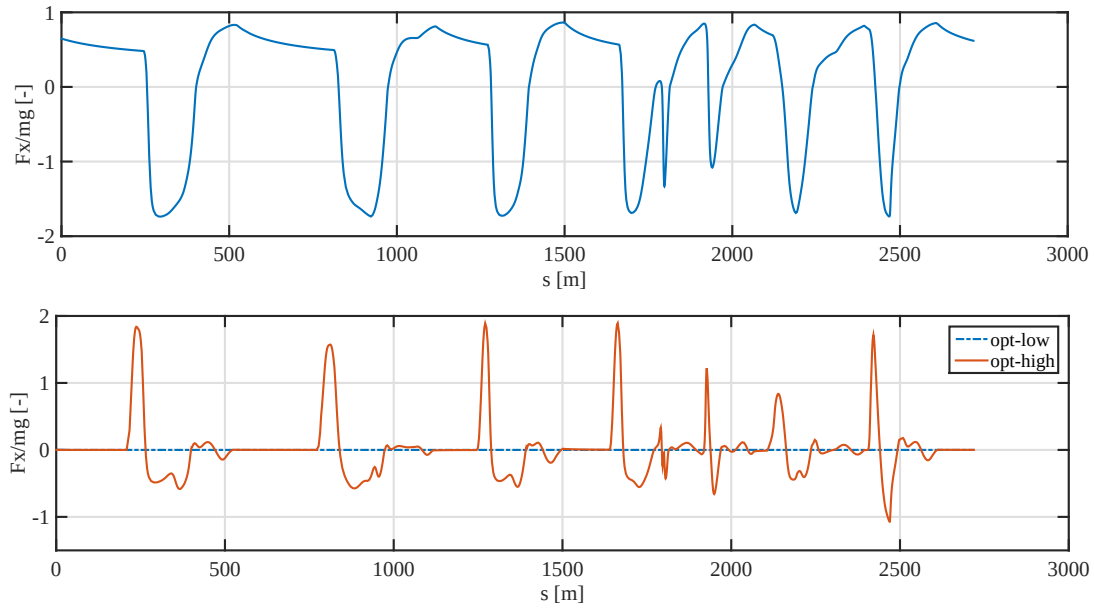

Figure 4.18: Longitudinal force for h_{opt} (top) and difference between the longitudinal force for lower (optimum) and higher value of h: $\Delta(F_x/mg) = (F_x/mg)_{opt} - (F_x/mg)_{high}$.

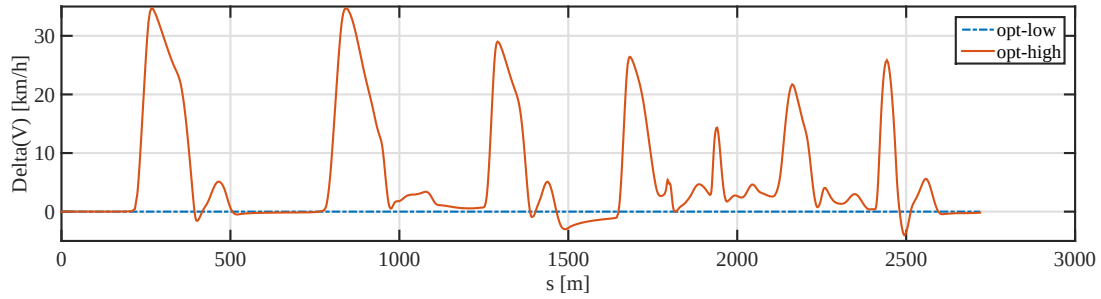

Figure 4.19: Difference between the speed profile for lower (optimum) and higher value of h: $\Delta V = V_{opt} - V_{high}$.

The total longitudinal force profile (fig. 4.18) allows to deduce that the braking action is delayed in the optimal simulation and the low load transfer permits a stronger braking force and a slightly better acceleration in the early exit of the corners.
The speed profile (fig. 4.19) shows that, assuming the optimal (lowest) vertical position of the CoM, the vehicle manages to travel the curves faster during the all track, although this advantage is lost when the speed is increased in the long straights, because lower forces are available at the driving wheels.

4.4 Wheelbase

The wheelbase of the vehicle is basically related to the static load distribution between the front and rear wheels and to the handling capabilities of the car, connected to the longitudinal load transfer; in order to consider the effect of the wheelbase only, independently to the variation of a and b, a constant ratio $b/a = k_w = 1.124$ in maintained, while w assumes different values in the range [2, 3.6] m. Thanks to this algebraic elaboration, the static load distribution becomes:

$$N_f = N_{fl} + N_{fr} = mg\,\frac{b}{w} = \frac{1}{k_w + 1}, \qquad N_r = N_{rl} + N_{rr} = mg\,\frac{a}{w} = \frac{k_w}{k_w + 1}; \quad (4.5)$$

hence, incrementing w, both a and b are incremented maintaining a constant ratio, while the static loads for front and rear wheels are constant. Therefore the assumption of $b/a = const$ allows to exclude the effect of the static loads to the analysis (which are already considered with the optimization of b) and to lead the focus to the longitudinal load transfer dependency from w.
The results of the simulations provided are summed up in table 4.6 and fig. 4.20; the improvement of the lap time follows the increase of the wheelbase and, consequently, the decrease of the load transfer, which is proportional to the ratio h/w. For high values of the wheelbase the lap time decreases less rapidly because the maneuverability in the second part of the track is reduced.

Parametric Opt. Adria	$\overline{\mathbf{w}} \cdot \mathbf{0.8}$	$\overline{\mathbf{w}}$	$\overline{\mathbf{w}} \cdot \mathbf{1.2}$	$\mathbf{w_{opt}}$
w [m]	2.321	2.901	3.481	3.600
b [m]	1.228	1.535	1.842	1.905
a [m]	1.093	1.366	1.639	1.695
Lap Time [s]	75.314	75.211	75.091	75.089
CPU Time [s]	927	996	500	485
Penalties [s]	0.122	0.138	0.152	0.159
Previous Solution Guess	yes	yes	yes	yes

Table 4.6: Simulation parameters used for wheelbase optimization w with $b/a = 1.124$.

The part of the track in which is more evident the difference between the trajectory obtained with w_{opt} and $w_{low} = 2.321$ m is the short straight before the last corner (fig. 4.21); the higher value of the wheelbase imposes a more rounded trajectory (fig. 4.22) for the optimal vehicle, that needs to use the whole road width. Even though the optimal model travels a longer distance, the reduced longitudinal load transfer allows a better braking and traction.

In fig. 4.23 can be noticed that for the optimal parameter the vehicle delays the braking action and uses a lower longitudinal load transfer both in braking and in traction condition. The lateral load transfer is not related to evident variations

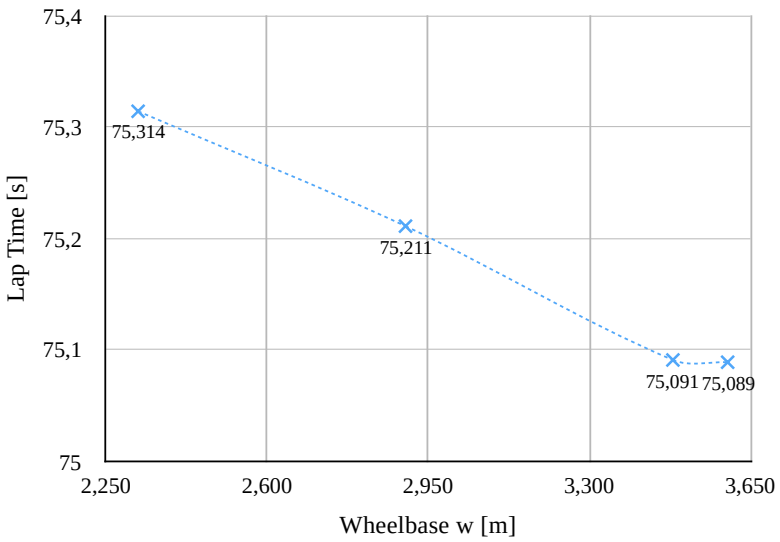

Figure 4.20: Variation of the lap time in terms of wheelbase w.

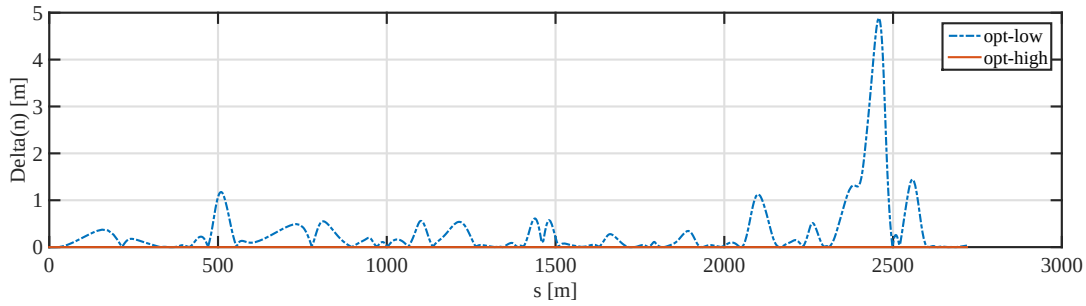

Figure 4.21: Absolute value of the difference between the wheelbase w for lower and higher (optimum) value of w: $\Delta n = |n_{opt} - n_{low}|$.

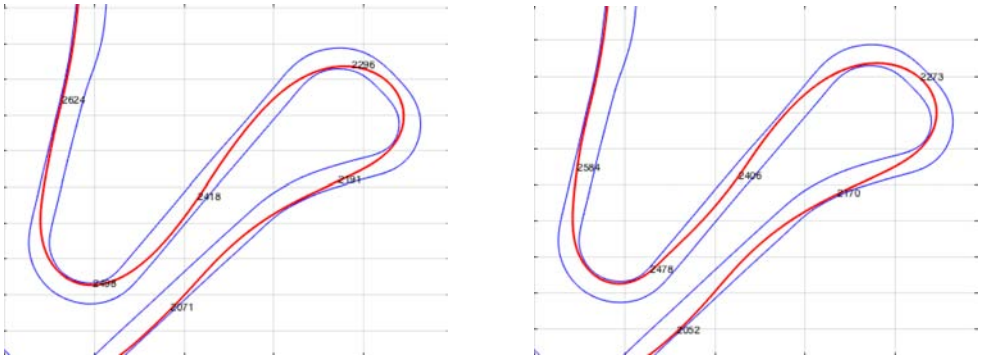

Figure 4.22: Magnified views of the last two curves for optimal (left) and lower value (right) of the parameter.

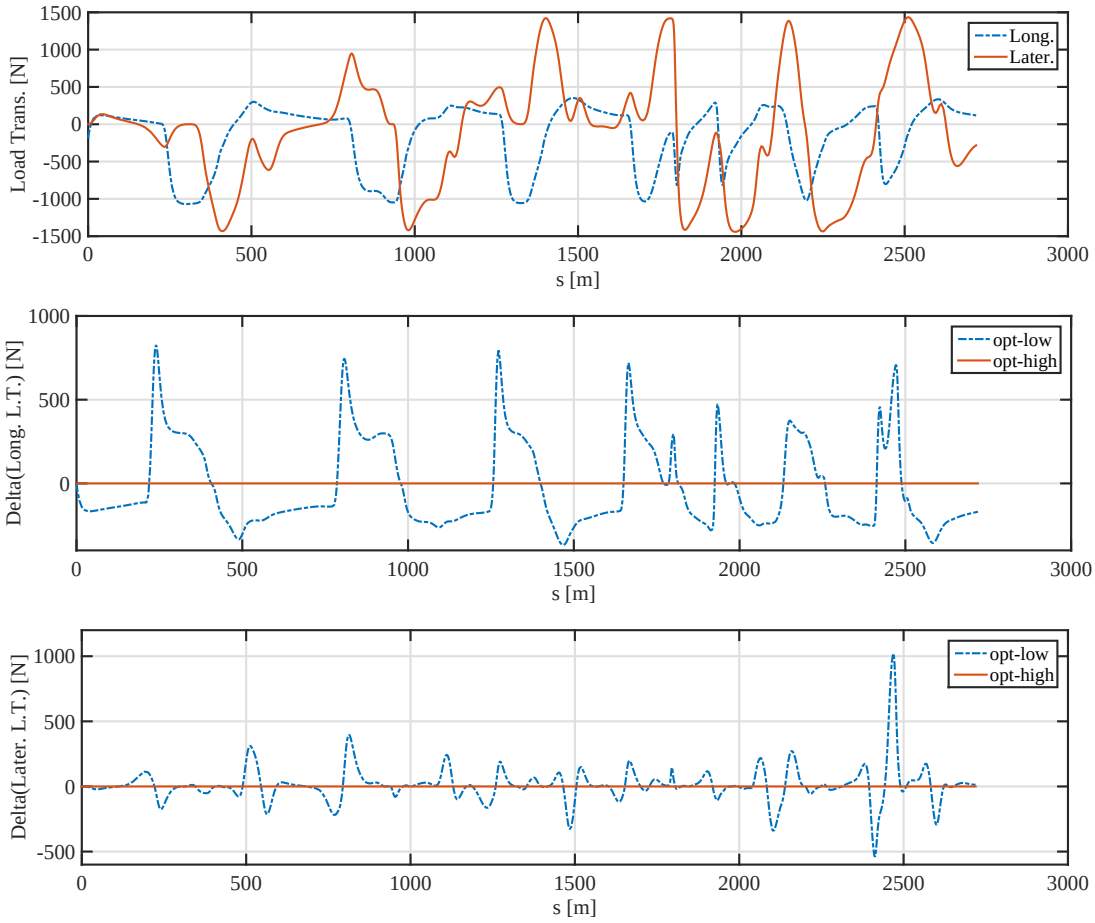

Figure 4.23: Load transfer for w_{opt} (top) and difference between the longitudinal (mid) and lateral (bottom) load transfer for lower and higher (optimum) value of w: $\Delta(\Delta N) = \Delta N_{opt} - \Delta N_{low}$.

except before the last corner in which the entering maneuver is different and provides a higher lateral load transfer for the simulation with w_{opt}: this drawback is a consequence of the increased wheelbase, for which the car is more difficult to insert in the corner. These difficulties are underlined where the curves are located in sequence and no semi-steady state phases are allowed.

The advantage of reducing the longitudinal load transfer is connected to the fact that the braking action can be delayed and a stronger braking force is available at the contact points (fig. 4.24). Moreover a slightly better traction force is exploited for the same reason.
Therefore, the vehicle enters faster in the corner and reduces the speed with a resolute braking phase; the turning and exit phases represent a drawback in terms of speed because the optimal car, due to the higher w, travels the curve slower and remains slightly slower also in the following straight. This behavior is less evident in the last sequence of corners, where the poor cornering capabilities and the shorter straights impose a different strategy and a lower advantage.

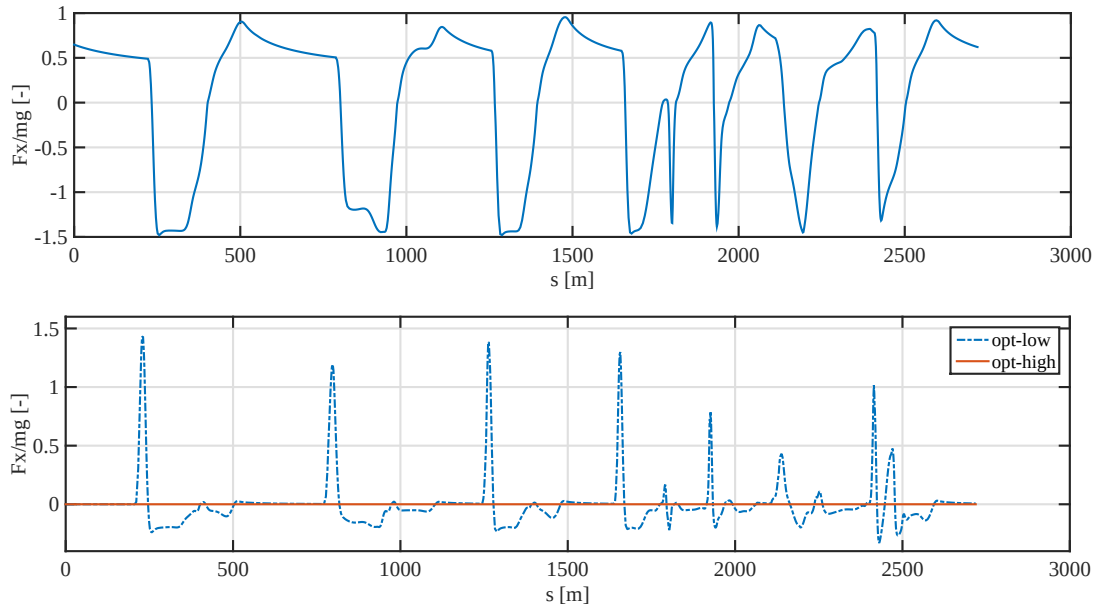

Figure 4.24: Longitudinal force for w_{opt} (top) and difference between the longitudinal force for lower and higher (optimum) value of w: $\Delta(F_x/mg) = (F_x/mg)_{opt} - (F_x/mg)_{low}$.

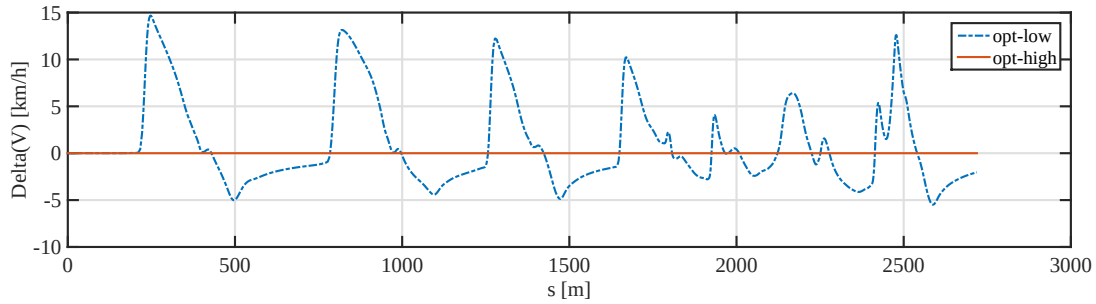

Figure 4.25: Difference between the speed profile for lower and higher (optimum) value of w: $\Delta V = V_{opt} - V_{low}$.

4.5 Vehicle Track

The width parameter T, or rather the distance between the axes of symmetry of the wheels, which is assumed equal for the front and rear axles, is mainly connected to the lateral load transfer.
Considering the range of $T \in [1.5, 2.8]$ m, some simulation results for different values of *track* are reported in tab. 4.7 and fig. 4.39. The higher the width, the lower the lateral load transfer and the better the lap time performance.

Parametric Opt. Adria	$\overline{\mathbf{T}} \cdot \mathbf{0.8}$	$\overline{\mathbf{T}}$	$\overline{\mathbf{T}} \cdot \mathbf{1.2}$	$\mathbf{T_{opt}}$
T [m]	1.613	2.016	2.419	2.800
Lap Time [s]	76.029	75.211	74.759	74.384
CPU Time [s]	673	996	757	624
Penalties [s]	0.125	0.138	0.142	0.146
Previous Solution Guess	yes	yes	yes	yes

Table 4.7: Simulation parameters used for track optimization T.

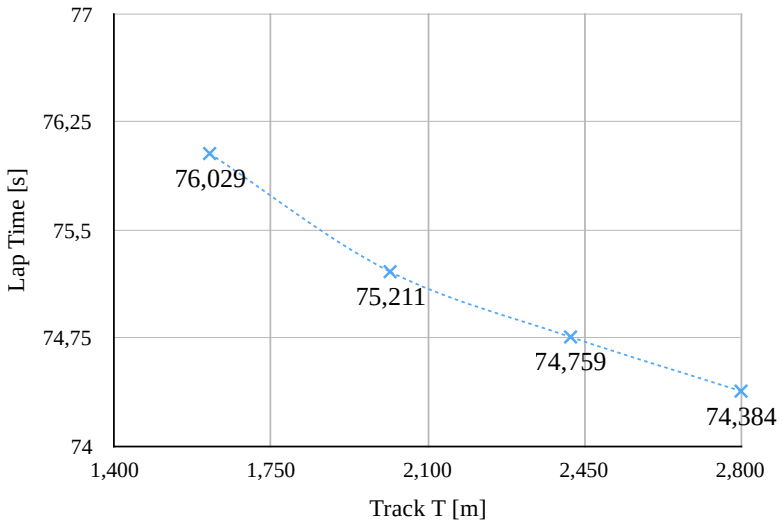

Figure 4.26: Variation of the lap time in terms of track T.

The major difference in terms of orthogonal coordinate n is obtained before the last corner (fig. 4.27), where the optimal car is capable of a more straight trajectory (fig. 4.28) because the lateral load transfer is reduced and the adherence limits are high enough.

In fig. 4.29 it can be noticed that, in most of the curves, the model that implements T_{opt} delays the braking, brakes stronger and anticipates the traction phase; the lateral load transfer is significantly lower during the whole track.
The same conclusions can be drawn considering the longitudinal force profile of fig. 4.30: higher and delayed braking force and more resolute acceleration are used.

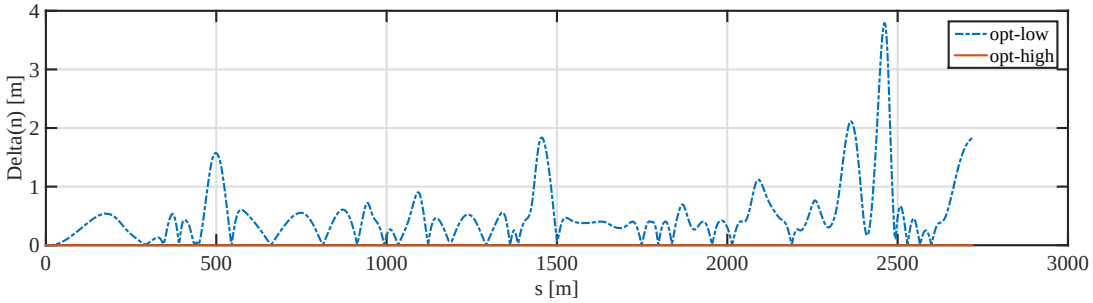

Figure 4.27: Absolute value of the difference between the wheelbase T for lower and higher (optimum) value of T: $\Delta n = |n_{opt} - n_{low}|$.

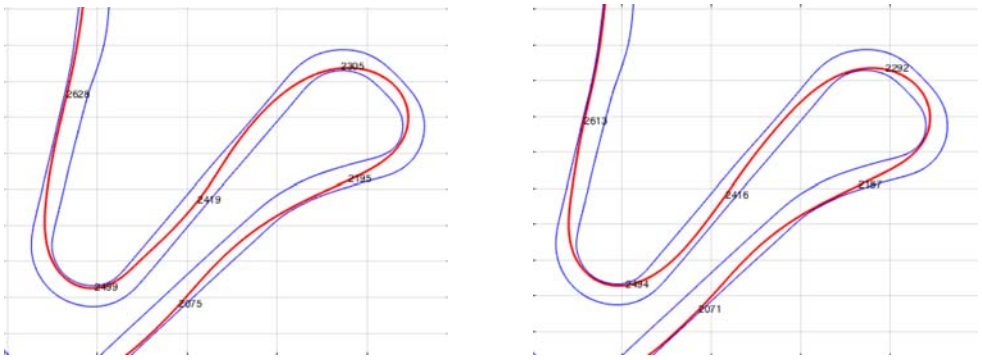

Figure 4.28: Magnified views of the last two curves for optimal (left) and higher value (right) of the parameter.

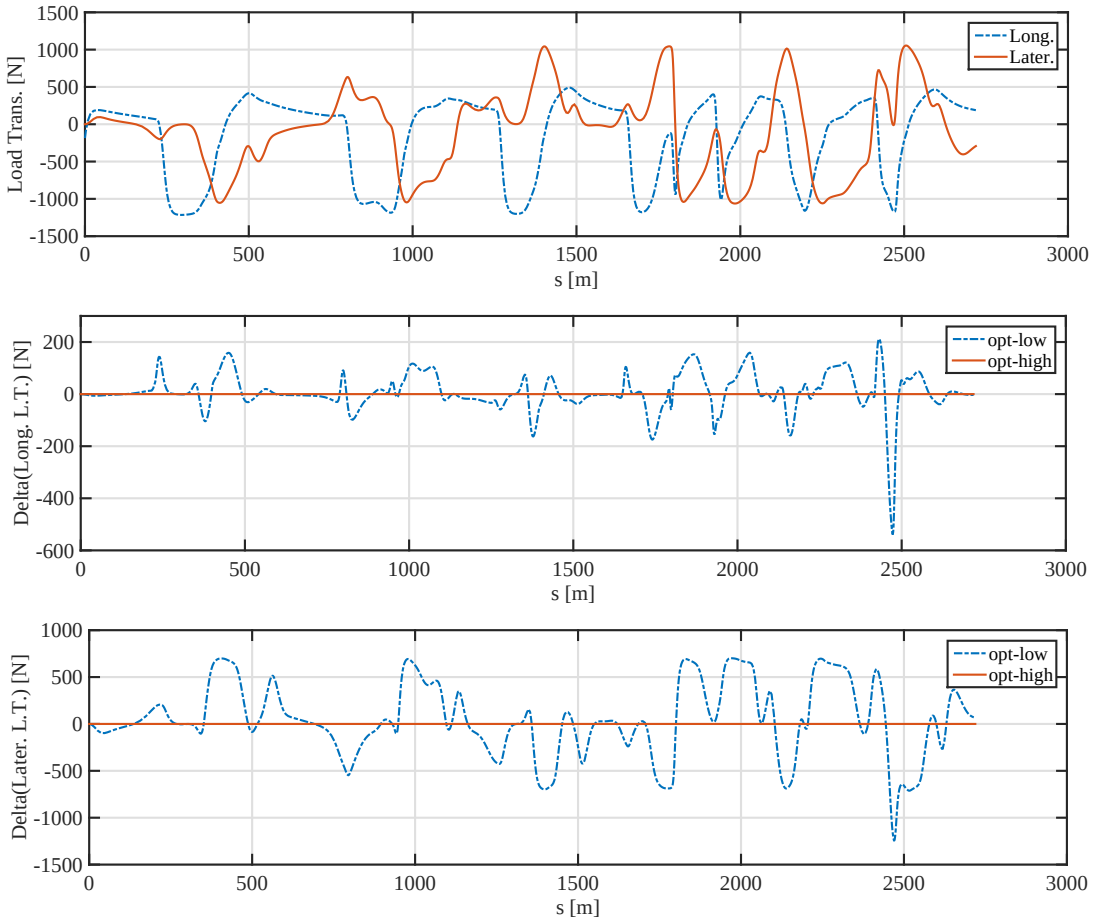

Figure 4.29: Load transfer for T_{opt} (top) and difference between the longitudinal (mid) and lateral (bottom) load transfer for lower and higher (optimum) value of T: $\Delta(\Delta N) = \Delta N_{opt} - \Delta N_{low}$.

In spite of that a greater difference is highlighted in the last corner, where this behavior is accentuated.
The speed profile (fig. 4.31) shows that a higher total velocity is reached in the cornering maneuver, although the speed advantage is reduced during the following acceleration. In the last corner the speed of the optimal model is lower in the first half of the curve, while in the traction phase the car achieves higher values of V.

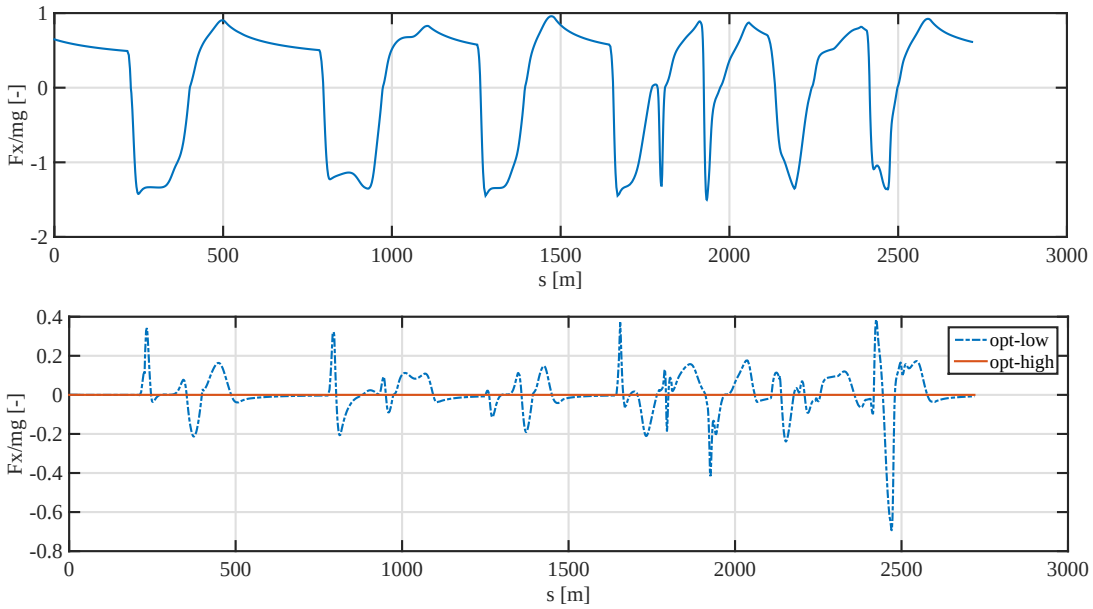

Figure 4.30: Longitudinal force for T_{opt} (top) and difference between the longitudinal force for lower and higher (optimum) value of T: $\Delta(F_x/mg) = (F_x/mg)_{opt} - (F_x/mg)_{low}$.

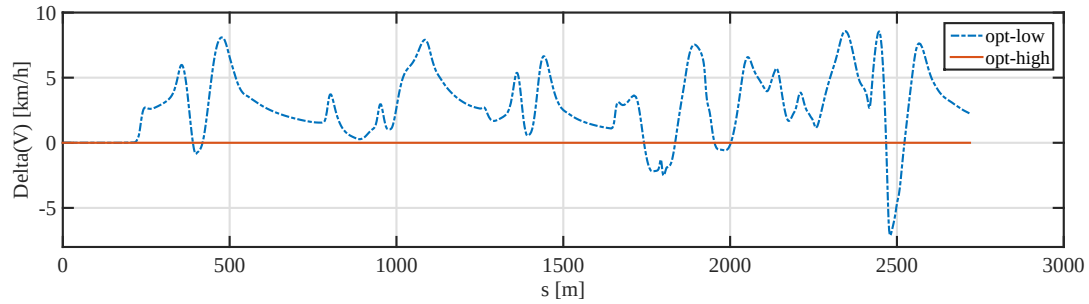

Figure 4.31: Difference between the speed profile for lower and higher (optimum) value of T: $\Delta V = V_{opt} - V_{low}$.

4.6 Yaw Inertia

The yaw inertia I_z reflects the cornering capabilities of the vehicle and is included in the Euler equation around the z axis of the SAE triad (eq. 2.15). Table 4.8 shows that this parameter, that is assumed to vary within the range [1000, 3000] kgm^2, has a weak effect on the lap time: in fact the variation in the interval considered is almost 0.2 s. The same overall behavior was captured in [10] where, considering only the range used, the variation of the lap time assumes a similar form to the one obtained in fig. 4.32, although the model treated maintains a constant lap time of 75.212 s up to inertia values of 10^4 kgm^2.
Because of the particular form of the lap time curve with a variation of I_z, in this case will be compared three different simulations characterized by the optimal (and maximum) value of yaw inertia $I_{z,opt} = I_{z,max} = 3000$ kgm^2 and two lower values: $I_{z,low} = I_{z,min} = 1000$ kgm^2 and $I_{z,high} = \bar{I}_z = 1700$ kgm^2.

Parametric Opt. Adria	$\mathbf{I_{z,min}}$	$\mathbf{\bar{I}_z \cdot 0.8}$	$\mathbf{\bar{I}_z}$	$\mathbf{\bar{I}_z \cdot 1.2}$	$\mathbf{I_{z,opt}}$
$\mathbf{I_z}$ **[m]**	1000	1360	1700	2040	3000
Lap Time [s]	75.154	75.138	75.211	75.204	75.098
CPU Time [s]	910	781	996	889	2157
Penalties [s]	0.126	0.126	0.138	0.138	0.126
Previous Solution Guess	yes	yes	yes	yes	yes

Table 4.8: Simulation parameters used for yaw inertia optimization I_z.

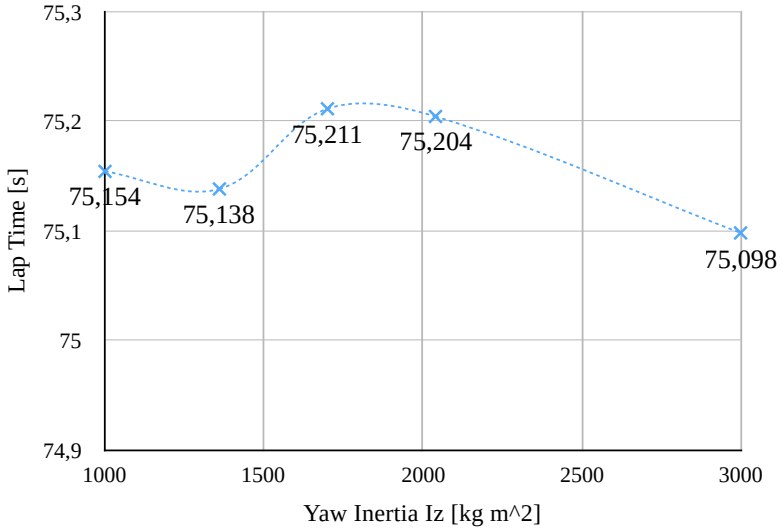

Figure 4.32: Variation of the lap time in terms of yaw inertia I_z.

The only significant difference in terms of orthogonal coordinate n (fig. 4.33) occurs between $I_{z,opt}$ and $I_{z,low}$ in the last corner of the track: the optimal vehicle

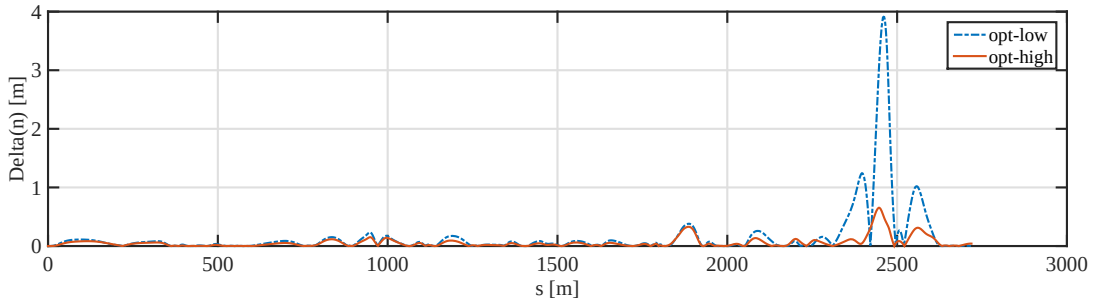

Figure 4.33: Absolute value of the difference between the wheelbase I_z for lower, optimum and higher value of I_z: $\Delta n = |n_{opt} - n_{high}|$ and $\Delta n = |n_{opt} - n_{low}|$.

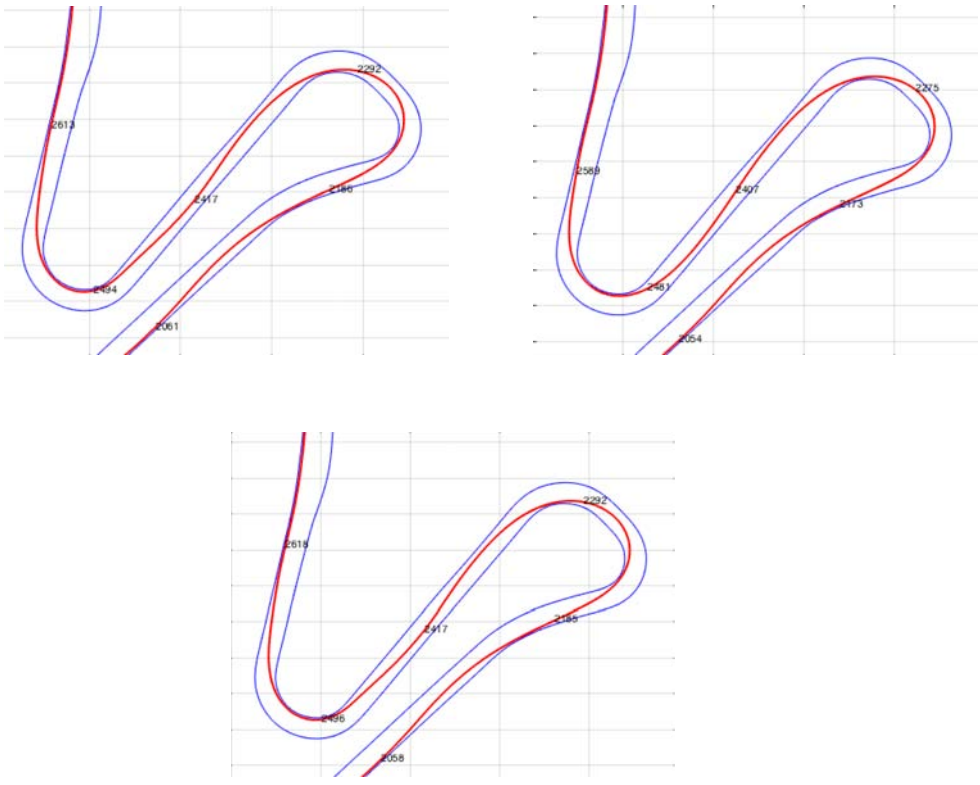

Figure 4.34: Magnified views of the last and second-last curves for optimal (left), lower value (right) and higher value (bottom) of the parameter.

uses a more straight trajectory to enter in the curve, while at the exit the approach to the external curb occurs later (fig. 4.34).

As for lateral and longitudinal load transfer the result is the same (fig. 4.35): the models which implement $I_{z,opt}$ and $I_{z,low}$ register a difference in the last corner, while no significant differences are obtained between $I_{z,opt}$ and $I_{z,high}$. The braking action is delayed and more longitudinal force is applied for braking and traction; the lateral load transfer, moreover, is higher for the optimal model in the first phase, but lower in the second part of the maneuver and newly higher in the curve exit. This considerations allow to make an hypothesis to justify the non-intuitive advantage reached with higher values of I_z: the vehicle starts the cornering maneuver and the higher inertia imposes to continue the yaw rotation exploiting the oversteering behavior of the car; at the end of the corner the vehicle stops the yaw maneuver because the steering was previously set parallel to the vehicle. Therefore the vehicle anticipates the phase in which the steering is straight and is able to impose higher longitudinal forces.
In most of the curves, in fact, the steering angle is lower for the optimal vehicle; in the last corner, instead, a greater steering angle is needed before and during the curve because of the different trajectory, although lower steering angles are reached in the exit phase.
The longitudinal force profile (fig. 4.37) and the speed profile (fig. 4.38) confirm the same conclusions exposed for the longitudinal load transfer.

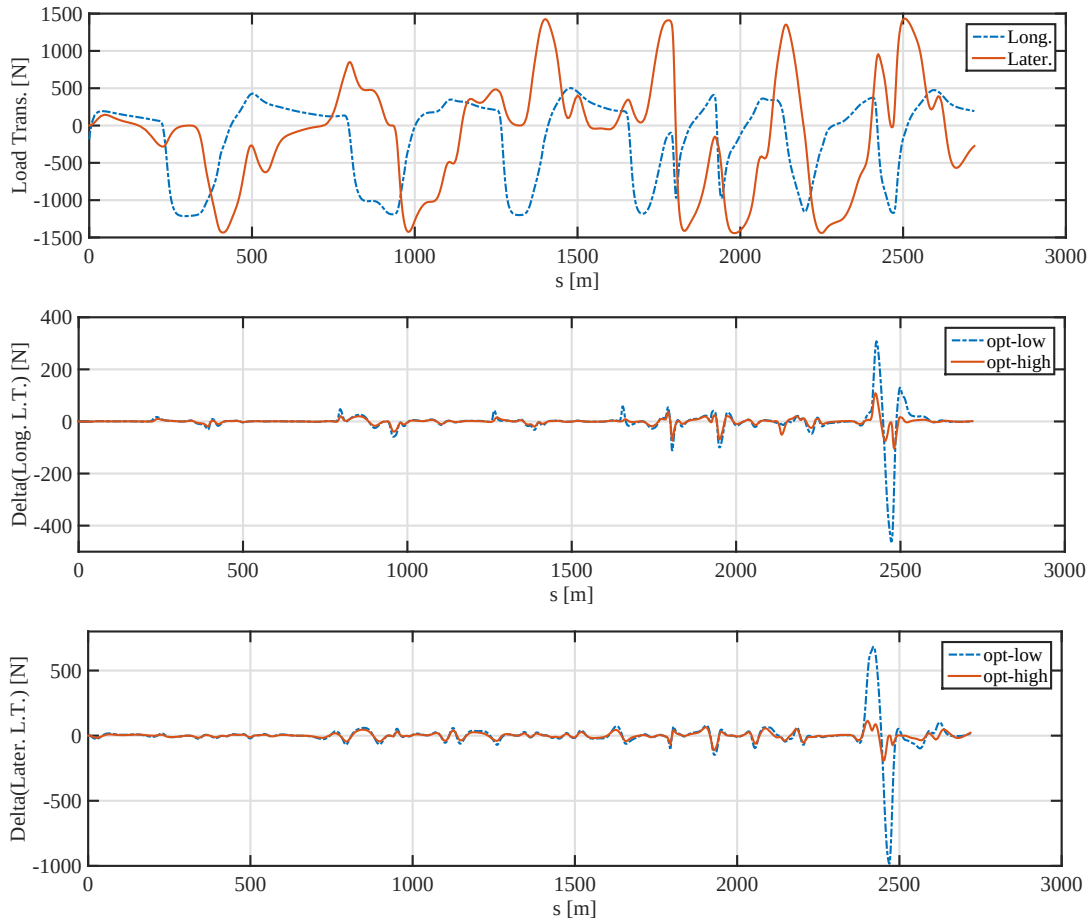

Figure 4.35: Load transfer for $I_{z,opt}$ (top) and difference between the longitudinal (mid) and lateral (bottom) load transfer for lower and higher (optimum) value of I_z: $\Delta(\Delta N) = \Delta N_{opt} - \Delta N_{high}$ and $\Delta(\Delta N) = \Delta N_{opt} - \Delta N_{low}$.

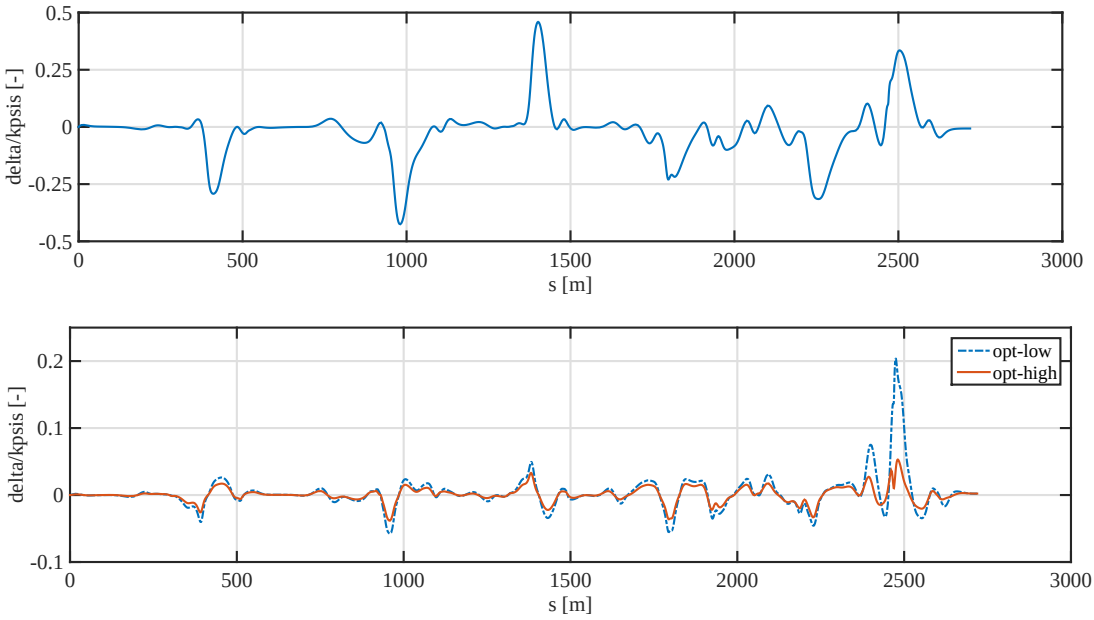

Figure 4.36: Normalized steering angle for $I_{z,opt}$ (top) and difference between the longitudinal force for lower, optimal and higher value of I_z: $\Delta(\delta/k_\delta) = (\delta/k_\delta)_{opt} - (\delta/k_\delta)_{high}$ and $\Delta(\delta/k_\delta) = (\delta/k_\delta)_{opt} - (\delta/k_\delta)_{low}$.

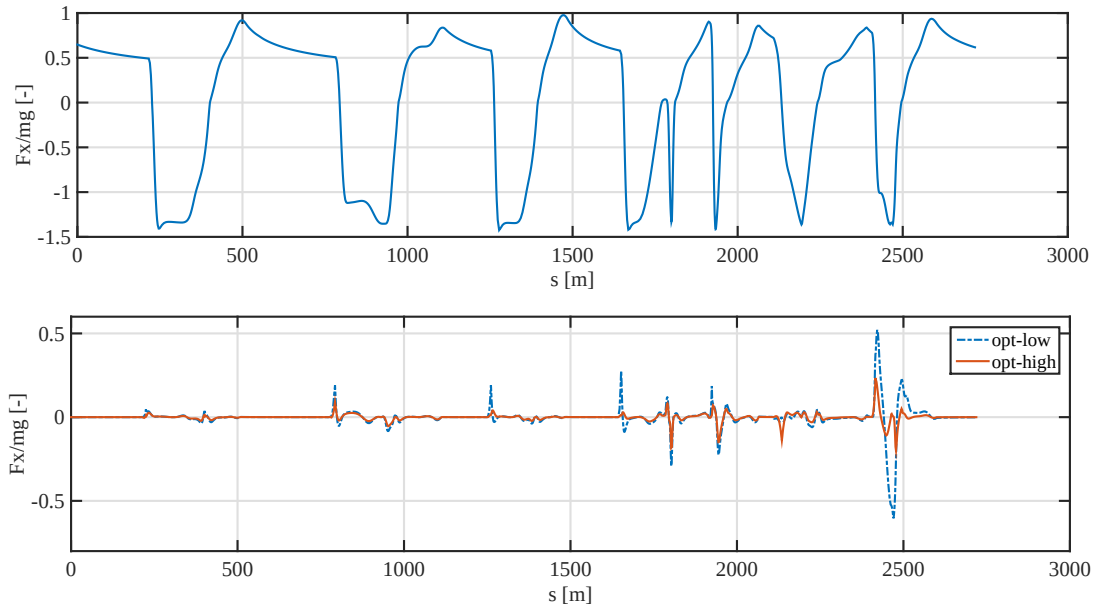

Figure 4.37: Longitudinal force for $I_{z,opt}$ (top) and difference between the longitudinal force for lower, optimal and higher value of I_z: $\Delta(F_x/mg) = (F_x/mg)_{opt} - (F_x/mg)_{high}$.

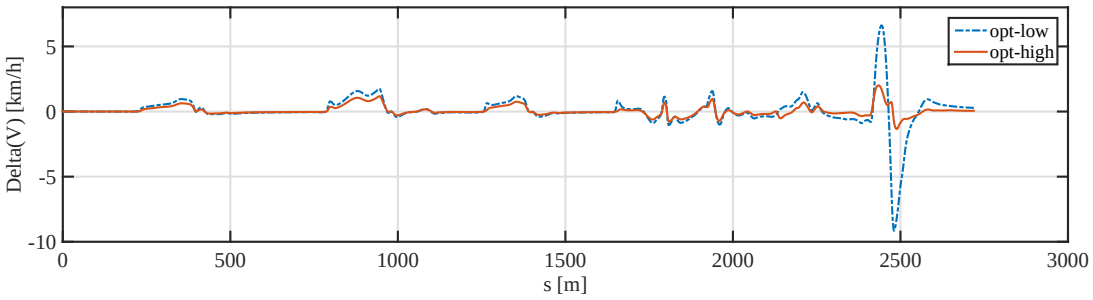

Figure 4.38: Difference between the speed profile for lower, optimum and higher value of I_z: $\Delta V = V_{opt} - V_{high}$ and $\Delta V = V_{opt} - V_{low}$.

4.7 Differential

The differential is an important mechanical device that allows an improvement in vehicle maneuverability; in fact the differential allows to split the torque delivered to the driving axle towards each wheel with a particular criterium: the greater is the wheel spin, the smaller is the torque delivered. This is the basic functioning principle behind the so-called *speed sensing differentials*, or rather the systems based on the driving wheel speed difference.
Two different operating limits can be defined: the first one is the condition of *open differential*, that delivers the torque in order to obtain the same longitudinal tyre forces on each wheel of the driving axle, with condition close to the pure slip; the other dual limit consists in the condition of *locked differential*, for which the driving axle is completely locked as if the differential becomes a rigid joint between the wheels; this operating condition is useful during the traction and braking of the vehicle, in which the car needs to deliver the maximum power to the ground.
A simple model for this complex system is expressed by the following relation between the torques at the rear axle $\mathcal{T}_{rl}$ and $\mathcal{T}_{rr}$ (for a rear wheel drive car) and the wheel spin velocities ω_{rl} and ω_{rr}:

$$\mathcal{T}_{rl} - \mathcal{T}_{rr} = k_d \, (\omega_{rr} - \omega_{rl}); \tag{4.6}$$

k_d is the viscosity parameter of the differential and is measured in [Nms]; $k_d = 0$ represents the condition of fully *open differential*, while for $k_d \to \infty$ the system is completely *locked*. Therefore for *locked* differential the equation becomes:

$$\omega_{rr} - \omega_{rl} = 0. \tag{4.7}$$

In table 4.9 are reported the results of the simulations with different values of k_d; the path constraint of equation (4.6) represents a very tough condition for the simulation and this is demonstrated by the elevated simulation time values. In this case, if on the one hand the optimum parameter value seems to follow the form of the curve that joins the points of different simulations, on the other hand it does not correspond to an absolute minimum in terms of lap time: probably the curve presents some waves where the lap time gains the minimum values and the optimizer has some difficulties for a proper convergence to the optimum value.

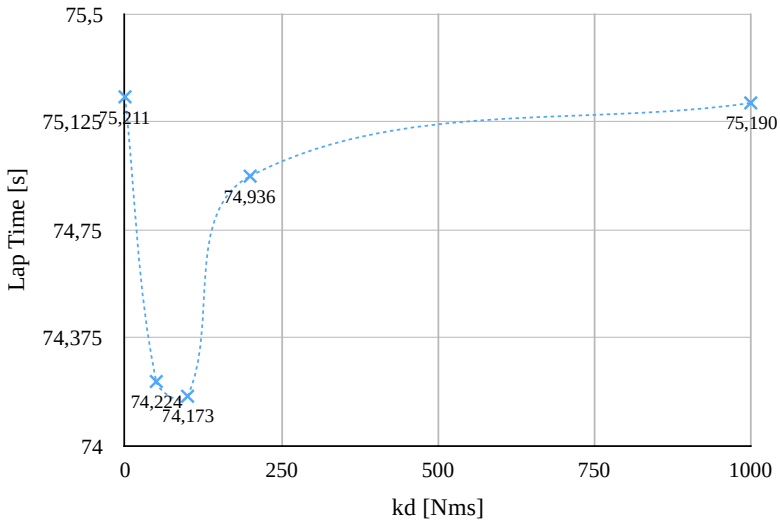

Figure 4.39: Variation of the lap time in terms of viscosity coefficient of the differential k_d.

Despite of that, a concrete optimum value for k_d can be realistically found in the interval $50 \div 100$.

Par. Opt. Adria	**Open**	$\overline{\mathbf{k}}_\mathbf{d} \cdot \mathbf{0.5}$	$\overline{\mathbf{k}}_\mathbf{d}$	$\overline{\mathbf{k}}_\mathbf{d} \cdot \mathbf{2}$	$\overline{\mathbf{k}}_\mathbf{d} \cdot \mathbf{10}$	$\mathbf{k_{d,opt}}$	**Locked**
$\mathbf{k_d}$ **[Nms]**	0	50	100	200	1000	84	∞
Lap Time [s]	75.211	74.224	74.173	74.936	75.190	74.471	75.629
CPU Time [s]	996	2043	1972	4418	8229	1249	1449
Penalties [s]	0.138	0.188	0.267	0.405	0.497	0.264	0.551
Prev. Sol. Guess	yes	yes	yes	yes	yes	yes	yes

Table 4.9: Simulation parameters used for differential viscous constant optimization k_d.

In fig. 4.40 is represented the difference of trajectory between the simulations for $k_{d,low} = 0$ Nms and the optimal value assumed as $k_{d,opt} \approx 100$ Nms (dash-dot line) and between the results obtained with $k_{d,high} = 1000$ Nms and the optimal value (continuous line). It can be observed that Δn, calculated considering the difference between the higher and optimal parameters, assumes the major values in the second, third and last curve; for the lower value of k_d, instead, the greatest difference is reached before the third and last curve.
The magnified views of the track are represented in fig. 4.41; considering the second corner, the optimal vehicle is capable of a lower enlargement of the trajectory than the model with $k_{d,high}$ because the handling is affected by the partial locking of the differential, that reduces the cornering capabilities. In the following straight the main difference is related to $k_{d,low}$: in fact the optimal model accentuates the opposite steering maneuver to prepare the curve, while with the open differential

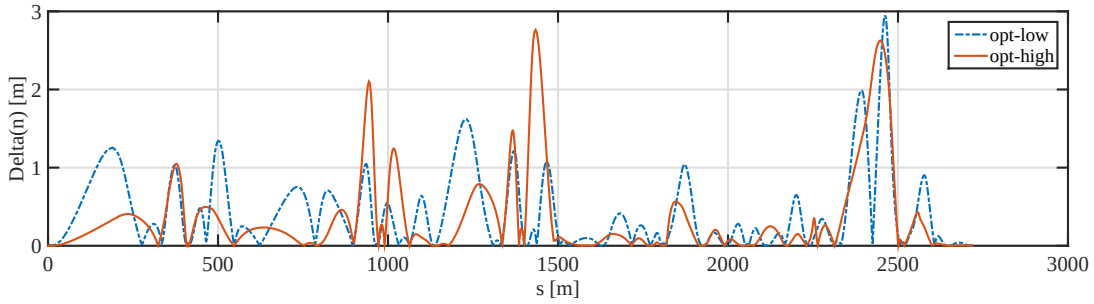

Figure 4.40: Absolute value of the difference between the wheelbase k_d for lower, optimum and higher value of k_d: $\Delta n = |n_{opt} - n_{high}|$ and $\Delta n = |n_{opt} - n_{low}|$.

this maneuver is not needed. If one the one hand the entering trajectory is similar using the optimal and the lower value, the vehicle with $k_{d,high}$ travels a more rounded trajectory, because of the higher degree of locking; at the same way, for the exit maneuver, with the lower and optimal value the trajectory is more straight and reduces the road traveled, while for the higher value the trajectory is gradual and rounded. In the last corner a different strategy is adopted for each value of k_d: in the approaching maneuver the changing of direction is more evident passing from $k_{d,low}$ to $k_{d,high}$, and the entering becomes less and less straight; the exit phase is similar, although for the lower parameter a more direct trajectory can be observed.

In general it can be noticed that the differences in terms of load transfers define irregular profiles with quite low values; as for the longitudinal load transfer (fig. 4.42) the optimal vehicle usually is capable of delaying the braking phase, of braking stronger and accelerating before the vehicles in which are implemented different values of k_d. Moreover it can be seen that in some corners the vehicle that uses $k_{d,high}$ has the possibility to slightly anticipate the traction phase at the exit of the curves and to further delay the braking action, thanks to the more locked differential.

In terms of steering angle (fig. 4.43) the main differences are calculated between the optimal model and the vehicle that uses $k_{d,high}$: the optimal car adopts a higher steering angle in most of the curves because the trajectory is more sharp; at the same way with $k_{d,opt}$, the steering angle needed is lower than the one used with the lower value of the parameter.

The longitudinal force profile (fig. 4.44) confirms the consideration deduced for the longitudinal load transfer, while a further analysis can be focused on the speed difference in fig. 4.45; the optimal parameter allows a faster entering and exit maneuver in all the corners respect to the use of $k_{d,low}$, and the advantage in maintained during the straights. In spite of that a slower cornering phase is obtained because of the differential partial degree of locking. An advantage is taken also with reference to the vehicle equipped with $k_{d,high}$ because the more rounded trajectory is obtained traveling greater distances; in spite of that a better traction and a higher speed can be obtained with a locked differential in the straights.

In fig. 4.46 is represented the term $\mathcal{T}_{rl} - \mathcal{T}_{rr} = k_d\,(\omega_{rr} - \omega_{rl})$ for $k_{d,opt}$ and $k_{d,high}$; the equation results identically null for $k_{d,low}$. Considering the first corner

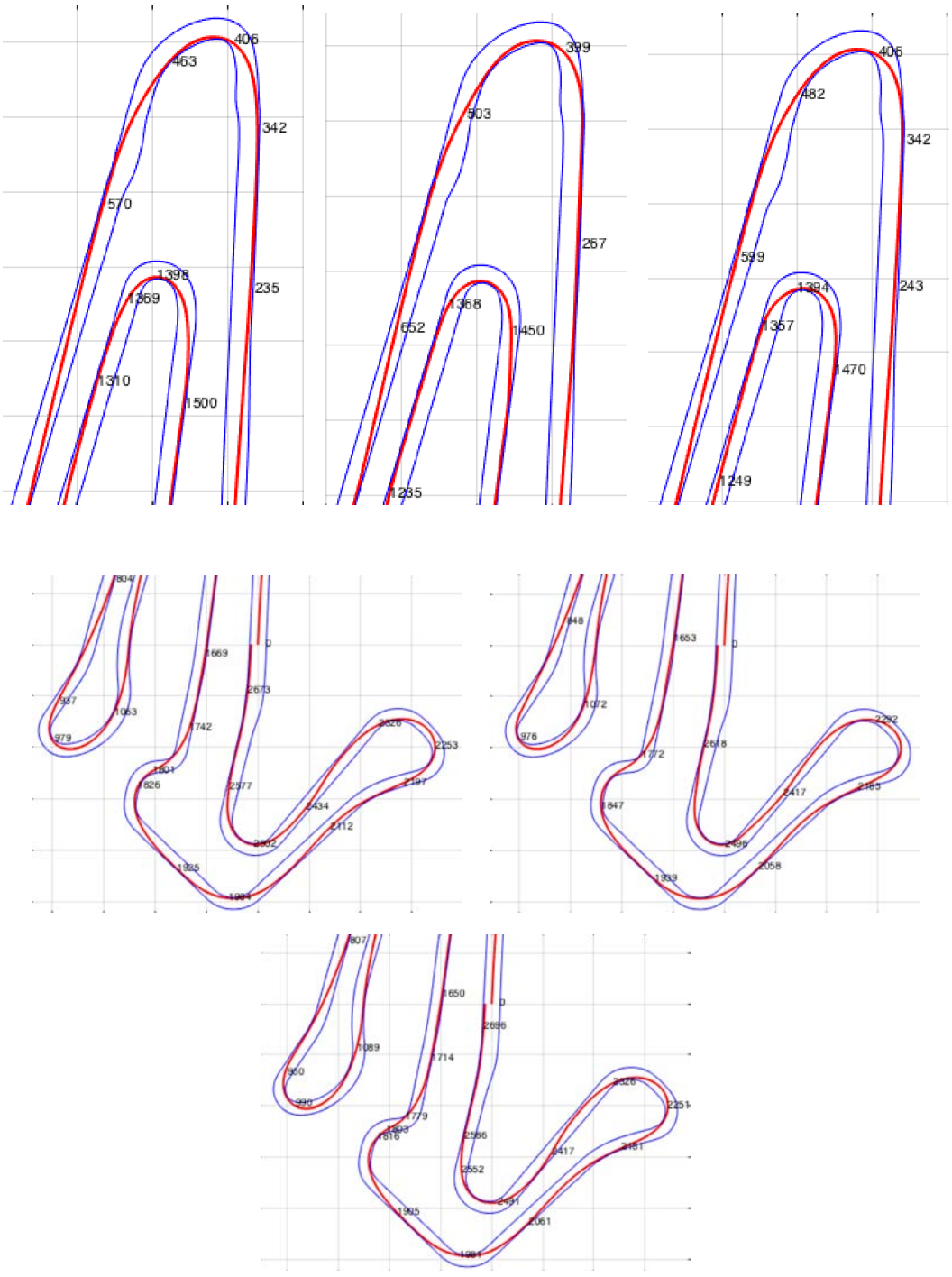

Figure 4.41: Magnified views of the first and third corners (top) for optimal (left), lower value (mid) and higher value (right) of the parameter; underneath is represented the second curve with second half of the track for optimal (left), lower value (right) and higher value (bottom) of the parameter.

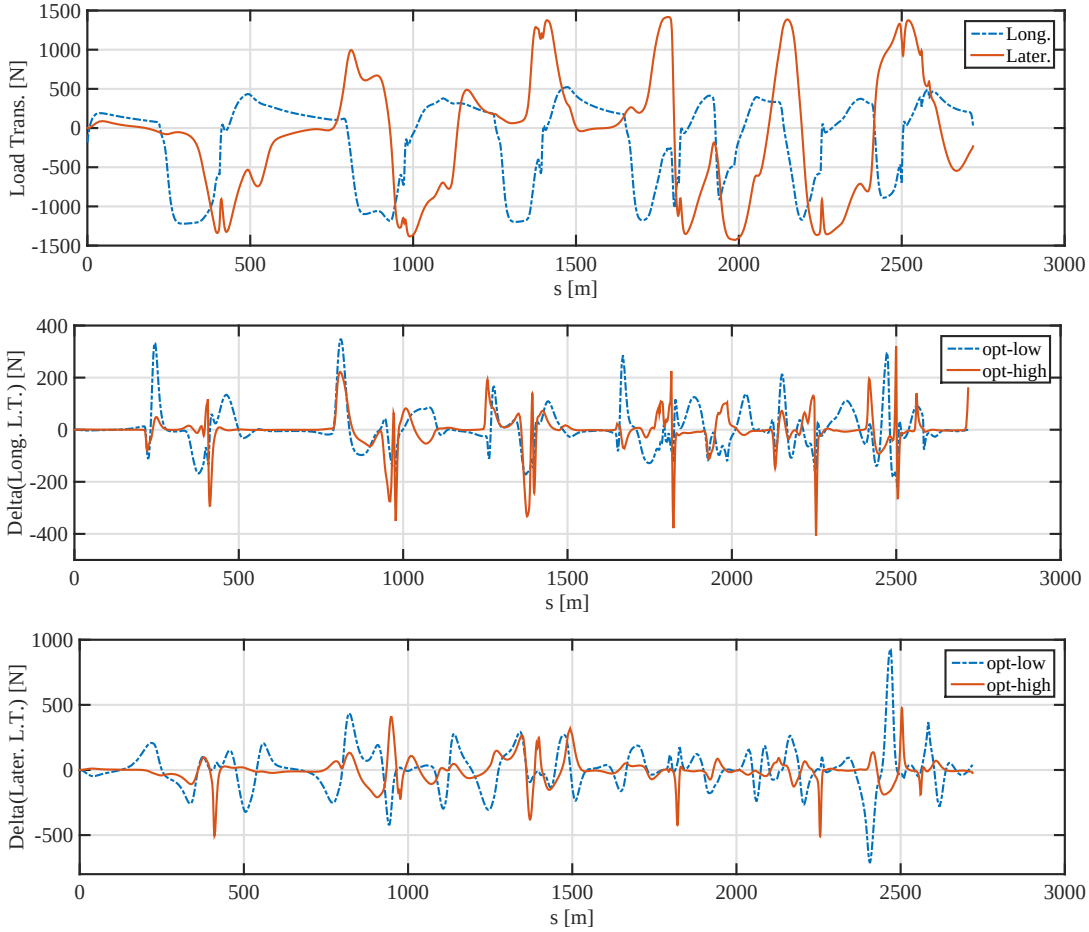

Figure 4.42: Load transfer for $k_{d,opt}$ (top) and difference between the longitudinal (mid) and lateral (bottom) load transfer for lower and higher (optimum) value of k_d: $\Delta(\Delta N) = \Delta N_{opt} - \Delta N_{high}$ and $\Delta(\Delta N) = \Delta N_{opt} - \Delta N_{low}$.

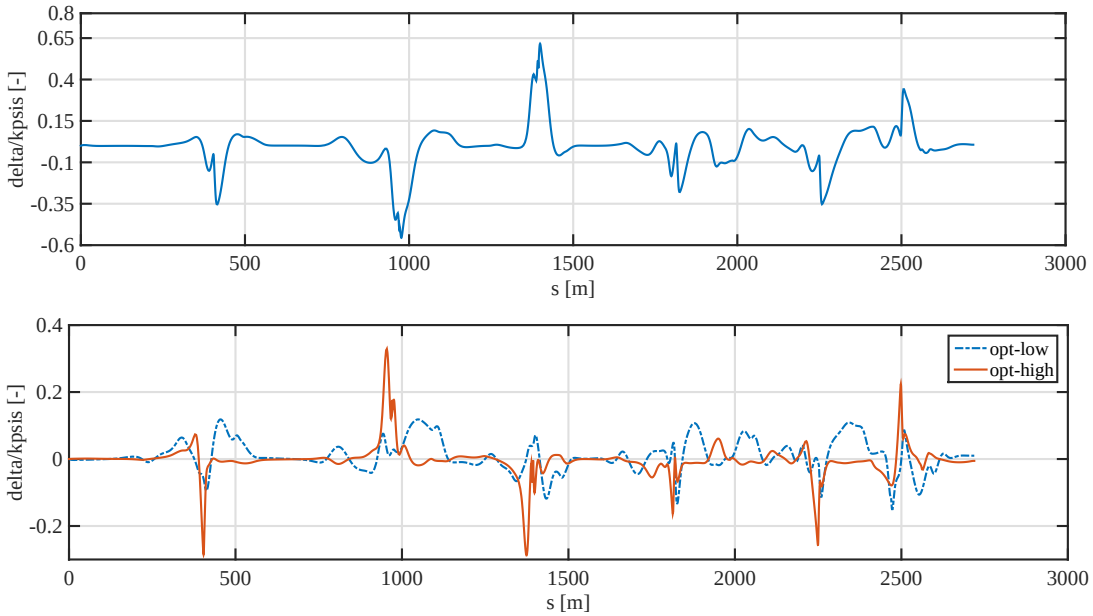

Figure 4.43: Normalized steering angle for $k_{d,opt}$ (top) and difference between the longitudinal force for lower, optimal and higher value of k_d: $\Delta(\delta/k_\delta) = (\delta/k_\delta)_{opt} - (\delta/k_\delta)_{high}$ and $\Delta(\delta/k_\delta) = (\delta/k_\delta)_{opt} - (\delta/k_\delta)_{low}$.

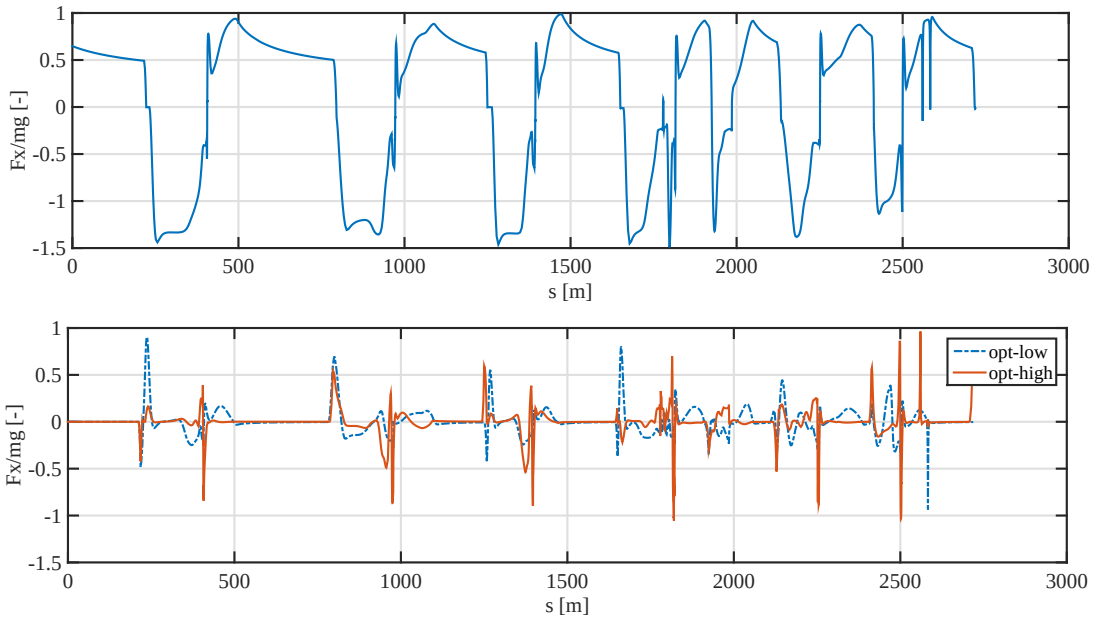

Figure 4.44: Longitudinal force for $k_{d,opt}$ (top) and difference between the longitudinal force for lower, optimal and higher value of k_d: $\Delta(F_x/mg) = (F_x/mg)_{opt} - (F_x/mg)_{high}$ and $\Delta(F_x/mg) = (F_x/mg)_{opt} - (F_x/mg)_{low}$.

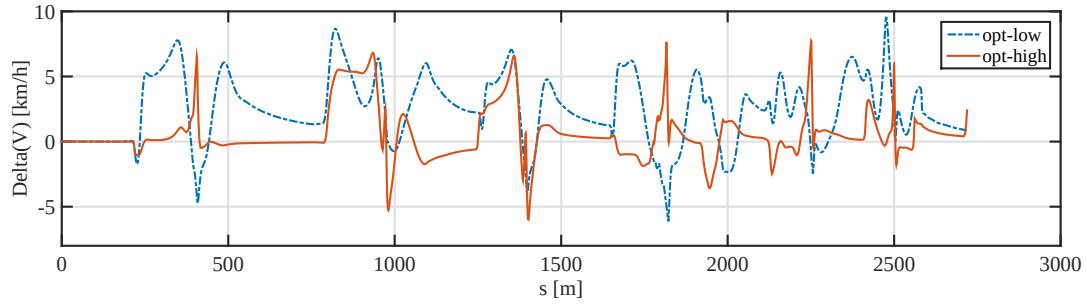

Figure 4.45: Difference between the speed profile for lower, optimum and higher value of k_d: $\Delta V = V_{opt} - V_{high}$ and $\Delta V = V_{opt} - V_{low}$.

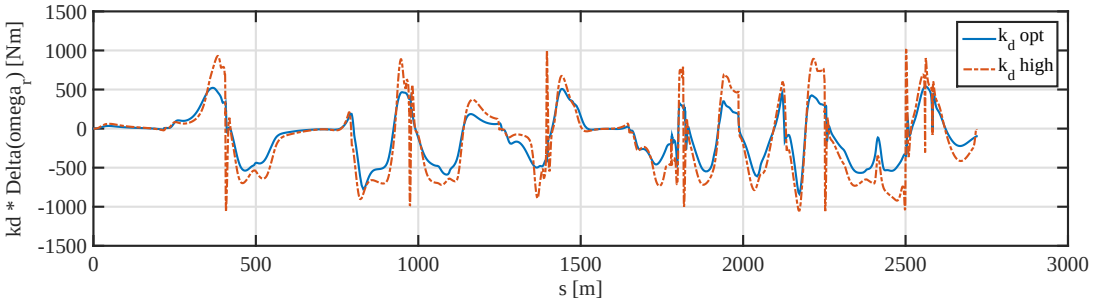

Figure 4.46: Difference between the rear left and rear right applied torque for $k_{d,opt}$ (continuous line) and $k_{d,high}$ (dash-dot line): $\mathcal{T}_{rl} - \mathcal{T}_{rr} = k_d\,(\omega_{rr} - \omega_{rl})$.

as an example of the typical behavior of the vehicle, initially the external wheel is faster than the interior one and more torque is delivered at the internal wheel; in the following phase, during the corner, the internal wheel becomes faster and the torque is transmitted to the external wheel to accentuate the oversteering action. This regulation of the torque for an improvement of the dynamics is known as *torque vectoring*. It should be noticed that the simulation for $k_{d,high}$ provides higher values of $k_d\,(\omega_{rr} - \omega_{rl})$ during the whole track but the profile presents also some vibrations because of the higher difficulty of convergence: the higher is k_d, the more restrictive is the constraint and the optimal solution is harder to find.

4.8 Lift Coefficient

The lift forces are important parameters for the vehicle dynamics because, for the racing cars, determine an increment of the normal loads, that can be traduced in higher forces available at the wheels, although a decrease of the adherence limit is inevitable. Typically for the Grand Touring racing cars the rear wing develops the most part of the lift downforce, while the frontal aerodynamics and the splitters are related to a minor fraction of the total vertical force; as shown in eq. (2.24), the two separated contributes enter in the load equations, although the parametric analysis is generated for a single lift parameter, due to numerical advantages in terms of simulation time[1]. Therefore a total value of the lift area is evaluated as $C_LA = C_{Lf}A + C_{Lr}A$ and different parameters are obtained incrementing or reducing the initial value $\overline{C_LA}$ by the 20%; at the rear wing is estimated the 70% of the total force, while the front provides with the remaining 30%. It must be considered also that these different parameters are obtained with a proper inclination of the rear wing and higher angles correspond to higher drag resistance: consequently the ratio between the lift and drag forces C_LA/C_DA is maintained constant for each simulation.
Table 4.10 and fig. 4.47 report a summing up of the results obtained for different parameters, considering an interval of $C_LA \in [1, 3.5]$ m^2 as boundary condition for the parametric optimization, which defines a range of realistic values for C_LA. With a constant ratio of $C_LA/C_DA = 3$, assumed as a typical value for a GT3 car, the optimum value is coincident to the maximum value of the interval considered: greater values for C_LA are not realistic; this behavior permits to conclude that the higher are the lift forces, the lower is the lap time; the vehicle in fact is subjected to higher loads and higher forces can be transmitted from the tires to the ground, although lower values for the friction coefficients are available. Moreover, due to the higher downforce at the rear axle, the longitudinal load transfer is incremented, increasing consequently the traction of the vehicle.

Parametric Opt. Adria	$\mathbf{\overline{C_LA} \cdot 0.8}$	$\mathbf{\overline{C_LA}}$	$\mathbf{\overline{C_LA} \cdot 1.2}$	$\mathbf{C_LA_{opt}}$
$\mathbf{C_LA}$ [m^2]	1.92	2.4	2.88	3.5
$\mathbf{C_DA}$ [m^2]	0.64	0.8	0.96	1.16
$\mathbf{C_LA/C_DA}$	3	3	3	3
Lap Time [s]	72.937	72.609	72.321	72.043
CPU Time [s]	1764	1565	1507	2396
Penalties [s]	0.132	0.135	0.136	0.158
Previous Solution Guess	yes	no	yes	yes

Table 4.10: Simulation parameters used for lift optimization.

[1]Multiple parameter optimization, however, is available in GPOPS, but it is not used to avoid an increase in the numerical difficulties of the problem.

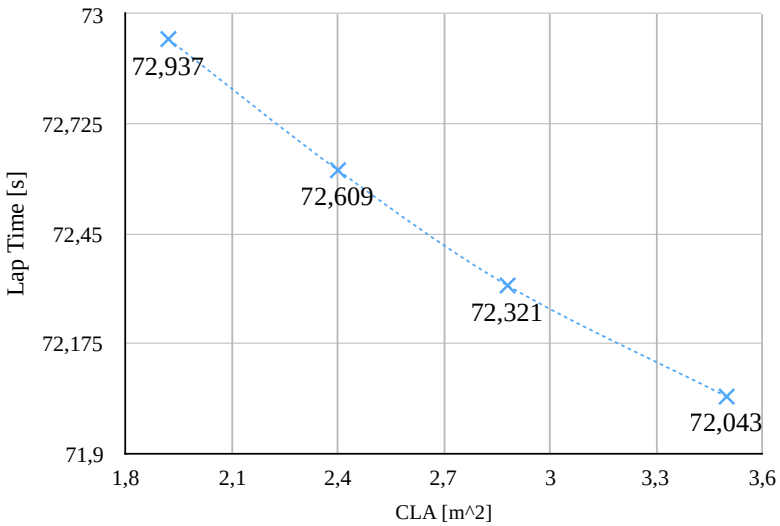

Figure 4.47: Variation of the lap time in terms of lift coefficient $C_L A$.

In fig. 4.48 is reported the difference between the normal coordinate n for optimal value of $C_L A$ and a lower value of 1.92 m^2; the difference Δn between the optimum parameter and the highest values of the range considered is zero, because $C_L A_{opt} = C_L A_{max} = 3.5$ m^2. The curve shows that the main differences in terms of trajectory can be found in the first curve (*Ramata*) and last curve (*Della Fonte*) of the track that are located respectively at $s \approx 500$ m and $s \approx 2400$ m (fig. 4.49); in particular Δn is maximum in correspondence to the entrance of the corners, or rather where the driver prepares the trajectory for an optimal traveling of the corner. Regarding the first corner, the simulation for $C_L A_{opt}$ determines a delay in the maneuver of reaching the external curb before the corner and a larger trajectory is chosen during the corner itself, anticipating the exit phase. In fact higher loads causes a reduction of the adherence limits and the ideal driver travels the curve without using too high lateral slip angles and preparing the exit to anticipate the full throttle phase. The approaching phase, moreover, stresses the opposite steering maneuver that reduces the lateral load transfer. On the contrary, for $C_L A_{low}$, the vehicle exploits the higher friction coefficients available and produces a trajectory with less distance travelled. Similar consideration can be made for the last corner of the track, although the cornering trajectory and the exit maneuver is substantially identical.

The longitudinal load transfer (fig. 4.50) is higher for $C_L A_{opt}$, because the most part of the downforce is applied at the rear axle; during braking a peak is registered because the braking action is delayed in the optimum model: in fact a lower load transfer from the rear to the front wheels limits the decrease of the friction coefficient of the front wheels and increases the effectiveness of the braking action for the rear wheels. The lateral load transfer is higher using the optimal parameter both in the first and in the last corner: although the vehicle adopts a more accentuated opposite steering action before the curve to reduce the lateral transfer, it enters the corner faster and the centrifugal action increases. Moreover in the first curve the enlarged trajectory permits to reduce ΔN_{lat} in the second

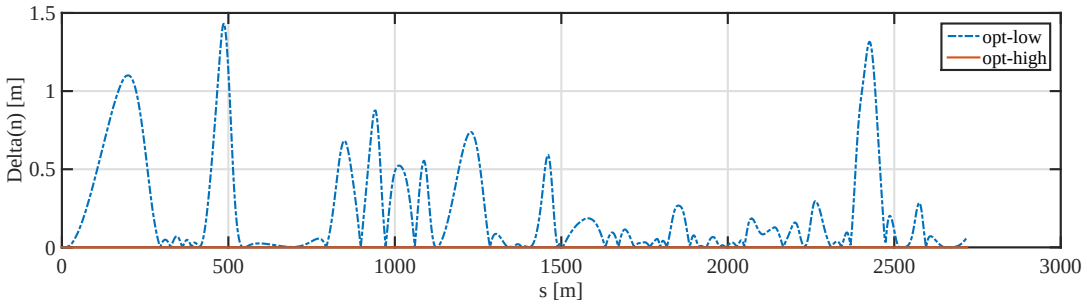

Figure 4.48: Absolute value of the difference between the curvilinear coordinate n for lower and higher (optimum) value of $C_L A$: $\Delta n = |n_{opt} - n_{low}|$.

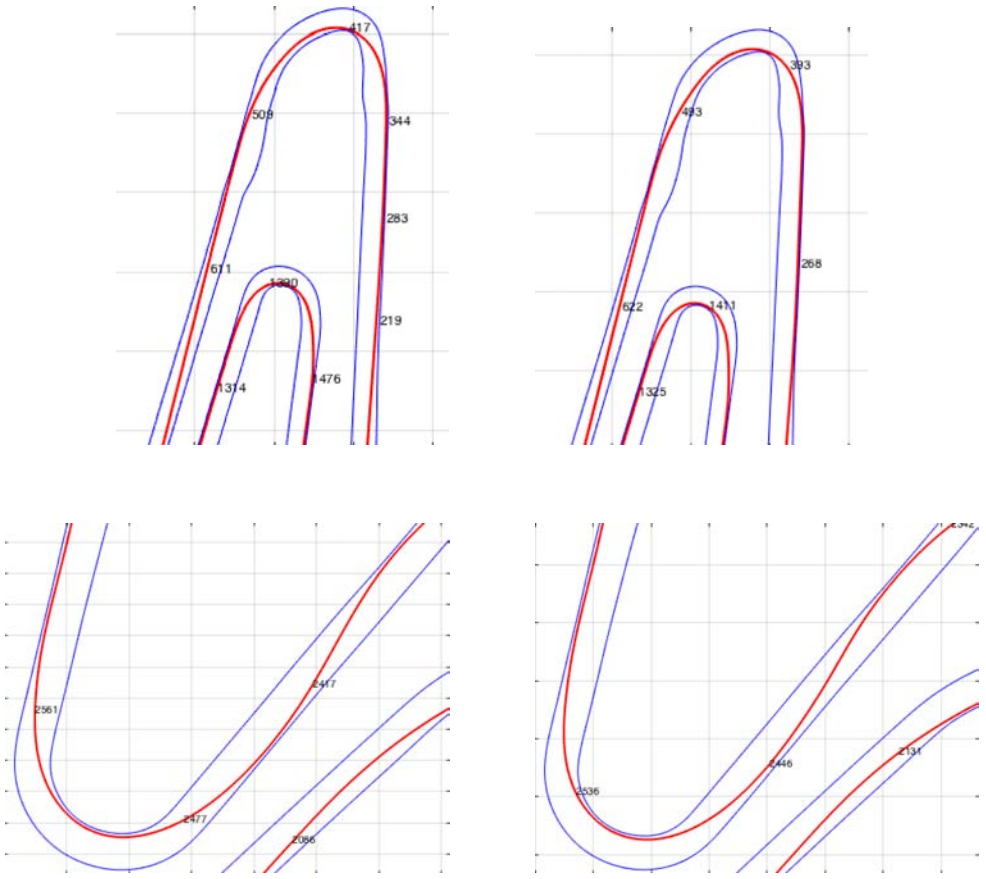

Figure 4.49: Magnified views of *Ramata* and *Della Fonte* curves for optimal (left) and lower value (right) of the parameter.

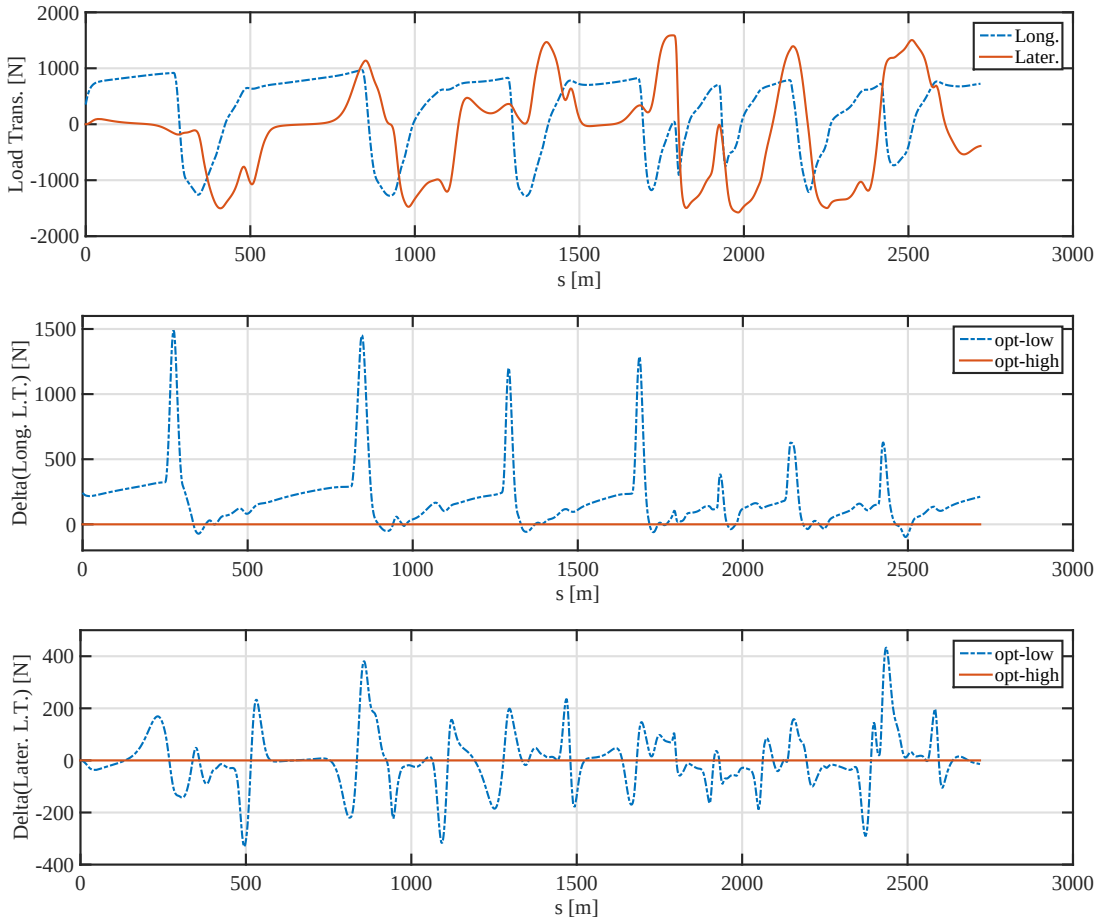

Figure 4.50: Load transfer for $C_L A_{opt}$ (top) and difference between the longitudinal (mid) and lateral (bottom) load transfer for lower and higher (optimum) value of $C_L A$: $\Delta(\Delta N) = \Delta N_{opt} - \Delta N_{low}$.

part of the corner.

In fig. 4.51 can be observed that the vehicle delays the braking action in all the curves and is capable of a higher braking force, thanks to the rear wing that reduces the longitudinal load transfer in braking conditions.
The velocity profile (fig. 4.52) confirms the previous conclusions: the vehicle with the optimum lift coefficient travels the corners faster and is able to use a better traction at the exit; in spite of that the greater value of the drag coefficient $C_D A$ determines a lower speed during the straights.

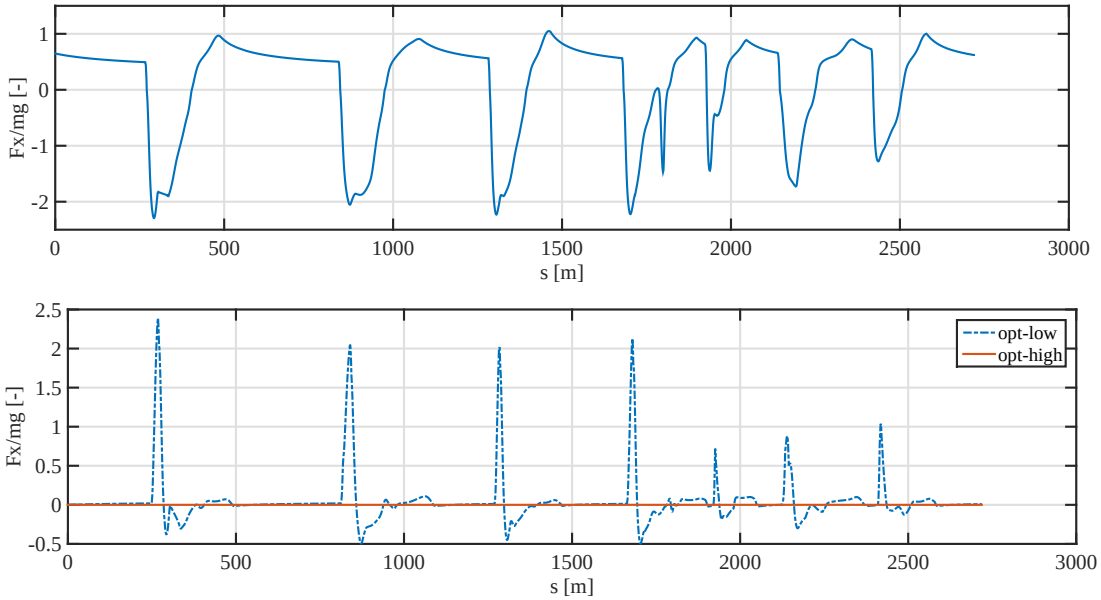

Figure 4.51: Longitudinal force for $C_L A_{opt}$ (top) and difference between the longitudinal force for lower and higher (optimum) value of $C_L A$: $\Delta(F_x/mg) = (F_x/mg)_{opt} - (F_x/mg)_{low}$.

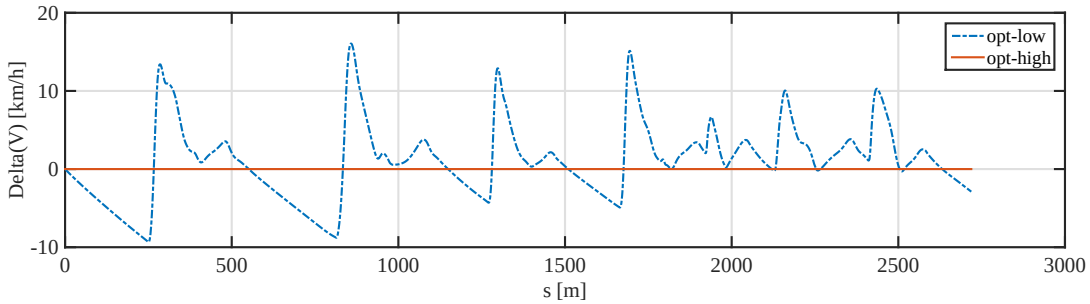

Figure 4.52: Difference between the speed profile for lower and higher (optimum) value of $C_L A$: $\Delta V = V_{opt} - V_{low}$.

Conclusions

This work represents, for the University of Padua, the first in-depth investigation on the direct optimal control methods applied to four-wheeled vehicles; in addition the research has been developed with the aim of investigating different modelling strategies and providing a complete optimization analysis of the most important parameters in the vehicle dynamics. The whole amount of simulations employed has permitted first of all to highlight the differences between the models considered in terms of the vehicle dynamic behavior; owing to the choice of control variables and the implementation of all the slip quantities and their coupling expressions, significant differences have been studied to convey the dynamic principles that stay behind these results. In general, if on the one hand the *basic* vehicle needs to travel straight and sharp trajectories to achieve the best performance, the *slip-slip* model, considering the same parameters, takes advantage of a more rounded trajectory that allows to exploit more effectively the tyre adherence and to reduce the load transfer. Secondly the usage of three different tracks, has granted an all-round analysis of the strategies, with which the ideal driver manages to face with the various characteristics that identify each single track, such as the slope, the curvature and the corners distribution along the circuit. The *basic* model presents some difficulties to reach the top performance in the parts of the track where long straights are separated by slow and medium speed corners; the sequence of curves, instead, represents a critical aspect for the *slip-slip* model, because in these conditions it is more difficult to reduce the effect of load transfer with gradual maneuvers.
In table 4.11 are reported the results obtained simulating the two models in the circuits considered. Thanks to the choice of the tyre data and the aerodynamics coefficients, the experimental lap time value results similar to the best lap time performance obtained with the optimal control simulations; in most of the tracks the *slip-slip* model reaches better results because the adherence ellipses are slightly larger than the constant ellipses implemented in the *basic* model: as underlined several times, this aspect is one of the core concepts for the achievement of the minimum lap time. In the circuit of Imola, instead, the *basic* model obtains a lower lap time than the *slip-slip* vehicle, due to the high technical difficulties of the track; this is a consequence of the fact that the adherence of the *basic* car is not affected by the load transfer, which produce relevant values in this circuit.
Both the penalties, or rather the time added to make unfavorable the use of the controls, and the CPU time, or rather the time needed for the simulations to converge with the imposed tolerance, are connected to the solving difficulties, that are dramatically increased with the use of the *slip-slip* model. The most

significant issues that affect the numerical efficiency of the problem are related to the combination of the lateral and longitudinal forces, to the slip limits (the higher the slip limits, the greater the time to convergence) and to the path constraints connected to the determination of the forces (i.e. braking ratio). A particular attention should be drawn to the effect of the slip limits: if the slip values overtake the value correspondent to the maximum of the tyre force, a lower force becomes available, even though the slip increases; this represents an outstanding drawback for the numerical solution of the problem because of the reach of the unstable domain for the tyre force. In spite of that, no univocal limits for the slip quantities can be individuated with the purpose of avoiding the overtaking of the stable domain, because the force maximum position depends on the loads applied in each wheel; therefore the slips boundary condition must be imposed with sufficiently high values, in order to make the controls able to exploit the whole dynamic possibilities.

Model	**Track**	**Lap** [s]	**CPU** [s]	**Penalty** [s]	**Real** [s]
Basic	**Adria**	76.398	191	0.075	76.630
	Monza	107.645	237	0.065	107.584
	Imola 2D	100.087	490	0.104	100.565
	Imola 3D	100.600	492	0.100	100.565
Slip-Slip	**Adria**	75.211	884	0.138	76.630
	Monza	106.298	2025	0.132	107.584
	Imola 2D	100.200	2837	0.191	100.565

Table 4.11: Simulations with different track and models.

A further analysis has been provided considering the *slip-slip* model in the Adria raceway and simulating the vehicle for different values of the main parameters that influence the dynamics. The study has been focused on the roll stiffness ratio ξ, the longitudinal (b) and vertical (h) position of the CoM, the wheelbase w, the width T, the yaw inertia I_z, the viscous constant of the differential k_d and the lift area $C_L A$: for each parameter a series of values was chosen, starting from a realistic value for the vehicle, and the profile of the lap time has been found for each parameter, in order to identify the effect on the performance. Consequently it has been possible to validate the result of the parametric optimization of GPOPS, that allows to find the optimal parameter to minimize the lap time.
A summing up of the optimal values found is reported in table 4.12, in which is also calculated the time improvement between the model characterized by the reference value of the parameter and the vehicle that implements an optimized parameter. The lowest lap time values are obtained adopting the lift downforces, that determine an increment of the tyre forces available. The absolute best lap time has been reached optimizing the parameter b with non-zero lift forces because are accentuated both the handling properties of the front of the car (and therefore the *oversteering* capabilities) and the tyre forces available.; moreover in this

case is achieved the lowest penalty value because the model results particularly controllable. In terms of CPU time, the longest simulations are related to the optimal (and maximum) lift coefficient, to the differential analysis and to the longitudinal position of the CoM; instead, the shortest simulations are obtained with the wheelbase and track optimization. As stated previously, k_d is implemented with a path constraint that is hard to satisfy and reaches the highest value for the penalty term, while b is related to the vehicle stability: increasing the *oversteering* behavior, in fact, reduces the *critical speed* of the car. Moreover $C_L A$ reduces the adherence limits and increases the difficulties of converging to the optimal values of the controls. Wheelbase and track, on the contrary, are related to the load transfer and, thanks to the normal load control strategy, do not represent a difficult constraint to satisfy. The most relevant time improvement is achieved with the optimal values of the CoM position parameters b and h, that are coincident to the minimum values available in the intervals considered; reducing b and h, in fact, corresponds to an improvement in terms of performance. This outstanding effect on the lap time is due to different causes: b is related to the static load distribution and to the *oversteering* capabilities, while low values of h reduce the lateral and longitudinal load transfer. Therefore these effects assume a fundamental importance for the improvement of the dynamic performance. By contrast, approximately zero time improvement is obtained changing the yaw inertia that, for a range of realistic values, does not affect the dynamic capabilities of the vehicle.

If on the one hand each parameter considered has a different effect on the dynamic quantities of the model, on the other hand it should be noticed that in each case can be highlighted a common dynamic behavior that leads to a performance improvement. In fact the lowest lap times are achieved with more sharp and straight trajectories, with delayed braking action and anticipated full throttle phase. This strategy determines a decrease in terms of distance traveled and is made possible only by the grip increment due to the better adherence conditions reached adopting the optimal parameters.

All the analyses developed in this research work have permitted to comprehend the importance of the modelling activity, that allows to capture peculiar aspects of the vehicle dynamics, related to the possibility of describing the most important behaviors that affect the performance; the choice of the model equations and of the optimal problem variables have also important consequences on the numerical capabilities of the solver to converge to a proper solution, in terms of time needed and error tolerance reached for the results. Complex models, that implement a complete description of all the dynamic aspects, may actually compromise the feasibility of the problem because it becomes hard for the solver to satisfy the constraints. Moreover the level of complexity of the model must be accurately chosen in order to find the optimum compromise between calculation efficiency and resulting accuracy: this depends on the case of study and on the grade of investigation needed, although typically the adoption of overall simple models, such as the *slip-slip* model, permits to capture a vaste amount of realistic behaviors and to develop an optimization of the real vehicle.

Future complications for this work can be related to the implementation of a *spin*

model of the vehicle, that allows to capture the spinning velocities of the wheels and to use directly the axle torque as a control variable; moreover a more complete description of the trim angles of the suspensions can be provided with a kinematic representation of the suspension movement. All these topics are surely connected to elevated numerical difficulties: probably the strategies used up to now might not have the capacity of facing with these problems and a more efficient approach could be needed.
These considerations lead the attention on the dramatic importance of the solution of optimal control problems in the vehicle dynamics research topics, thanks to the interesting possibilities that are made available and the flexibility allowed. This kind of problems, in fact, can be applied not only for the performance improvement, but also to the safety, the efficiency and the comfort of the vehicles, adjusting the focus of the optimal control analysis to the proper quantities of interest. In particular future developments can be implemented for the study of the driver's skills and characteristics, in order to optimize the best vehicle fitted to its driver, both for racing and for everyday-use application. To focus the attention on the driver, for instance, fixed-trajectory optimal control problems can be provided considering a minimization of the difference between the real controls (e.g. steering and longitudinal force) and the simulated ones as a target for the problem. Other implementations of these strategies can be used to optimize the automatic gear shifts or the vehicle trim (e.g. pneumatic suspensions or active aerodynamics) in order to reduce the consumption or to improve the performance or the comfort during a travel.

Parameter	**Value**	**Best Lap [s]**	**CPU [s]**	**Penalty [s]**	**Improvement [%]**
$\boldsymbol{\xi}$ **[-]**	0.869	73.852	1782	0.158	1.8
$\mathbf{b}$ **[m]**	1.112	72.774	1934	0.151	3.2
$\mathbf{b_{lift}}$ **[m]**	0.128	71.159	1135	0.125	2.0
$\mathbf{h}$ **[m]**	0.100	72.823	1459	0.158	3.2
$\mathbf{w}$ **[m]**	3.600	75.089	465	0.159	0.2
$\mathbf{T}$ **[m]**	2.800	74.384	624	0.146	1.1
$\mathbf{I_z}$ **[kgm^2]**	3000	75.098	1097	0.141	0.03
$\mathbf{k_d}$ **[Nms]**	100	74.173	1972	0.267	1.4
$\mathbf{C_LA}$ **[m^2]**	3.5	72.043	2396	0.159	0.8

Table 4.12: Optimal parameters used for performance optimization.

Bibliography

[1] J. T. Betts: *Practical Methods for Optimal Controls Using Nonlinear Programming, 2nd edition*, SIAM, 2010;

[2] A. Bryson: *Dynamic Optimization*, Addison Wesley Longman, 1999;

[3] M. Tanelli, M. Corno, S. M. Savaresi: *Modelling, Simulation and Control of Two-Wheeled Vehicles*, Wiley, 2014, ch. 5;

[4] E. Bertolazzi, F. Biral, M. Da Lio: *Symbolic-numeric efficient solution of optimal control problems for multibody systems*, Journal of Computational and Applied Mathematics, 2006;

[5] M.A. Patterson, A. V. Rao: *GPOPS-II: A MATLAB Software for Solving Multiple-Phase Optimal Control Problems Using hp-Adaptive Gaussian Quadrature Collocation Methods and Sparse Nonlinear Programming*, ACM Transactions on Mathematical Software, 2014;

[6] A. Waechter, L. T. Biegler: *On the implementation of an interior-point filter line-search algorithm for large-scale nonlinear programming*, 2005;

[7] Weinstein, M. J., Patterson, M. A., and Rao, A. V.: *Utilizing the Algorithmic Differentiation Package ADiGator for Solving Optimal Control Problems Using Direct Collocation*, 2015 AIAA Guidance, Navigation, and Control Conference, 2015;

[8] H. B. Pacejka: *Tire and Vehicle Dynamics*, Butterworth-Heinemann, Oxford, 2002;

[9] G. Perantoni, D.N. Limebeer: *Optimal Control of a Formula One Car on a Three-Dimensional TrackPart 1: Track Modeling and Identification*, ASME. J. Dyn. Sys., Meas., Control, 2015;

[10] D. Casanova , R.S. Sharp, P. Symonds: *Minimum Time Manoeuvring: The Significance of Yaw Inertia*,Vehicle System Dynamics: International Journal of Vehicle Mechanics and Mobility, 2010;

[11] V. Cossalter, M. Da Lio, R. Lot, L. Fabbri: *A general method for the evaluation of vehicle manoeuvrability with special emphasis on motorcycles*, Vehicle System Dynamics, 1999;

[12] D. J. N. Limebeer, A. V. Rao: *Faster, Higher, and Greener: Vehicular Optimal Control*, IEEE Control Systems Magazine, 2015;

[13] R. Lot; F. Biral: *A Curvilinear Abscissa Approach for the Lap Time Optimization of Racing Vehicles*, 19th IFAC World Congress, 2014;

[14] S. Bobbo, V. Cossalter, M. Massaro, M. Peretto: *Application of the Optimal Maneuver Method for Enhancing Racing Motorcycle Performance*, Motorsport Engineering Conference, 2009;

[15] A.J. Tremlett, M. Massaro, D.J. Purdy, E. Velenis Assadian, A.P. Moore and M. Halley: *Optimal control of motorsport differentials*, Vehicle System Dynamics, 2015;

[16] M. Guiggiani: *Dinamica del Veicolo*, Città Studi, 2012.